12-2021

Complete Modeling of the Chondrogenic Environment under Continuous Low-Intensity Ultrasound

Heather Newell
University of Nebraska-Lincoln, heather.newell@huskers.unl.edu

Newell, Heather, "Complete Modeling of the Chondrogenic Environment under Continuous Low-Intensity Ultrasound" (2021). *Chemical & Biomolecular Engineering Theses, Dissertations, & Student Research*. 39.
https://digitalcommons.unl.edu/chemengtheses/39

COMPLETE MODELING OF THE CHONDROGENIC ENVIRONMENT UNDER CONTINUOUS LOW-INTENSITY ULTRASOUND

by

Heather A. Newell

A DISSERTATION

Presented to the Faculty of

The Graduate College at the University of Nebraska

In Partial Fulfillment Requirements

For the Degree of Doctor of Philosophy

Major: Chemical and Biomolecular Engineering

Under the Supervision of Professor Hendrik J. Viljoen

Lincoln, Nebraska

December, 2021

COMPLETE MODELING OF THE CHONDROGENIC ENVIRONMENT UNDER CONTINUOUS LOW-INTENSITY ULTRASOUND

Heather A. Newell, Ph.D.

University of Nebraska, 2021

Adviser: Hendrik J. Viljoen

Articular cartilage is an avascular tissue that requires therapeutic intervention methods. This work answers the following: determine transducer operation to optimize the bioeffects; calculate the magnitude of pressure exerted on chondrocytes at an injury site; and confirm the theoretical findings by an animal model.

Earlier work has shown that cellular response to US is maximized at the resonance frequency of the cells. Resonance frequencies were calculated for chondrocytes in various layers. The latter configuration closest resembles in vivo conditions and the resonance occurred at 3.8±0.3 MHz. The 3D model of US propagation in a rabbit knee was constructed from MRIs to produce anatomically correct domains. US attenuates in cartilage and 3D results showed that pressure is maximized at an injury site when the transducer is placed in line with the site. Transducer positions that causes US waves to traverse cartilage before reaching the injury site must be avoided. The 3D model is time-consuming, and impractical for routine clinical usage. The average pressure delivered is lower in pulsed low-intensity US compared to cLIUS.

A 1D model, which captured all the key results of the 3D model, was used to calculate the temperature rise due to US dissipation – the cLIUS protocol produces

negligible increases in temperature. US attenuation can be overcome if the injury site lies in the near-field of the transducer, where constructive interference tends to not only cancel attenuation but delivers pressures higher than the transducer value – confirmed by both 3D and 1D models.

Rabbit studies confirmed that cLIUS treatment significantly improved healing of damaged cartilages, and defect sites filled, in contrast to fibrous filling in untreated defects. Finally, a model that involves three intracellular pathways was used to investigate mechanochemical response of a mesenchymal stem cell (MSC). Results showed that MSCs could be prompted towards the condensation step by mechanical stimulation at the resonance frequencies without any exogeneous chemical prompting, and the key proteins formed much earlier than in in vitro experiments.

ACKNOWLEDGEMENTS

I would firstly like to thank my advisor, Dr. Hendrik Viljoen for the many years of support and encouragement he has provided. Even during my undergraduate days he was always available for helpful discussions and insight. I would also like to thank Dr. Anu Subramanian for her guidance during this time. Special thanks also goes to Dr. Nejati and Dr. Avalos for being on my committee and taking time to read through the many iterations of this work.

I would also like to thank my family for their continued support during my education. Without my mother, I would not have had the courage to do any of this. The constant reminder that my future had no limitations and I could be whatever I wanted to be pushed me to pursue research in science. My brother Josh has always been there to ground me and give me a break for fun whenever I needed it. My sister Nicole shares in my excitement for mathematics and the resulting helpful discussions that came from our time together. Also, thanks go to my soulmate Jessika who has always been available to provide encouragement, support, and love my whole life.

TABLE OF CONTENTS

LIST OF FIGURES

LIST OF TABLES

CHAPTER 1 – INTRODUCTION

1.1 ARTICULAR CARTILAGE

Articular cartilage is an avascular tissue that lies between joints to protect bones from bone on bone contact. The lack of blood vessels in cartilage translates to lack of nutrient delivery and thus makes the healing of damaged areas very slow without outside intervention (Oldershaw, 2012). The primary reason is that the cartilage lacks any vascularization. Many intervention methods have been developed in recent years such as chondrocyte implantation, bone marrow stimulation, tissue grafting, and mosaicplasty, to name a few (Bhosale, Richardson, 2008). These methods are promising, though full restoration has been elusive (Oldershaw, 2012). The research presented here provides deeper insights in the use of ultrasound (US) as a method to treat cartilage injuries. Specifically, it shows the effects that continuous low-intensity ultrasound (cLIUS) have on cartilage tissue, beginning with a macroscopic model of a rabbit knee in 3D, and then progressing all the way to the effects of the US within the cell envelope. US is primarily a mechanical effect where at the interface between the cell and its environment, the mechanical signals are translated into chemical signals which initiate a series of reactions in certain cellular pathways.

1.1.1 OVERVIEW

Cartilage tissue is comprised of four different zones: the superficial zone, the middle zone, the deep zone, and the calcified zone (Fox *et al*., 2009). The superficial zone is the outermost layer and makes up 10-20% of total depth, while the middle zone makes up 40-60%, and the deep zone 30-40%. The calcified zone is made up of very few hypertrophic chondrocytes. Each zone has different mechanical properties and the chondrocytes within the zones vary in morphology, caused by the orientation of collagen fibers.

Chondrocytes are the building blocks for this tissue though they are the minority component in cartilage tissue making up approximately only 1.65% in each square millimeter of tissue (Hunziker *et al*., 2002). Their function is to maintain the matrix infrastructure by synthesizing collagens and proteoglycans. Extracellular and pericellular matrices (ECM and PCM) hold chondrocytes in place, and water fills in the gaps. The surrounding matrices consist of collagens and proteoglycans providing structure. The mechanical properties of the ECM and PCM tissue have been studied intensively as they receive signals from outside environments to translate to cells.

1.1.2 OSTEOARTHRITIS

Osteoarthritis (OA) is a degenerative disease impacting the joint structure (Setton *et al*., 1999). The progression of this disease drives hypertrophic chondrocytes to apoptosis. The increase in population translates to an increase in the effect joint damage has. Trauma and age cause defects and degradation of cartilage by increased production in enzymes. This disease disrupts the ECM and PCM surrounding chondrocytes and increases tissue permeability causing a decrease in elasticity and thus a subsequent decrease in its load bearing capacity (Han *et al*., 2019).

Decreases in muscle mass and increases in fat mass occur with age (Ohkawa *et al*., 2005). An important secretor of inflammatory markers lies in the fat pad that protects the joint (Ioan-Facsinay, Kloppenburg, 2013). This positively correlates with the impact obesity has on progressing OA. Weight loss studies have shown a decrease in compressive force seen at the knee as well as decreased cytokines (Vincent *et al*., 2012).

During the aging process our joints lose the lubrication of synovial fluid. This causes the joint environment to evolve to an inflamed state by increased production of inflammatory mediators (Jebens, Monk-Jones, 1959). Physical results from this disease result in decreased physical function and joint pain. Knockout of an important cytokine interleukin (IL)-6 has been studied, where OA worsened as a result (Greene, Loeser, 2015). Though this was not an expected result, it only highlights the necessity to continue the study of the intricacies of this disease, as there are many inflammatory markers that work cooperatively (Morrisette-Thomas *et al*., 2014).

Normal everyday movement is imperative for cartilage health as it assists in cartilage homeostasis (Houard *et al*., 2013). Mechanical loads induce synovial fluid movement into cartilage providing nutrients to chondrocytes. In the occurrence of injury elevated levels of inflammatory markers are present causing swelling of the joint (Lieberthal *et al*., 2015). The response to damage releases pro- and anti-inflammatory mediators where it is thought that there exists a lack of control in the pro-inflammation marker response that causes further damage leading to OA (Goldring 2000). Resolution of inflammation is seen through anti-inflammatory markers produced early in post-injury.

1.1.3 IMPACT OF CARTILAGE INJURY AND LOSS

OA is not limited to the elderly and obese; healthy people that experience joint injuries can also develop the disease. Cartilage is eroded through trauma and age, degrading the tissue and damaging the bone surface as a result. Since chondrocytes are the minority constituent in cartilage tissue, their motility is limited. When joint tissues are injured in a healthy person, a subsequent loss of cartilage is observed (Elsaid *et al*., 2005). A study on anterior cruciate ligament (ACL) injuries (common in athletes) shows a six-fold loss of cartilage and damage years after the injury occurred (Murrell *et al*., 2001). In mechanical injury proteins are released that signal cell disruption and apoptosis (Stevens *et al*., 2009).

1.1.4 CARTILAGE REPAIR AND REGENERATION

The oldest method of cartilage repair utilizes bone marrow stimulation (Steinwachs *et al*., 2008). Methods were devised for marrow stimulation, which are located underneath the cartilage, and which can be accessed via penetrating the subchondral bone. One method that has been replacing older techniques like Pridie drilling or abrasion is microfracture. In this technique the damaged layer of cartilage is debrided, and small channels are drilled through the bone to reach marrow, providing a source of potent MSCs and nutrients in an otherwise avascular area (Kuo *et al*., 2006). Though this method has been continually improved, the technique often fails to repair the defect site (Solheim *et al*., 2020).

Autologous chondrocyte implantation (ACI) was introduced in 1987 as a biological cell-based approach to treat full-thickness cartilage defects (Grande *et al*., 1989). This method uses chondrocytes isolated from biopsy samples and implanted in the defect site under a periosteal cover. This environment provides protection and even nutrients to the implanted chondrocytes. A study comparing various orientations of ACI showed the efficacy of this method for cartilage repair (Horas *et al*., 2003). Furthermore, this method of cartilage repair has shown effective for long-term results even 10 to 20 years after treatment (Peterson *et al*., 2010).

Tissue grafting is another area of cartilage repair. One such extensively studied technique is osteochondral transplantation – or mosaicplasty (Robert, 2011). This method uses osteochondral autographs harvested from areas of the knee where there is low weight bearing. While utilizing donor tissues is promising, there exists differing thicknesses in cartilage tissue. This method is also a difficult method of repair and restricted for younger patients with small (less than 3cm in diameter) cartilage defects.

While these methods show success in cartilage tissue repair, they are also highly invasive causing more inflammation. A small portion of these methods also show little-to-no difference in cartilage tissue repair. Some methods alone are not effective enough and require combining techniques. These methods are also used when intervention becomes a requirement for the health and well-being of a patient. While preventative methods such as diet and exercise are important, US could be introduced at an earlier stage to assist in the prevention of OA development.

1.2 ULTRASOUND IN THERAPEUTICS

The use of US in therapeutics has been utilized for bone healing for decades (Hadjiargyrou *et al*., 1998). Ultrasound therapy has also proven useful for soft tissue healing, pain relief, and a facilitator of healing (Best *et al*., 2016). Promising results utilizing US as a therapeutic technique has probed the question of what else it could be used for. Recent methods employing US as therapy include wound healing (Dyson *et al*., 2003), burn care (Waldrop, Serfass, 2008), and surgical techniques for tumor treatments (ter Haar *et al*., 1989).

Treatment of cartilage with US was a natural shift as osteocytes (bone cells) and chondrocytes are so closely related. Following this progression, the therapies detailing a 1.5MHz frequency have been thoroughly studied, and in some cases applied in orthopedic clinical trials (Zhang *et al*., 2017). The efficacy of that regimen has been debated, and in a limited clinical study was found to be ineffective at cartilage regeneration as the sole therapeutic intervention (Loyola-Sanchez *et al*., 2012). This could be due to the transducer positioning, voltage used, frequency of the transducer, pulse duration, and many more variables.

1.2.1 *IN VITRO* ULTRASOUND APPLICATION

Ultrasound has been shown to assist in regenerating cartilage tissues with mechanical stimulation (Cook *et al*., 2001). The economical option of utilizing this therapeutic and noninvasive technique is attractive when compared to alternative methods. To begin to study US effects on cells, *in vitro* models are used. Mechanical stimuli enhance chondrocyte metabolic activity in alginate cultures (Min *et al*., 2007). In vitro ultrasound application to chondrocytes has been done with various frequencies ranging from 0.8MHz to 5MHz, but primarily at 1.5MHz (Cui *et al*., 2006; Aliabouzar *et al*., 2016; Budhiraja *et al*., 2017; Korstjens et al., 2008). All these in vitro studies show enhanced ECM synthesis and chondrocyte proliferation, though a review determined that there exists a lack of evidence for recommending this practice in clinical environments (Rothenberg et al., 2017).

1.2.2 EFFECT OF ULTRASOUND ON MSCS

The objective of applying ultrasound to marrow derived mesenchymal stem cells is to induce chondrogenesis. The mechanism of this is not well understood but the goal here is to help describe the phenomenon through mathematical modeling. The most crucial factor in healthy cartilage tissue is TGF-β. Though the requirement of TGF-β has wide agreement in literature there is also confirmation that it can induce degrading enzymes when in high quantities by activating the ALK1 receptor (Van den Berg, 2011), activating Smads1 and 5, which induces MMP13 synthesis.

Monitoring the effects of potential therapies through mathematical modeling has the advantage of predicting whether the proposed method will work. Many pathways are proposed to affect the health of a chondrocyte and therefore the surrounding environment. Utilizing US as a stimulant for chondrogenesis has been widely reported to positively impact chondrogenesis through activating mitogen activated kinase proteins (MAPKs) (Takeuchi *et al*., 2008; Whitney *et al*., 2012).

This research is a continuation to model the behavior of cells under cLIUS. A previous study on MSCs showed upregulation of cell proliferation regulators in vitro without impacting multipotency (Budhiraja *et al*., 2017). Further experimentation with cytokines showed suppression of inflammation, resulting in a chondroprotective role of cLIUS (Sahu *et al*., 2019). Additionally, the gene expression of master chondrogenic marker SOX9 was upregulated using cLIUS (Sahu et al., 2020). The phosphorylation of ERK was determined to be key in these results, which is a key intracellular signaling molecule in cell-surface receptor pathways.

1.2.3 *IN VIVO* ULTRASOUND APPLICATION

Preliminary studies focus on *in vitro* US applications and modeling and laboratory experiments are done in highly controlled environments. Simply transferring the therapeutic regimen to the *in vivo* environment will not produce the expected results as the complexity of the system has increased. This leads to the use of animal models for US therapy to further study its effects *in vivo*. Rabbit studies done by Yang *et al*., using 1.5MHz pLIUS showed no significant potential using the standard regimen for bone healing (Yang *et al*., 2014).

While these results showed no advantage for utilizing pLIUS for cartilage regeneration, there exists other in vivo experiments that show positive histological staining indicating upregulation in ECM component expression. Sheep studies done with bilateral cartilage defects show the formation of cartilage tissue treated with pLIUS at 200mW/cm^2 (Vahedi *et al*., 2021). Additionally, a pig study using 1.5MHz pLIUS showed an attenuation of the progression of cartilage degeneration in the joint (Naito *et al*., 2010). These animal studies conclude that US has potential for therapeutic intervention methods to treat OA.

1.3 OBJECTIVES

Previous theoretical and experimental outcomes have shown the benefits of cLIUS. Continuation of this research is necessary to examine the promotion of bioeffects.

The objectives of this dissertation are as follows:

- To evaluate US propagation in the joint on a macroscopic scale to examine the system pressure and ensure optimal transducer placement for maximal effects.

- Develop a mathematical model to describe the damping of US signal of the PCM surrounding the chondrocyte.
- Mathematically evaluate enhanced bioeffects US modulates during the first stage of chondrogenesis through integrated pathway kinetics.

The overall goal here is to examine pressure responses from large to micro scale to better understand the systemic response after microfracture procedures and cLIUS treatment. Analyzing this will allow for better understanding the role of cLIUS for *in vivo* therapeutics for cartilage repair in order for clinical application. A major contribution from this thesis is to offer a more complete picture of the connectivity between the mechanical stimulation and the secretion of new cartilage from stimulated cells, and providing a more quantitative picture of how the mechanical/chemical mechanisms function. Another contribution of this thesis is that it places the ultra-sound treatment of cLIUS on a firmer footing and advances its utility as a therapeutic method for cartilage regeneration.

CHAPTER 2 – COMPLETE SYSTEM MODEL

2.1 INTRODUCTION

This chapter will focus on the modeling of ultra-sound propagation in the rabbit knees with the commercial software package COMSOL Multiphysics (COMSOL Inc., Burlington, MA, USA). Although there have been significant advancements in software to solve complex physical problems, the actual modeling of US propagation in a knee remains a challenging task. Two problems stand out as particularly challenging in nature. First, the domain, which is the space in which the US model is solved, is very complex and it varies from animal to animal, person to person. Second, the materials that constitute the domain are not isotropic, homogeneous (as in the case of *in vitro* studies), but are best described as multi-phase materials with anisotropic properties, which require more sophisticated models such as Biot theory to describe the US propagation.

Previous modeling on the chondrogenic environment has been utilized to show the potential of US in the joint environment in 2D (Miller 2017). These 2D models were generated from sagittal views of rabbit and sheep MRIs. Theoretical results show that the placement of the transducer is key in optimal intensity reached at the defect site, as seen by the shift up/down on the sagittal view. Though these results give an insight to the environmental response, the bone geometry changes considerably when moving the transducer in the axial view.

2.2 MATHEMATICAL MODELING

While many studies and models have been developed for ultrasound applications *in vitro* (Rothenberg *et al*., 2017), there is a lack of *in vivo* studies. The translation of results from *in vitro* studies to *in vivo* applications is complicated because the *in vitro* studies lack the necessary complexity. In the past, some naïve conclusions about *in vivo* usage have been made, on the basis of *in vitro* findings. But extrapolating findings to another milieu that differs so much from the *in vitro* environment has oftentimes led to disappointing outcomes. Unfortunately, the stark reduction in complexity, found in *in vitro* experiments, specifically the lack of recreating the chondrogenic environment, has placed a questionable value on its use in clinical applications (Duda *et al*., 2004). Another aspect that frustrates researchers, is the inability to perform non-obtrusive monitoring of the chondrogenic environment on a continuous basis. Thence, we need to resort to mathematical modeling to provide these insights. Here, a complete model of the overall system is presented, starting with the piezo-electric transducer that delivers the pressure and progressing to the propagation of the pressure in an anatomically correct three-dimensional model. However, one should ask what is really gained from modeling the propagation in a knee?

The COMSOL modeling has been used to answer two key questions. First, we want to identify the optimal frequency bandwidth where US-induced bioeffects are maximized **within the *in vivo* environment** (Louw *et al*., 2013). Secondly, we want to determine what is the pressure at an injury site – the magnitude of the pressure on chondrocytes at the injured site will determine the amount of mechanical/chemical interaction that occurs on the cellular level and ultimately determine the extent to which the cells will respond to the mechanical stimulation. Clearly, to answer the second question we must solve the macroscopic model of US propagation through the knee. The 3D modeling of US propagation in a knee is an involved process. A methodical description of the macroscopic model should start with the piezoelectric transducer that provides the input for the pressure field.

2.3 KLM EQUIVALENT CIRCUIT FOR THE PIEZOELECTRIC TRANSDUCER

The Krimholtz, Leedom, & Matthaei (KLM) equivalent circuit has been used to describe the transition from electric input impedance to an acoustic impedance in ultrasonic transducers (Krimholtz *et al*., 1970; Castillo *et al*., 2003; Kim *et al*., 2019; Kar, Wallrabe, 2020). Other one-dimensional methods are available to describe equivalent circuits such as the Mason model (Kar, Wallrabe, 2020) though negative capacitance values prove problematic (Sherrit *et al*., 1999). Utilizing the KLM mathematic model allows for a pressure prediction at the surface of the transducer when coupled with transmission line theory and transfer functions (Castillo *et al*., 2003; Kulkarni, 2011).

This method of calculating pressures at the transducer surface has been well established in literature (Rathod 2019). Previous modeling utilized the KLM model of an immersion transducer coupled to the ultrasonic field using the transfer matrix/angular spectrum approach (Louw *et al*., 2015). The model here describes the maximum pressure propagated at the center of the transducer in a more simplistic fashion. Figure 1 shows the circuitry design with the piezoelectric element and matching layers (Krimholtz *et al*., 1970).

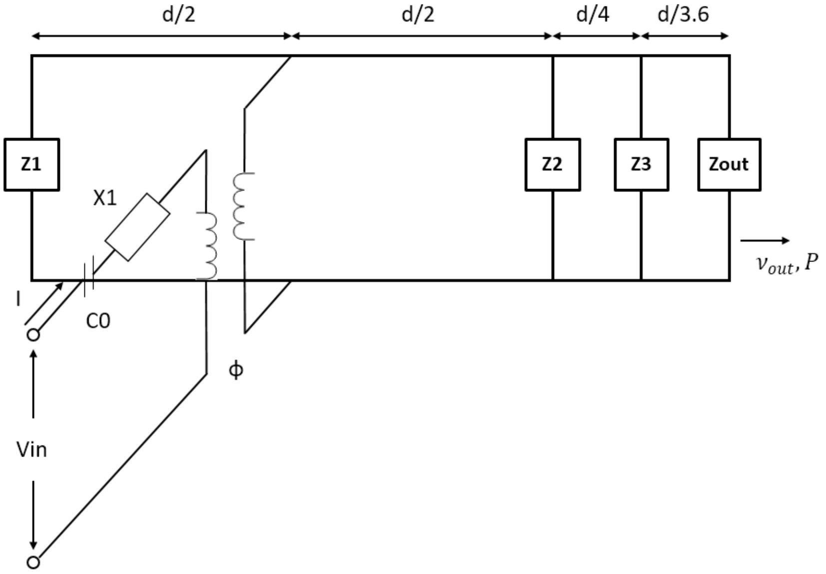

Figure 1: KLM Equivalent Circuit. Thickness of each layer is d, and impedances Z with subscripts are impedances radiating into the surrounding. Capacitor C0, impedance X1, and transformer turn ratio ϕ are calculated in Appendix B.

Most ultrasound transducer manufacturers keep the internal components as proprietary information; therefore, third party users need to resort to a model to predict the output pressure given an input frequency and voltage. The transducer modeled here is an unfocused 3.5MHz Olympus immersion transducer with a 6mm diameter (V384-SU) at a manufacture calibrated frequency of 3.8MHz. Previous experiments have been done using a transducer of different frequency and size from the same manufacturer (Olympus NDT, MA), allowing for output pressure calibration to be done (Louw *et al*., 2015). This was done by adding a small matching layer with properties similar to air in front of the wear plate matching layer. The thickness of the layer, along with its impedance was varied to sufficiently calibrate the model.

The goal of using this model is to develop a relationship between the input voltage V_{in}, and the output impedance Z_{out}, which can be used to calculate initial pressure values at the front of the transducer face (Bigelow, 2001). The initial pressure values can then be coupled with a sinusoidal signal generator to produce a frequency and time dependent pressure. Modeling the transducer begins with electric impedance shown by equation 2.3.1:

$$Z_e = \frac{1}{i\omega C_0} + iX1 + \frac{Z_a}{\phi^2} \qquad 2.3.1$$

where ω is the angular frequency, C_0 is the capacitor, $X1$ the impedance, ϕ the transformer turns ratio, and the input impedance of the transmission line is

$$Z_a = \frac{Z_{1in}Z_{2in}}{Z_{1in} + Z_{2in}} \qquad 2.3.2$$

Circuit parameters are well described in literature, and full calculations for each can be seen in Appendix B. The impedances Z_{1in} and Z_{2in} are calculated based on the backing material and matching layer material $Z_{1,2}$ as well as the piezoelectric element impedance Z_0,

$$Z_{1,2in} = Z_0 \frac{Z_{1,2} + iZ_0 \tan\left(\frac{\omega d}{2c}\right)}{Z_0 + iZ_{1,2} \tan\left(\frac{\omega d}{2c}\right)} \qquad 2.3.3$$

The impedances of the matching layers are similarly calculated, using the characteristic impedance of the layer itself. Together with transmission line theory this allows for the solution of the voltage-driven displacement response equations 2.3.4 and 2.3.5:

$$\nu_1 = \frac{exp(ikd/2) - \mathit{\Gamma}_2 \exp\,(-ikd/2)}{\phi Z_e(\exp(ikd) - \mathit{\Gamma}_1\mathit{\Gamma}_2 \exp\,(-ikd))}(1+\mathit{\Gamma}_1) \qquad 2.3.4$$

$$\nu_2 = \frac{\mathit{\Gamma}_1 exp(-ikd/2) - \exp\,(ikd/2)}{\phi Z_e(\exp(ikd) - \mathit{\Gamma}_1\mathit{\Gamma}_2 \exp\,(-ikd))}(1+\mathit{\Gamma}_2) \qquad 2.3.5$$

where k is the wavenumber, and current transmission coefficients are:

$$\mathit{\Gamma}_{1,2} = \frac{Z_0 - Z_{1,2}}{Z_0 + Z_{1,2}} \qquad 2.3.6$$

Each matching layer velocity can be determined using the forward velocity from the previous layer shown by equation 2.3.7:

$$\nu_x = \frac{Z_x(\nu_{x-1})}{Z_x \cos(k_x d_x) + iZ_{out}\sin(k_x d_x)} \qquad 2.3.7$$

where x denotes the layer number. Finally, pressure radiated from the face of the transducer can be solved for as a function of the last layer velocity and transducer face area.

$$P = Z_{out}\nu_{out}/Area \qquad 2.3.8$$

where ν_{out} is the last layer velocity. These equations provide an output pressure which shows a linear relationship to input voltage, as shown in Figure 2 with an input voltage of 3.5Vpp and 3.8MHz frequency. Material properties used are listed in Table 1.

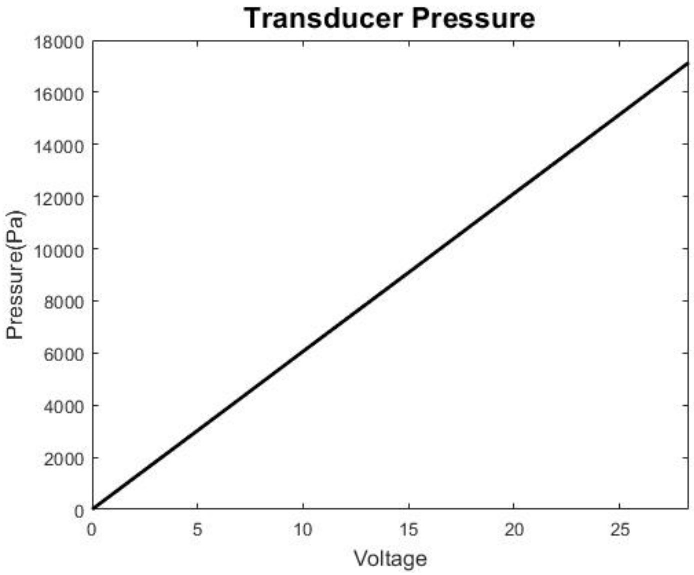

Figure 2: Output transducer pressure dependent upon input rms voltage for 3.5MHz transducer.

Piezoelectric Element	
c_{PZT}	$4897\ m/s$
ρ_{PZT}	$5840\ kg/m^3$
d	$\lambda/2\,mm$
Z_{PZT}	$20.17\ MRayl$
h_{33}	$2.19e9(1+0.029i)V/m$ (Sherrit *et al.*, 2007)
ε	$1.36e-8\ F/m$
Wear Plate	
c_w	$1480\ m/s$
d_w	$\lambda/4\ m$
Z_w	$\sqrt{Z_{water} * Z_{PZT}}$ (Kulkarni, 2011)

Table 1: Material property values for the KLM model.

The voltage applied to the transducer is output from a function generator that requires peak-to-peak voltage input. By varying the input voltage, the linear relationship between voltage and pressure is used to predict the pressure output at the face of the transducer. For the purposes of the 1.5MHz transducer study, the same KLM model was applied with the same constraints as the 3.5MHz transducer. A similar linear relationship was obtained, as shown in Figure 3.

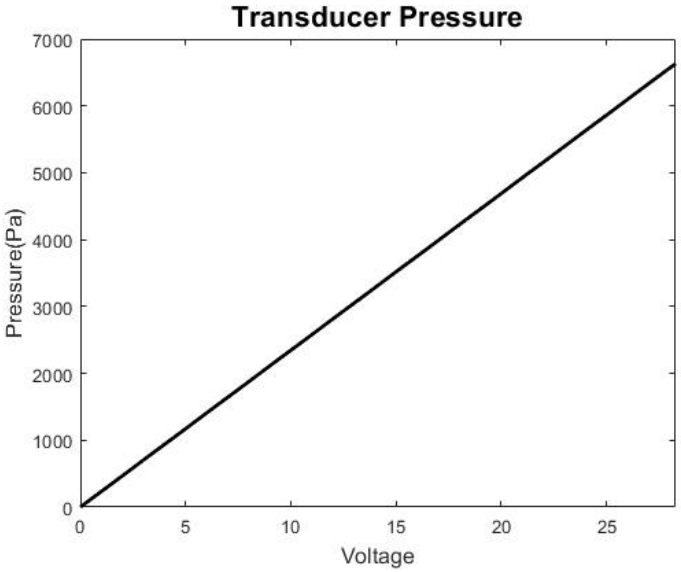

Figure 3: Output transducer pressure dependent upon input rms voltage for 1.5MHz transducer.

As we can see from comparing Figure 3 with Figure 2, the voltage input required is much higher to produce the same pressure output as the 3.8MHz transducer. In our experimental ultrasound procedure, the applied voltage was 3.5Vpp (peak-to-peak). The pressure output, based on the KLM model with this input, is shown to be 3kPa. To keep consistency, we used 3kPa for all the modeling, regardless of the transducer choice. To obtain this pressure for the 1.5MHz transducer an approximate voltage input of 9Vpp is required. The pressure output (at the transducer surface) of 3kPa is used for all further modeling in a 3D environment. The KLM model is used to calculate the pressure at the transducer surface and this value is an input for the COMSOL model.

As will be discussed later, the 3D simulations are computationally very expensive, and are not currently an option for routine clinical applications. In an effort to bring some computational guidance to the clinical setting, we also propose the use of a simple one-dimensional model to predict defect site pressure and temperature changes. A drastic increase in temperature can result in cell death, therefore analyzing this with cLIUS application is vital.

2.4 COMSOL MODELING

2.4.1 PRESSURE ACOUSTICS MATHEMATICS

The pressure acoustics module in COMSOL is governed by the wave equation with assumptions of adiabatic flow and lossless, i.e. no viscous effects, together with a linear equation of state. Applying a harmonic solution in the general form of $p(x,t) = p(x) * e^{i\omega t}$ where $p(x)$ is the instantaneous pressure and ω is the angular frequency results in the inhomogeneous Helmholtz equation in the frequency space (Morse, Ingard, 1986):

$$\nabla \cdot \left[-\frac{1}{\rho_c} (\nabla p_t - \boldsymbol{q}_d) \right] - \frac{k_{eq}^2 p_t}{\rho_c} = Q_m \qquad 2.4.1$$

Pressure here is p_t the total pressure, $\boldsymbol{q}_d$ and Q_m are sources, and k_{eq} is a function of the angular frequency ω and speed of sound c_c so that $k_{eq} = (\omega/c_c)^2$ (Zwikker, Kosten, 1949). The total acoustic pressure p_t is the sum of the pressure solved for, including the scattered pressure and the background pressure. When damping occurs in the system, both density ρ_c and c_c are complex values which is represented by the subscript notation. In the case of user defined attenuation, we set $\rho_c = \rho c^2/c_c^2$ and $c_c = \omega/k$. Material properties of the model prescribe the density ρ and speed of sound c in each domain. The wave number in this case is defined as (COMSOL, 2018):

$$k = \frac{\omega}{c} - \left(ln(10)\frac{\alpha}{20}\right)i \qquad 2.4.2$$

where α is the attenuation coefficient. Source terms do not apply here and are set to zero $\boldsymbol{q}_d = Q_m = 0$. When modeling in the frequency domain, the specification of a pressure source at the position of the transducer serves to mimic the action of the transducer surface, thus a cylindrical radiation boundary condition is specified where p_0 is the amplitude of the harmonic pressure source. The radiation boundary condition is applied to the outermost boundaries of the model to depict minimal reflection of the wave to domains which lie adjacent to the modeling domain. This boundary condition, using a plane wave for the transducer, is set to (COMSOL, 2018):

$$-\mathbf{n}\cdot\left(-\frac{1}{\rho_c}\nabla p_t\right) + \frac{ikp_t}{\rho_c} = (ik - i(\mathbf{k}\cdot\mathbf{n}))\frac{p_0}{\rho_c}e^{-i(\mathbf{k}\cdot\mathbf{r})} \qquad 2.4.3$$

where k is the wavenumber, $\mathbf{k}$ is the wave vector set to $\mathbf{k} = k\mathbf{n_k}$ with $\mathbf{n_k}$ being the unit vector in the direction of propagation.

2.4.2 POROELASTIC WAVES MATHEMATICS

Mathematical modeling was done using COMSOL Multiphysics in an effort to optimize the cLIUS application (cLIUS or continuous low-intensity ultra-sound). When cells are subjected to US, the cells act like oscillators, in a mechanical sense, and therefore resonance frequencies exist where the cells couple most effectively with the impending US field (Kim *et al*., 2008; Miller *et al*., 2017). This results in complex biomechanical behaviors effecting metabolic activity of a cell. This coupling can be understood as the transfer of mechanical energy to the cells. In a linear model, the amount of mechanical energy (kinetic + potential) approaches infinity, but nonlinear effects will limit the total mechanical energy (Miller *et al.,* 2017). Louw *et al.* reported the first linear resonance modeling of cells suspended in solution and found that chondrocytes have a primary resonance frequency of 5 MHz (Louw *et al*., 2013). That model was expanded by Miller *et al*., to include nonlinear effects. The nonlinearities stemmed from the use of an equation of state as proposed by Shchetinin (Shchetinin, 1991). The nonlinear analysis showed that the resonant frequencies lie in a range of 3.5-4.1MHz (Miller *et al*., 2017). Translation to the in vivo model can be assumed a similar range as the model of a chondron in an ECM plug in suspension are closest to the in vivo environment. The mathematical model that was used for the linear resonance studies were Biot's poroelastic acoustics solving the wave equation for pressure, sound pressure level, and stored energy density in the frequency space. Expansion of work done on Miller *et al*., 2017 has been done here by confirming the chondrocyte environment and expansion to the MSC. Biot theory is commonly used in calculating pressure in biological materials and more specifically in cartilage tissue (Suh, DiSilvestro, 1999). A brief review of Biot's theory is presented. The governing equation for a poroelastic model is given by (COMSOL, 2018):

$$-\nabla \cdot \boldsymbol{\sigma} = \boldsymbol{F} \qquad 2.4.4$$

where the divergence of the Cauchy stress tensor $\boldsymbol{\sigma}$ is set equal to the source term $\boldsymbol{F}$, and this source term is defined as a body load. The strain tensor is defined as (Atalla *et al*., 1998)

$$\boldsymbol{\epsilon} = \frac{1}{2}[(\nabla\boldsymbol{u})^T + \nabla\boldsymbol{u}] \qquad 2.4.5$$

and is dependent on displacement of the porous material $\boldsymbol{u}$. The expressions for poroelastic waves derived by Biot with the assumption of time-harmonic dependence for both displacements $\boldsymbol{u}$ and $\boldsymbol{w}$ are (Biot, 1956; Allard, 1993)

$$-\rho_{av}\omega^2\boldsymbol{u} + \rho_f\omega^2\boldsymbol{w} - \nabla\cdot\sigma = 0 \qquad 2.4.6$$

$$-\rho_f\omega^2\boldsymbol{u} - \rho_c\omega^2\boldsymbol{w} + \nabla p_f = 0 \qquad 2.4.7$$

where p_f is the pore pressure. This is the pressure which the COMSOL solves for instead of the fluid displacement $\boldsymbol{w}$. This simplifies equation 2.4.7 to

$$w = \frac{1}{\rho_c\omega^2}\left(\nabla p_f - \rho_f\omega^2\boldsymbol{u}\right) \qquad 2.4.8$$

This can be then applied to equation 2.4.6 so that it becomes

$$-\rho_{av}\omega^2\boldsymbol{u} - \frac{\rho_f}{\rho_c}\left(\nabla p_f - \rho_f\omega^2\boldsymbol{u}\right) - \nabla\cdot\sigma = 0 \qquad 2.4.9$$

The same assumption of time-harmonic can be applied to the elastic wave equation and can be written as (Biot, 1956)

$$-\left(\rho_{av} - \frac{\rho_f^2}{\rho_c}\right)\omega^2\boldsymbol{u} - \nabla\cdot(\boldsymbol{\sigma} - \boldsymbol{s}_0) = \boldsymbol{F} \qquad 2.4.10$$

where $\boldsymbol{\sigma}$ is the total stress tensor of the fluid and porous material, ρ_f is the density of the fluid, ω the angular frequency defined as a function of the frequency $\omega = 2\pi f$, and ρ_{av}

is the average density defined by the summation of the porous matrix density ρ_d and the fluid density (COMSOL, 2018):

$$\rho_{av} = \rho_d + \epsilon_p \rho_f \tag{2.4.11}$$

The complex density ρ_c is described by (COMSOL, 2018)

$$\rho_c = \frac{\tau_{¥}}{\epsilon_p}\rho_f + \frac{\widetilde{\mu_f}}{i\omega\kappa} \tag{2.4.12}$$

where $\widetilde{\mu_f}$ is the frequency dependent viscosity, κ is permeability, $\tau_{¥}$ the tortuosity factor, and ϵ_p is the porosity. Working in the high frequency application of ultrasound requires a correction as the flow profile can no longer be considered Poiseuille like. This impacts the reference frequency as well as the viscosity. The frequency dependent viscosity is defined as (COMSOL, 2018)

$$\widetilde{\mu_f} = \mu_f F\left(\sqrt{f/f_r}\right) \tag{2.4.13}$$

where μ_f is the fluid dynamic viscosity, f the working frequency, and f_r the reference frequency. The viscosity model used in these cases is Biot's high frequency range, where the reference frequency is characterized by the pore size which is calculated as follows (Biot, 1956):

$$f_r = \frac{\mu_f}{2\pi a^2 \rho_f} \tag{2.4.14}$$

Here a is the pore size. The total stress tensor is a combination of contributions from the drained porous matrix and the fluid so that (COMSOL, 2018)

$$\boldsymbol{\sigma} = \boldsymbol{\sigma}_d - \alpha_B p_f \boldsymbol{I} \tag{2.4.15}$$

Applying the identity tensor ***I*** results in the pore pressure only contributing to the diagonal of the total stress tensor. The fluid parameters used in modeling are those of water since it has similar properties as the synovial fluid (Fox *et al.*, 2009). The parameter F is a frequency dependent on the viscous drag and defined by Bessel functions of the first kind (Biot, 1956).

$$F = \frac{1}{4}\left[Q\left(\frac{-\sqrt{-i}J_1\left(\sqrt{-i}Q\right)}{J_0\left(\sqrt{-i}Q\right)}\right)\Big/\left(1 + 2i\left(\frac{-\sqrt{-i}J_1\left(\sqrt{-i}Q\right)}{J_0\left(\sqrt{-i}Q\right)}\right)\right)\right] \qquad 2.4.16$$

Biot's module M is described by (Biot, 1962)

$$\frac{1}{M} = \epsilon_p \chi_f + \frac{\alpha_B - \epsilon_p}{K_d}(1 - \alpha_B) \qquad 2.4.17$$

the drained bulk modulus K_d is a function of the specified poroelastic parameters. In this case it is the Young's modulus E_d and Poisson's ratio ν_d. The various choices COMSOL allows as an input can be interchanged due to the mathematical relationship between the shear modulus, Poisson's ratio, and Young's modulus (Biot, 1941). Note that the Biot-Willis coefficient α_B is dependent solely upon the porous matrix properties while Biot's module depends on both the fluid and porous matrix properties. The body load is dependent upon angular frequency and fluid pressure, which also acts as a spherical contribution to the diagonal of the stress tensor resulting in (Biot, 1956):

$$\boldsymbol{F} = \frac{\rho_f}{\rho_c}\nabla p_f \qquad 2.4.18$$

And

$$\boldsymbol{s}_0 = \alpha_B p_f \boldsymbol{I}. \qquad 2.4.19$$

2.4.3 ACOUSTIC – POROUS BOUNDARY

Using the Multiphysics component of COMSOL, the pressure acoustics physics is combined with the poroelastic waves physics. It is assumed that at the interface, there is no loss between the two. Continuity of pressure on the boundary is (COMSOL, 2018):

$$(p_t)_{acoustic} = (p_t)_{porous} \qquad 2.4.20$$

The pressure load from the acoustics physics is set equal to the pressure experienced by the porous material through (COMSOL, 2018):

$$-\mathbf{n}(p_t)_{acoustic} = \mathbf{n} \qquad 2.4.21$$

These mathematical models with their accompanying boundary conditions are used to analyze the effects of an applied US field on cells *in vitro*.

2.4.4 MACROSCOPIC MODEL

Three-dimensional modeling of the system requires magnetic resonance images (MRIs) to be collected. These were imported to Simpleware ScanIP (Synopsys®, CA), a 3D image processing and model generation software, where the different tissues were segmented, and a finite element mesh analysis was done to smooth edges and corners and produce a 3D model. The output 3D mesh was then imported to COMSOL Multiphysics (COMSOL Multiphysics®, MA) where-after the acoustics physics package was applied. The output pressure from the KLM model was used as the initial pressure with time-harmonic dependence, $p(t) = p_0\sin(\omega t)$ as consistent with the function generator used to supply power to the transducer. To reduce the computational demand, the model is solved only on a section of the knee 12mm in height.

2.4.5 SENSITIVITY ANALYSIS

Modeling of the system was done in COMSOL Multiphysics which gets progressively more complex, beginning with *in vitro* modeling of a mesenchymal stem cell (MSC) or chondrocyte – which was used to find the optimal frequency at which to apply ultrasound – and evolving to a macroscopic model of a rabbit knee joint. An important part of the modeling setup is the mesh size. This specifies how many points within the model are solved for and defined as the maximum mesh element size. General guidelines for this are prescribed by COMSOL as a function of material velocity $c_{material}$ and operating frequency.

$$Mesh\ size = c_{material}/f/N \qquad 2.4.22$$

where the number of elements N was calculated through the use of a mesh refinement study so that a balance was struck between computational energy and sufficient data collection. The higher the number of elements, the more memory is required to solve. COMSOL prescribes this value to be anywhere from 1 to 5. These sensitivity analysis results differed for the various geometries but generally N was no more than three. In cases where N was not large enough the solutions did not converge. As the mesh size is dependent on material properties as well as applied physics, it is important to obtain accurate values. Parameters used in the pressure acoustics module are listed in Table 2.

Tissue	Sound velocity (m/s)	Density (kg/m^3)	Reference
Marrow	1410	990	Kawasaki 2015, Hughes 2007
Bone	3844	1900	Weiss 2000, Cameron 1996
Cartilage	1658	1473	Myers 1995, Basser 1998

Meniscus	1640	1470	Basser 1998
Fat	1470	950	Madsen 1978, Martin 1994
Muscle	1550	1073	Feigin 2020, Kuthe 2016
Skin	1645	1020	Moran 1995, Liang 2009
Blood	1575	1055	Azhari 2010

Table 2: Speed of sound and density values for tissues in the 3D modeling environment.

For acoustic pressure propagation through the system two options were available: the pressure acoustics module and the poroelastic waves module. Both modules were used to solve the wave equation with different boundary conditions, resulting in a system of partial differential equations. Many studies have presented extensive derivations of the wave equation, which has been briefly reviewed here (Green *et al*., 1976).

2.5 THEORETICAL MODELING

2.5.1 *IN VIVO* MODELING TO DETERMINE THE OPTIMAL FREQUENCY

Traditionally a frequency of 1.5MHz was used for most US treatments, regardless of tissue type and injury (Lai *et al*., 2021). Louw *et al* (Louw, *et al*., 2013) provided important information on the role of US frequency on the cellular response. In an experimental study chondrocytes were suspended in an aqueous medium and the bioreactor was exposed to US at different frequencies. A significant increase in the expression of c-Fos was observed at 5±0.5 MHz, compared to frequencies at 2 and 8MHz. The *in vitro* study was complemented by a mathematical model of the response of a suspended chondrocyte to an US field. It turned out that 5MHz corresponds to the first resonance frequency of the cell. At 5±0.5 MHz, the impending US transfers mechanical energy to the cell, which causes an increase in ERK phosphorylation and the upregulation of SOX9 expression (Sahu *et al*., 2020). Motivated by these results, we conducted a computational study of chondrocytes in different surroundings to determine the first resonance frequencies. Chondrocyte models were confirmed from Miller et al., and expanded upon here with zonal variations and mesenchymal stem cell suspensions. The different conditions were: (1) chondrocytes suspended in medium, (2) a chondron (chondrocyte plus PCM – i.e. pericellular matrix) suspended in medium, (3) a chondron embedded in ECM– i.e. extra-cellular matrix), and (4) chondrons in ECM where the ECM is layered into a superficial zone, middle zone and deep zone. Suspended cell computational studies were also done on the MSC and the MSC in a blood clot.

As described previously by Miller *et al*., to keep the computational requirements to a minimum the geometry was scaled by minimizing the culturing environment by a height of $3\lambda/4$ and a width of $\lambda/2$ (Miller *et al*., 2017). The geometry for a chondrocyte and MSC (mesenchymal stem cell) were modeled as two concentric spheres of different diameters to represent the cytoplasm and nuclear compartments of a cell. The geometries where a cell was embedded in an ECM or blood clot were done as a cylindrical plug equivalent to Guilak and Mow with a height of 65μm and radius of 32.5μm (Guilak, Mow, 2000). The pericellular matrix thickness in the chondron (the chondrocyte, with a PCM layer around it, is termed a chondron) and chondron + ECM model was designated to be 2.5μm as in previous modeling since the sensitivity lies in the value of Young's modulus (Miller *et al*., 2017). The final *in vitro* model was of a partial cartilage biopsy punch differentiating the three zones of cartilage with an overall thickness of 0.3mm (Fox *et al*., 2009) containing a chondron in each layer. Since chondrocytes make up less than

2% of cartilage tissue (Hunziker *et al*., 2002), only one was embedded in each zone, though the spherical shape was maintained. In each model the cell is positioned at an antinode for each frequency; where the ultrasound source is positioned at the bottom of each cylinder. A complete set of tissue properties can be seen in Appendix C. The different *in vitro* modeling geometry setups can be seen in Figure 4.

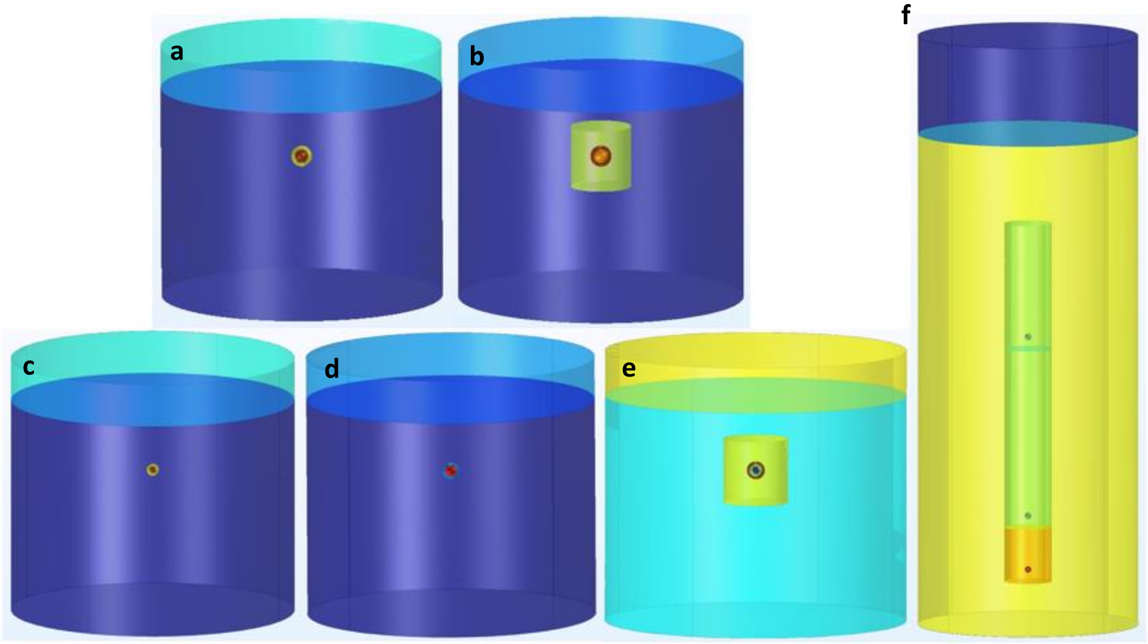

Figure 4: COMSOL in vitro cell geometries. a) a suspended MSC in water. b) a MSC embedded in a blood clot in water. c) a chondrocyte suspended in water. d) a chondron (chondrocyte with PCM layer) suspended in water. e) a chondron embedded in ECM in water. f) zonal differentiation of the ECM with chondrons embedded in each layer in water. The overall thickness of cartilage is broken up into zones as follows: superficial zone (SZ) 15%, middle zone (MZ) 50%, and deep zone (DZ) 35%.

Previous work done by Louw *et al*. (Louw *et al*., 2015) showed that a 5MHz transducer driven at a peak-to-peak voltage of 6V, produced a pressure of 14kPa. That pressure was used in *in vitro* modeling as the pressure amplitude in a boundary condition. Applying a parametric sweep by varying the frequency of the applied US field, the system attains a peak energy density at a specific frequency, which corresponds to the resonance value found here. The resulting storage energy density can be seen in Figure 5. Here, the frequency at which storage energy density peaks is referred to as the resonant frequency. Adding layers to the chondrocyte (+PCM, +PCM+ECM) or the MSC (+blood clot) shifts its resonance frequency. In Figure 5, the chondrocyte in suspension has a resonance frequency around 5MHz, confirmation of modeling done by Louw *et al*. (Louw *et al*., 2013). When the PCM layer is added, the resonance frequency of the chondron drops to 4.3MHz. This result is in agreement with Miller *et al*. where the maximum energy density lies in the range of 3.7 to 4.1 MHz for the chondron. When the chondron is placed in ECM, the resonance frequency is 3.8MHz, which is confirmation of modeling done by Miller *et al*. (Miller *et al*., 2017). The MSC in suspension has a resonance frequency of 2.3MHz, and in the presence of a blood clot it drops to 2.1MHz (Keep in mind the properties of an MSC and chondrocyte differ). The peaks at 6.4MHz are secondary resonance values. It is important to examine the effects of US on the MSC and its environment, as injuries and intentional creation of defects lead~~s~~ to a flood of blood from the bone which is rich in MSCs and nutrients. MSCs are stem cells which can differentiate into chondrocytes. As demonstrated in *in vitro* experiments by (Sahu *et al*., 2020), MSCs can differentiate into chondrocytes if they are exposed to a daily regimen of US. This is an important result, because in vitro chondrogenesis was always done by adding TGF-β to the culture medium. (In other words, the MSCs, which usually require chemical prompting by TGF-β to differentiate into chondrocytes, now differentiate only by mechanical prompting with US). Utilizing US as a stimulant can result in inducing chondrogenesis, which is examined further in Chapter Four. The response elicited by the cell is maximal at the peaks from Figure 5, though with changes in parameters there could be peak shifting. The results of Sahu *et al*. add another dimension to future clinical treatments (Sahu *et al*., 2019); treat patients immediately after injury with US that matches the resonance frequency of MSCs – this will expedite the formation of new chondrocytes. Then the treatment shifts to US treatments at the resonance frequency of chondrocytes to expedite cartilage secretion.

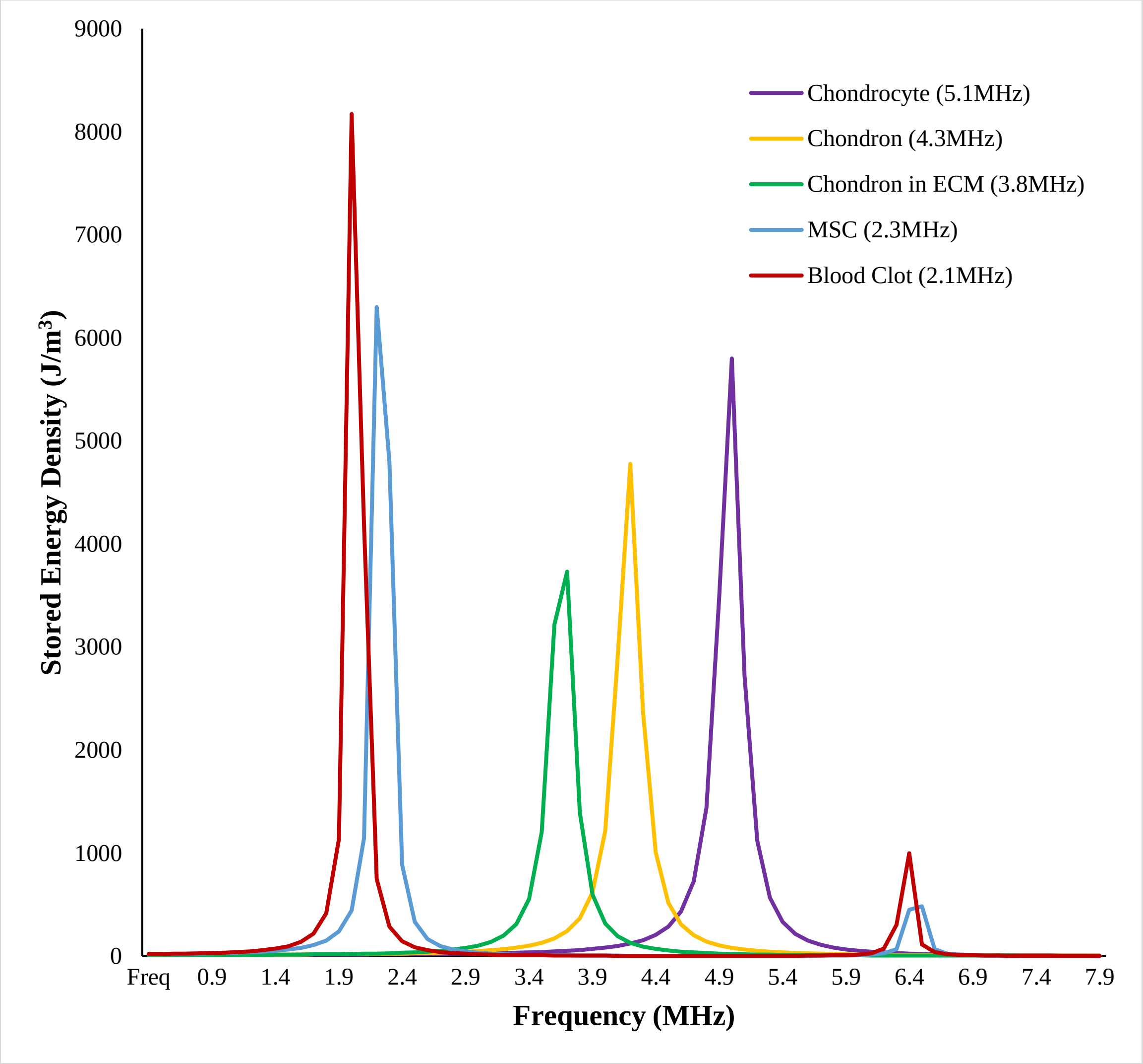

Figure 5: Resonant frequency plot for cell in vitro COMSOL simulations.

The three zones of articular cartilage are analyzed in the biopsy punch *in vitro* model in two separate scenarios where each have the same mechanical properties (SZP), and when the zones have their own specific properties (DZP) (Guilak *et al*., 2005). Again, applying a parameter sweep with varying frequencies the results show a shift in resonant frequency to 3.6MHz, within the range found by Miller *et al*. (Miller *et al*., 2017). Figure 6 below shows the resonant frequency and pressure results. It is important to note that even with different zonal properties the peak pressure still lies at 3.6MHz. This further illustrates that utilizing the optimal frequency results in efficient energy coupling. The broad spectrum of resonant frequencies with the DZP is promising for macroscopic models as the addition of more tissues will shift the peaks.

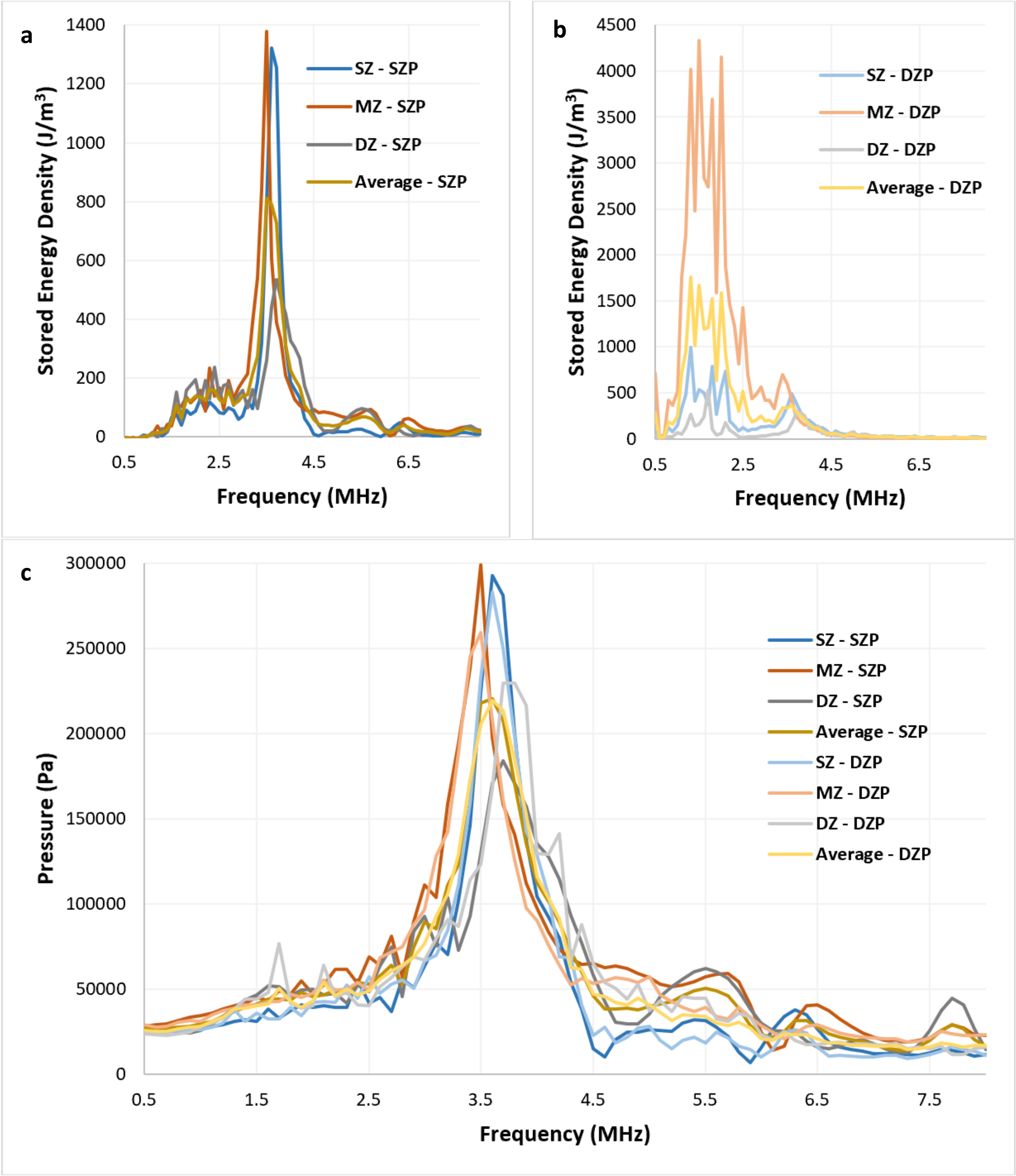

Figure 6: COMSOL biopsy punch results for a) SZP resonant frequencies, b) DZP resonant frequency, and c) peak pressure for both SZP and DZP.

The modeling of the chondrocyte in different environments to determine the resonance frequency was key in determining the transducer parameters for the experimental work. Based on the results of the *in vitro* modeling and available transducers from Olympus, resulted in the selection of a 3.5MHz transducer with a 0.25" diameter calibrated to 3.8MHz. The operating peak to peak voltage was set to 3.5Vpp. The model that was used to calculate the pressure at the transducer surface, as a function of applied voltage, is the KLM model. A KLM model calibrated by previous experiments shows how the new 3.8MHz transducer pressure output changed to 3kPa due to the decrease in transducer diameter by half, compared to the results of Louw *et al*. (Louw *et al*., 2015). **The frequency of 3.8 MHz and pressure of 3 kPa were then used in a macroscopic model of the rabbit knee.**

2.5.2 COMPUTATIONAL STUDY OF US PROPAGATION IN A KNEE

To answer the second question (cf. section 2.2), a finite element method (COMSOL) is used to solve for the governing equations in the solution domain. High resolution MRI pictures (DICOM files) are imported into ScanIP (Simpleware). ScanIP is a robust 3D image segmentation software that generates high-quality models through user manipulation. In ScanIP the different subdomains are defined; these subdomains include bone, muscle, synovial fluid etc. Each tissue has its own unique coloring which can be segmented through a threshold application. For humans the software has an autosegmenting function, which could not be used here due to the small dimensions of the rabbit anatomy. Once a tissue has been identified and isolated, ScanIP creates a finite element (FE) mesh which can be refined and smoothed without compromising the topology of the geometry. The time it takes to generate a final model depends on how complex the geometry is and how many iterations the user inputs. Figure 7(c) shows the finite element model of the bone segment and Figure 7(d) is the FE model of the combined domain. An overview of this process can be seen in Figure 7. A high resolution (9T) MRI scanner was used to obtain the DICOM file in Figure 7(a).

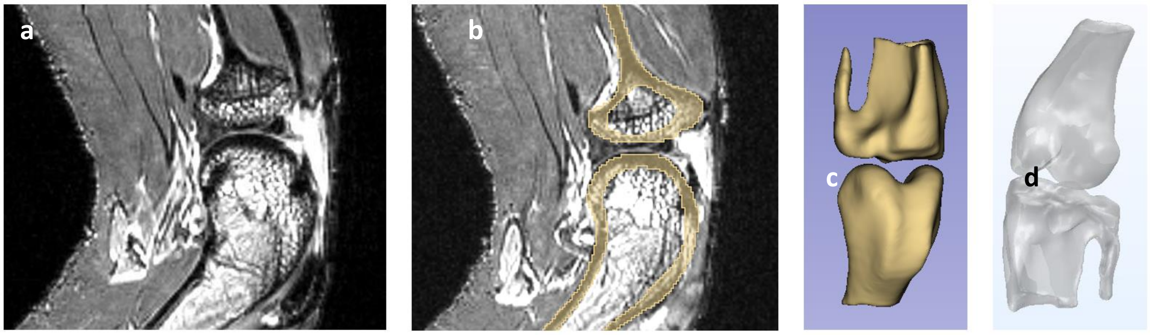

Figure 7: Workflow from ScanIP to COMSOL. a) raw slice from ScanIP. b) segmented bone tissue in ScanIP. c) 3D FE mesh generation from ScanIP. d) ScanIP FE mesh import to COMSOL with cartilage, muscle, and skin layers

A useful feature of ScanIP is that the final mesh can be exported directly into a COMSOL file, which is imported to the COMSOL geometry branch where the finite element model can be further manipulated. In this model the femur has been extruded and Boolean operations have been used to add a 0.3mm layer which is designated as cartilage tissue. The final 3D model, which also defines the domain on which COMSOL solves the governing equations, is shown in Figure 8 (the height of the cylinder in Figure 8 is 12 mm). Note the cartilage layer shown in Figure 8. Surrounding the joint is muscle tissue with a final outer skin layer. The diameter of the model in Figure 8 is 30mm (this value was determined by the dimensions of the axial views in ScanIP). A cylindrical indentation in the skin is placed in line with the joint space to mimic transducer placement, as seen in Figure 8. Pressure acoustics is applied to the skin and muscle tissue as linear elastic materials, and poroelastic wave theory is applied to the cartilage and bone tissues in COMSOL modeling as has been commonly done (Baron *et al.*, 2017). Complete material parameters can be found in the Appendix C material.

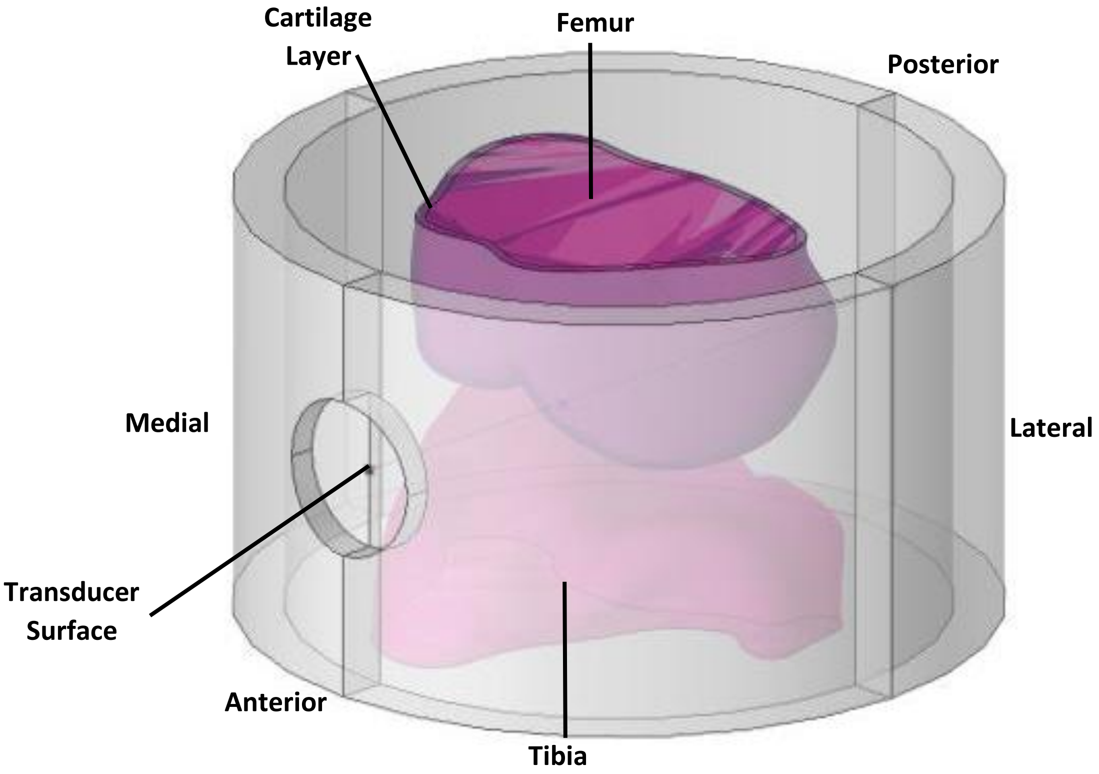

Figure 8: Annotated finite element COMSOL model of the rabbit knee anatomy. The space between the femur/tibia and the inner cylinder surface is filled with muscle tissue, and the outermost layer is skin tissue.

2.5.3 RABBIT JOINT MODEL IN 3D FREQUENCY SPACE

Preliminary modeling on the joint allowed for the final condensed geometry to be used. Compared to the sectioned joint in Figure 7c, the final model in Figure 8 is a small portion. COMSOL has a mesh refinement study which was used to determine how detailed the muscle and skin tissue should be. A finer mesh was used along the centerline of the transducer to capture in better detail the wave propagating through the joint space, including the effects on the cartilage. The resulting mesh contains millions of elements and varies when different frequencies are used, since the element size is frequency dependent.

The efficacy of ultrasound for cartilage regeneration has been much studied and debated (Loyola-Sánchez *et al*., 2010). Variability of results can be explained by a myriad of reasons, primarily that the operating frequency is non optimal. A clinical study was done with a 1MHz pLIUS (pulsed low-intensity ultrasound) regimen which resulted in ambiguous results (Karakaş *et al*., 2020). Pulsed US was applied to a general area of the knee while flexed. When compared to patients who had no US application there were no significant differences. Another clinical study of 1MHz was done by Loyola-Sanchez *et al*. and showed promising results though further studies are required to optimize US operations (Loyola-Sánchez *et al*., 2012). Theoretical modeling is a useful tool to minimize the trial-and-error approaches to determine the optimal operating conditions. Another reason for lower efficacy is the placement of the transducer. The placement of the transducer must be directed by the specifics of the anatomy, in other words the MRI should be used to choose the position where the transducer is placed. Incorrect position of the transducer could cause a lower intensity at the defect site and the US treatment would not induce the beneficial bioeffects (Feng *et al*., 2010). To summarize the factors that played a role in the ambiguous outcomes; the frequencies which were used lay outside the resonance range, pLIUS regimens deliver much lower pressures than cLIUS, and the optimal placement of the transducer must depend on an individual's anatomy.

Comprehensive modeling in COMSOL could circumvent the efficacy issues by utilizing patient-specific anatomy. Theoretical modeling is beneficial in first deciding if US could be therapeutic to the patient. The aim of US is to expedite the healing process of the tissue. Therefore, a best practice can be developed by using the COMSOL model to study US propagation through the joint space and optimize the transducer position to minimize the number of different tissues in the wave's pathway and to minimize the pathlength. Figure 9 depicts these results using the standard 1.5MHz (a-c) versus 3.8MHz (d-f). The 3D model results are interpreted along the centerline in 2D to clearly understand the system response at the center of the transducer.

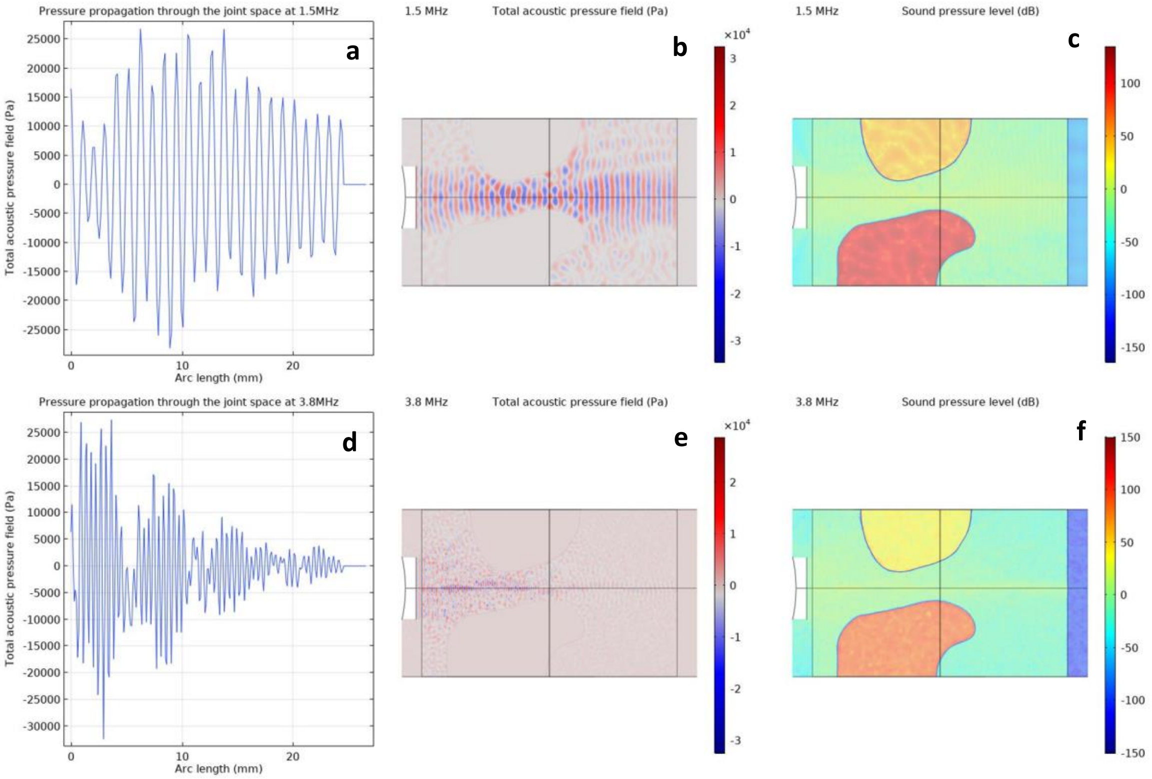

Figure 9: COMSOL results from complete rabbit geometry comparing 1.5MHz US (a-c) with 3.8MHz (d-f). Panels a) and d) show the pressure propagation through the joint space on the transducer centerline. b) and e) show the pressure field in a slice of the geometry. c) and f) show the sound pressure level through the joint space

In further simulations using the settings obtained for a 3.8MHz transducer with 3kPa pressure output, the position of the transducer was placed in line with the defect site (on the surface of the femur) to simulate the conditions which were used in rabbit experiments. Figure 10 shows the pressure propagation results.

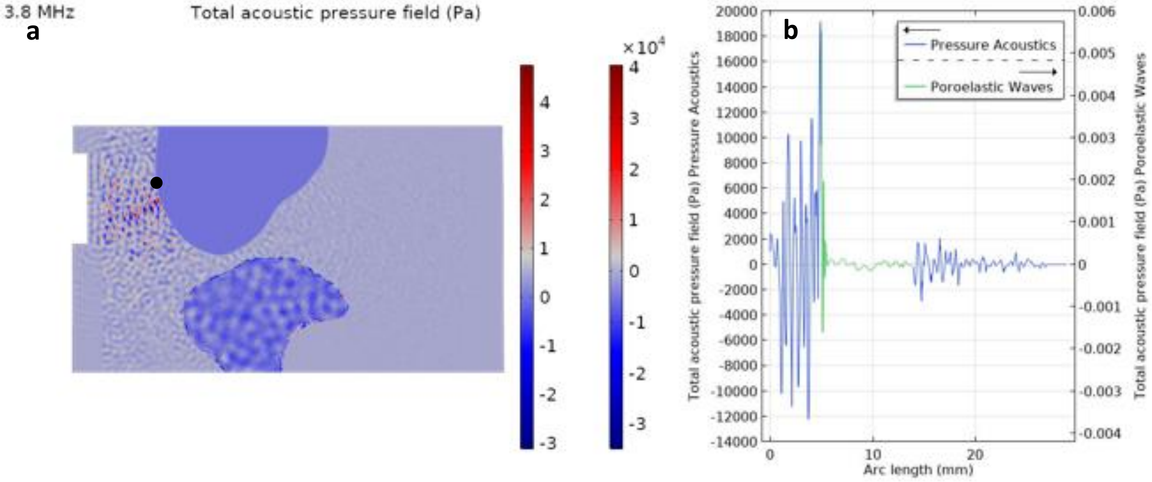

Figure 10: COMSOL results from complete rabbit geometry with transducer in line with femur surface. a) shows the pressure field in a slice of the geometry where the left scale is for the bone and cartilage and the right shows the scale for the muscle and skin. The black dot denotes where the defect site would lie approximately. b) shows the pressure propagation along the transducer centerline through muscle and skin (blue) and cartilage and bone (green).

As shown in Figure 10(b) there is a large difference in the pressure signal in the muscle tissue versus cartilage and bone. The surface plot in Figure 10(a) does not show these differences in pressure so clearly. The pressure at the surface of the cartilage tissue is approximately 16kPa and rapidly declines to a low value that is almost not detectable upon entering the bone. This is a result of the difference in the acoustic impedances of the muscle, cartilage, and bone.

The pressure acoustics module in COMSOL was used to study the role of the transducer on the pressure field in the knee, and specifically at the injury site. This was done on a simple anatomical structure existing only of muscle and bone tissues.

Transducer placements at the front of the knee (anterior), back (posterior), and side (lateral) were examined where the disparity of pressure at the transducer face and the defect site were minimized in the anterior case.

2.6 DISCUSSION OF THE 3D MODELING

Theoretical modeling in 3D gives a better understanding to what the surface of the bone is exposed to, since its topology is not uniform. As the bone extends away from the transducer the pressure decreases. Visualizing this in 3D is important for optimal transducer position selection. Here the transducer has a small diameter which will not create a uniform pressure distribution at the surface of the bone.

For future transducer selection for optimal patient applications, one must also consider how the transducer diameter, frequency, and voltage affect the near field range. In this range the pressure distribution is unpredictable and therefore results in variable defect site pressures. The approximate near field distance can be calculated by (Kinsler *et al.*, 2000)

$$L_{Nf} = d^2 f / 4u \qquad 2.6.1$$

where d is the diameter of the transducer and u is the material sound velocity. In this case we will specify the muscle as the material as it makes up the bulk of the material in the model. The resulting near field distance is calculated to be 24.7mm which is almost the entire diameter of the rabbit knee. In the case of the 1.5MHz transducer, the near field is 9.8mm assuming that the diameter of the transducer is constant. Both frequency and diameter affect the depth of the near field.

The cLIUS results are obtained from steady state calculations. In this case, the US is applied sufficiently long that a steady state is reached. Usually, the steady state is reached after the wave has traversed the domain several times. In this case, the domain is three-dimensional, but if you consider the direction normal to the center face of the transducer, the distance to the knee surface is approximately 30 mm. At an approximate speed of sound (it varies between tissue types) of 1500 m/s, it takes about $40\ \mu s$ to traverse the domain twice to reach the transducer again. pLIUS treatment is a 1kHz cycle, with $200\ \mu s$ active and $800\ \mu s$ rest periods per duty cycle. Based on the estimates, about 5 passes can be fitted into one active period. All US dampens completely during the rest period, so each active cycle will be a repeat of the previous one. Again, we iterate that the domain is 3-D and it takes more than 5 passes to reach the steady state. In other words, the pressures one observes with pLIUS will always be lower than the steady-state values of cLIUS.

COMSOL is computationally much more intensive to solve the transient (i.e. pLIUS) case. The code uses an adjustable time step, and considerably more memory is required to integrate the equations. Just to set some perspective, it takes about 4 hours to solve the steady state problem on the Holland computer center at UNL, but the transient problem, modeling only the first 33 $\mu s,$ takes more than 24 hours. Now this time does not allow for a wave to travel across the domain and back to the transducer. Since the Biot theory is also computationally more demanding, we were not able to model pLIUS with Biot theory, but we had to rely on the linear elastic model. Therefore, we first ran the less demanding steady state problem for both models. The transducer frequency is 1.5 MHz.

The rational for this choice of frequency is the standard US application regimen is usually done at 1.5MHz.

2.6.1 cLIUS RESULTS

In Figure 11 the steady state problem has been solved using Biot theory (left) and the linear elastic model (right). The pressure field appears more scatted in the linear elastic model, but more important, the range in which the pressure oscillates does not differ that much. This point is better illustrated in Figure 12 where the pressure along the straight line from the transducer center to the opposite free surface is plotted.

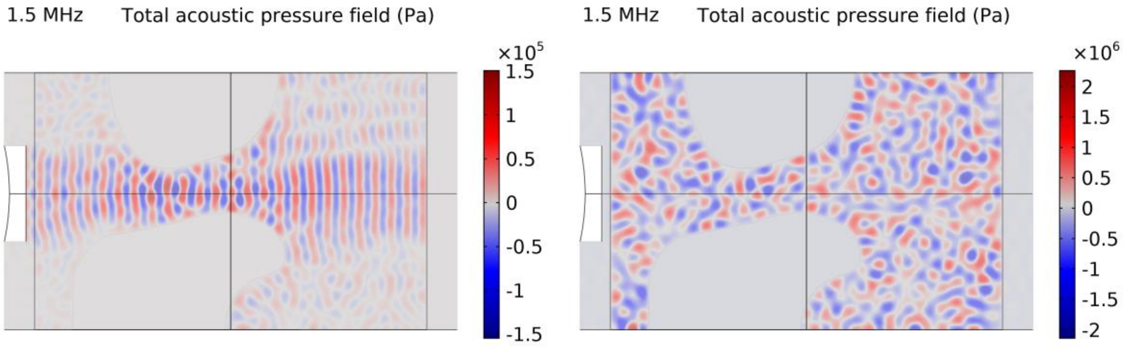

Figure 11: Comparison of the acoustic pressure field in COMSOL acoustics packages. Left: steady-state pressure field in the knee using Biot theory. Right: steady-state pressure field using linear elastic physics.

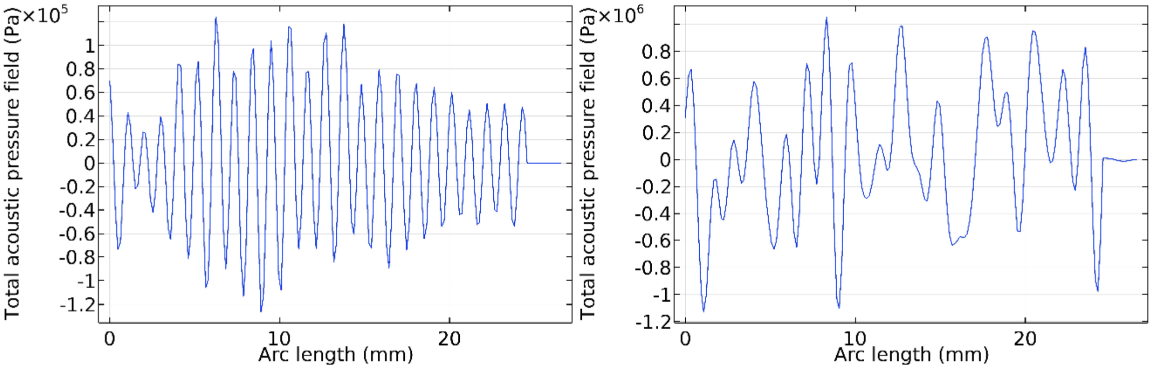

Figure 12: Comparison of pressure propagation along the transducer centerline. Left: The steady state pressure vs. position, using Biot theory. Right: The steady state pressure vs. position using

the linear elastic model. Position is measured from the center of the transducer to the opposite free end of the knee.

The linear elastic model produces a more scattered plot, whilst one recognizes the near-field and transition to the far-field in the Biot theory plot. Generally speaking, the pressures are approximately five-fold higher in the linear elastic model, but this can be explained by the fact that the Biot theory also accounts for damping in both phases, which is not the case for the linear elastic model. Thus, we make the case that the two models produce pressures of the same order of magnitude, factoring in the effect of damping.

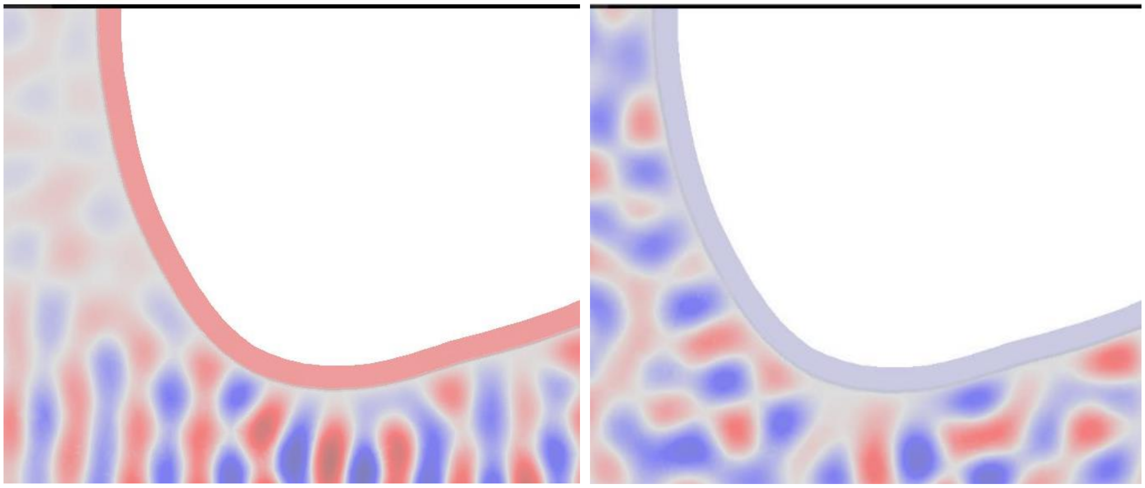

Figure 13: Enhanced steady-state pressure at the muscle-cartilage interface. Left: The steady state pressure at the cartilage/bone interface, using Biot theory. Right: The steady state pressure at the cartilage/bone interface using the linear elastic model.

The cartilage is only 300 μm thick, which is less than one wavelength, therefore it is more important to focus on the pressure at the muscle/cartilage interface. Although differing quantitatively, the pressure at this interface is qualitatively similar for the two models, albeit lower pressure for the Biot model due to damping. ***Therefore, we conclude from the results in this section that Biot models and linear elastic theory give***

qualitatively similar results, and the match would be even better if damping is added to the linear elastic model.

2.6.2 pLIUS RESULTS

As mentioned before, the pLIUS results are all based on the linear elastic model. In the following section we will present the pLIUS results, but keep in mind that Biot results for pLIUS are expected to look similar, but the computation is too expensive for the available resources. In Figure 14 we show a series of snapshots at different points in time. These snapshots provide insight of the active part of the duty cycle.

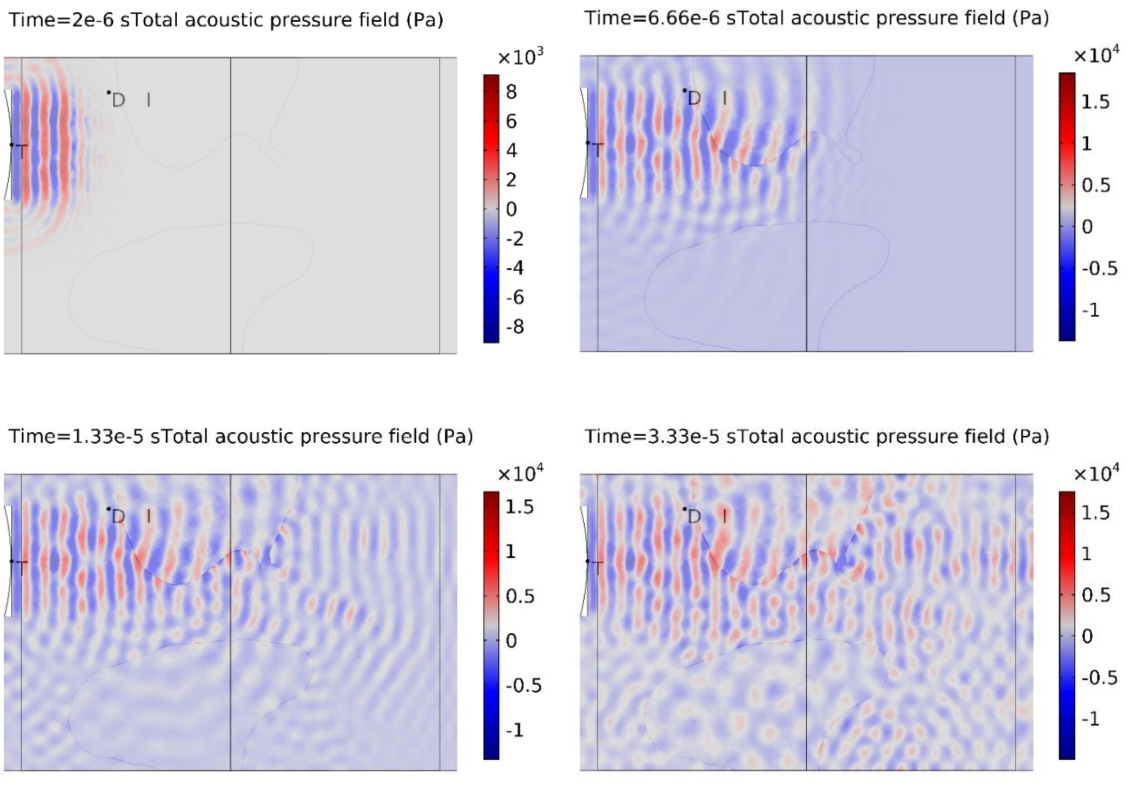

Figure 14: Panel of snapshots to show the progression of the pressure field at the start of the active part of the duty cycle. From top left, ant-clockwise, the pressure fields are shown at 3P, 10P, 20P and 50P. P is the time of one period in the muscle, which is approximately 20 μs. The position of the defect site is marked by D on the plots, and I denotes a point lying inside the bone.

Even at 50P, the leading part of the wave has not returned from the free surface of the knee to reach the transducer again. In other words, the incident and reflected waves have not established a final steady state pattern. The active part is 200 μs, and it is expected that the pressure field near the end of the active part will approach the steady state, since 5 passes back and forth across the centerline of the domain would be completed by then.

We can conclude from the results in Figure 14 that the pressure field builds up during the active part of the duty cycle of pLIUS and only reaches the steady state values towards the end of the active stage. In comparison to cLIUS, we can safely say that the pressure field in pLIUS is significantly lower. If the pressures during the active stage are averaged over the duration of the active part, we estimate the values are at least one order of magnitude less than in the case of cLIUS. Therefore, from a therapeutic standpoint, pLIUS would be less effective than cLIUS to induce the mechano-chemical reactions in cells which lead to enhanced secretion of ECM, suppression of inflammation markers and directing MSCs to chondrocytes.

2.7 ONE-DIMENSIONAL MODEL

The rationale for a one-dimensional model is the high computational cost associated with the 3D model, which must be performed with licensed software on a high-performance computer. Also, the annotation of the MRI scans to demarcate the zones of tissue/bone/muscle/cartilage is a very labor-intensive task. All these factors, in combination, have the practical consequence that clinical applications of 3D modeling remain a goal for the future, but in the intermediate we need to find more practical compromises. In Figure 15 a small cylindrical domain is marked, that connect the center of the transducer with the injury site. A one-dimensional model is used to describe the propagation along this cylindrical section. The model can also be used to provide an estimate of the energy dissipation and the temperature rises along the cylinder.

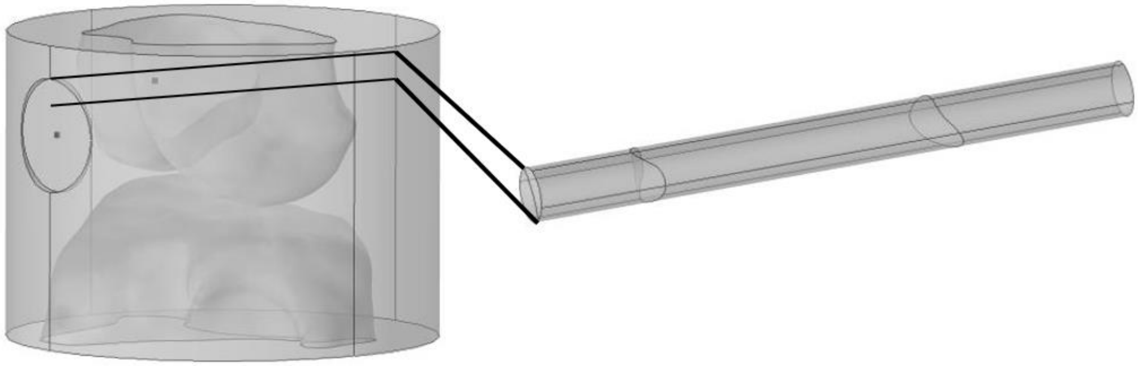

Figure 15: Representation of tissue-bone-tissue domains used in 1D modeling from 3D. This shows the transition from tissues at designated intervals where the face of the bone is in line with the transducer. The point on the surface of the bone shows an approximate defect site.

To start the discussion, consider a one-dimensional model of US propagation through a combination of bone and tissue. The domain is divided into tissue, $0 \leq x \leq L_1$, and bone, $L_1 \leq x \leq L_2$. The transducer is placed at $x = 0$, the edge of the tissue zone, and the receiver is placed at $x = L_2$. For both regions the damping is modeled by an internal dissipation model. The dimensionless propagation models have been scaled with $\tau = tf_r, z = xf_r/c_1$. The dimensionless domain is $0 \leq z \leq z_2$ and the interface between the tissue and bone region is at $z_2 \leq z \leq z_3$.The sound velocities and densities of the tissue and bone are c_1, ρ_1 and c_2, ρ_2. The reference frequency is $f_r = 3.8\ MHz$. The dimensionless damping coefficients are $\gamma_{1,2} = \nu_{1,2} f_r / c_1^2$.

2.7.1 NEAR-FIELD MODEL

Each point on a transducer serves as a source that transmits acoustic energy into the space ahead of it. Depending on the geometry of the overall body within which propagation can occur, flat-faced transducers typically transmit waves into a hemi-sphere.

The propagation from a point source is described by the wave equation in spherical coordinates. Using the driving radial frequency $2\pi f_r = \omega_r$ as a scale for time, and sound velocity c_0 to scale length, ω_r / c_0, the equation for the radial velocity is

$$\frac{\partial^2 u}{\partial \tau^2} = \frac{\partial^2 u}{\partial r^2} + \frac{2}{r}\frac{\partial u}{\partial r} - \frac{2u}{r^2} + \gamma \frac{\partial}{\partial \tau}\left[\frac{\partial^2 u}{\partial r^2} + \frac{2}{r}\frac{\partial u}{\partial r} - \frac{2u}{r^2}\right] \qquad 2.7.1$$

The damping coefficient depends on the kinematic viscosity ν and its dimensionless form is $\gamma = \nu\omega_r / c_0^2$. The analytical solution for a point source located at dimensionless radius R on the transducer, the radial velocity at a distance z from the transducer and $R = 0$, is

$$u(r,\tau) = Ae^{-i\omega\tau}\left[\frac{e^{\lambda r}}{r^2} - \frac{\lambda e^{\lambda r}}{r}\right].$$

The radius r is $r = \sqrt{(R^2 + z^2)}$. The dimensionless radial frequency is $\omega = f/f_r$. The wavenumber $\lambda = \lambda_r + i\lambda_i$ has a non-zero real part when damping is present.

$$\lambda = \left(\frac{-\omega^2(1 - i\omega\gamma)}{1 + \omega^2\gamma^2}\right)^{1/2} \qquad 2.7.3$$

The velocity potential is defined as $\nabla \mathrm{u} = \phi$ and its solution is

$$\phi = \phi_0 \frac{e^{\lambda r - i\omega\tau}}{r}$$

The pressure is

$$P = \rho_0 \frac{\partial \phi}{\partial \tau} = -\rho_0 i\omega\phi_0 \frac{e^{\lambda r - i\omega\tau}}{r}$$

The pressure on the transducer plate is $P_0 e^{-i\omega\tau}$.

$$P_0 = -\rho_0 i\omega\phi_0\lambda$$

$$P = P_0 \frac{e^{\lambda r - i\omega\tau}}{\lambda r}$$

The pressure at point $(0, z)$ on the centerline of the transducer is obtained from integrating over the transducer plate;

$$P = P_0 e^{-i\omega\tau} \int_0^{R_t} \frac{e^{\lambda r}}{\lambda r} \times 2\pi r dr = 2\pi P_0 e^{-i\omega\tau} \left[e^{\lambda \sqrt{z^2 + R_t^2}} - e^{\lambda z} \right]$$

$$u(0, z, \tau) = 2\pi C_1 e^{i\omega\tau} \int_0^{R_t} \left(\frac{e^{-\lambda r}}{r^2} - \frac{\lambda e^{-\lambda r}}{r} \right) \times \frac{z}{r} \times RdR \qquad 2.7.4$$

A plot of $Re(u(0, z, \tau))$ at fixed point in time is shown in Figure 16. The constant $C_1$is related to the medium sound velocity c_1, density $\rho_1$and the transducer's delivery pressure $p_0 = 3kPa$:

$$i \frac{c_1 \rho_1}{\omega} \lambda_1 C_1 = p_0 \qquad 2.7.5$$

In Figure 16 the pressure along the centerline is shown.

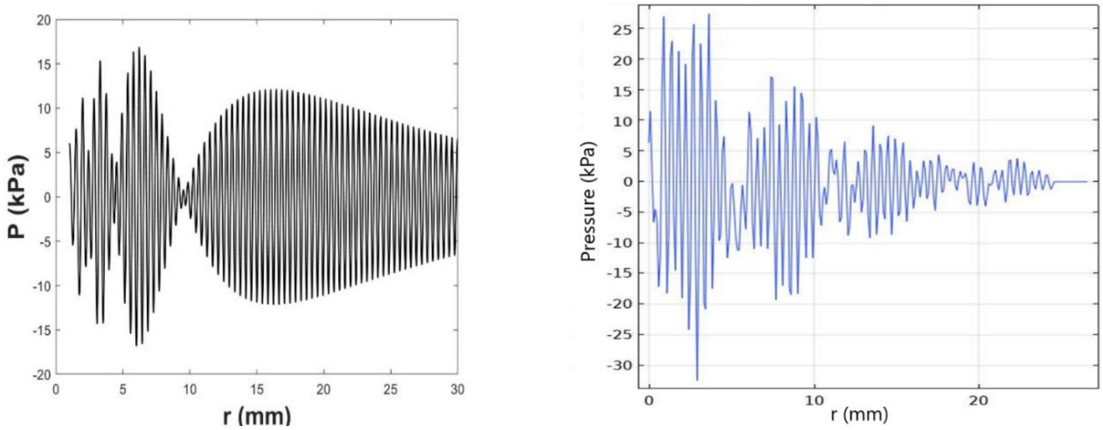

Figure 16: (Left) Pressure along the centerline of the transducer using eq.2.7.4. The attenuation coefficient is $\nu = 5 \times 10^{-4} m^2/s$*. (Right) The pressure on the centerline, retrieved from the solution of the 3D Biot theory model.*

Both the analytical and the 3D model show the constructive/destructive interference close to the transducer surface, but further away the 3D solution changes, due to the complexities of the domain with scattering and reflection of waves. At the transducer surface the pressure is $p_0 = 3kPa$, but it is amplified in the near-field due to the constructive interference of the point sources to reach a maximum of $P = 26kPa$ at a distance 3mm from the transducer (Figure 16(R)). The attenuation of the US field is a major concern, but two points need to be considered to bring more balance to this concern; the signal is amplified in the near-field and attenuation increases with frequency. Overall, the Biot model exhibits stronger amplification of the signal close to the transducer and stronger attenuation further away from the transducer, compared to the 1D model.

2.7.2 FAR-FIELD MODEL

In the case of the rabbit knee, the small transducer radius and the diminutive anatomy have the combined effect that most of the knee lie in the near-field. However, larger transducers will be used in human applications and it is expected that in many cases the far-field conditions are appropriate.

Tissue

$$\frac{\partial^2 u}{\partial \tau^2} = \frac{\partial^2 u}{\partial z^2} + \gamma_1 \frac{\partial^3 u}{\partial z^2 \partial \tau} \qquad 2.7.6$$

Bone

$$\frac{\partial^2 v}{\partial \tau^2} = \left(\frac{c_2}{c_1}\right)^2 \frac{\partial^2 v}{\partial z^2} + \gamma_2 \frac{\partial^3 v}{\partial z^2 \partial \tau} \qquad 2.7.7$$

We kept the velocities and pressures dimensional. The pressures in the tissue and bone regions are related to the velocities as follow;

$$\frac{\partial P_1}{\partial \tau} = -c_1 \rho_1 \frac{\partial u}{\partial z} \qquad 2.7.8$$

$$\frac{\partial P_1}{\partial \tau} = -c_2^2 \rho_2 / c_1 \frac{\partial v}{\partial z} \qquad 2.7.9$$

The solutions are;

$$u = C_1 e^{i\omega\tau + \lambda_1 z} + C_2 e^{i\omega\tau + \lambda_2 z} \qquad 2.7.10$$

$$v = C_3 e^{i\omega\tau + \beta_1 z} + C_4 e^{i\omega\tau + \beta_2 z} \qquad 2.7.11$$

The dimensionless radial frequency is $\omega = 2\pi f / f_{ref}$, the wavenumbers λ, β are complex;

$$\lambda_{1,2} = \left(\frac{-\omega^2 (1 - i\omega\gamma_1)}{1 + \omega^2 \gamma_1^2}\right)^{1/2} \qquad 2.7.12$$

$$\beta_{1,2} = \left(\frac{-\omega^2 \left(\left(\frac{c_2}{c_1}\right)^2 - i\omega\gamma_2\right)}{\left(\frac{c_2}{c_1}\right)^4 + \omega^2 \gamma_2^2}\right)^{\frac{1}{2}} \qquad 2.7.13$$

If the damping coefficients were zero, then $\lambda_1 = i\omega, \lambda_1 = -i\omega$ and $u_F = C_2 e^{i\omega(\tau - z)}$ and $u_R = C_1 e^{i\omega(\tau + z)}$ are easily identified as the forward and backward propagating wave. This distinction still holds for the damped case, $u = u_F + u_R$.

The boundary condition at $z = 0$ describes the external forcing.

$$i\frac{c_1\rho_1}{\omega}(\lambda_1 C_1 + \lambda_2 C_2) = P_0 \tag{2.7.14}$$

At $z = z_1$, continuity of u and P is imposed;

$$C_1 e^{i\omega\tau+\lambda_1 z_1} + C_2 e^{i\omega\tau+\lambda_2 z_1} = C_3 e^{i\omega\tau+\beta_1 z_1} + C_4 e^{i\omega\tau+\beta_2 z_1} \tag{2.7.15}$$

$$C_1\lambda_1 e^{i\omega\tau+\lambda_1 z_1} + C_2\lambda_2 e^{i\omega\tau+\lambda_2 z_1} = \frac{\rho_2 c_2^2}{\rho_1 c_1^2}\left(C_3\beta_1 e^{i\omega\tau+\beta_1 z_1} + C_4\beta_2 e^{i\omega\tau+\beta_2 z_1}\right) \tag{2.7.16}$$

At z_2 a stress-free condition is applied.

When another tissue region is added behind the bone, $z_2 \leq z \leq z_3$, similar continuity conditions are imposed at the second interface z_2 and the stress-free condition is applied at z_3. In Table 3 parameter values are listed for the examples which are presented next.

Type	C_P (J/kg K)	Longitudinal sound velocity, c (m/s)	Density, ρ (kg/m^3)	Thermal conductivity, k (W/mK)
Tissue	3,500	1550	1073	0.7
Bone	1,260	3844	1900	0.56

Table 3: Parameter values for tissue and bone.

In Figure 17 the velocity and pressure are shown in the tissue-bone-tissue domain for $\gamma_1 = \gamma_2 = 0.0028$. The frequency is $f = 3.8\ MHz = f_r$. The width of each region is set to approximate values obtained from rabbit MRIs with distances of $5mm, 12\ mm,$ and $30mm$.

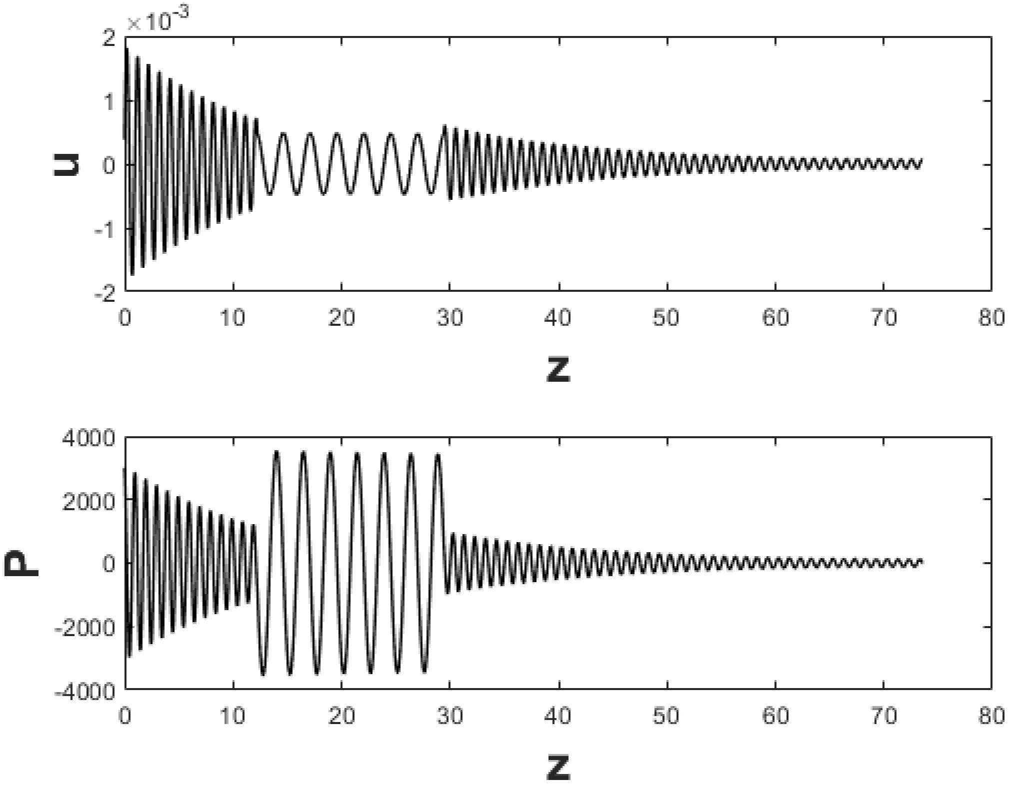

Figure 17: Velocity and pressure in the tissue-bone-tissue domain at f = f_r.

The largest velocity decrease occurs in the first tissue region and is negligible in the bone region. The pressure amplitude also drops in the first tissue region, no change in the bone region and a notable reduction when the second tissue region is entered. Next, we consider a similar configuration at $f = 1.5MHz$ in Figure 18.

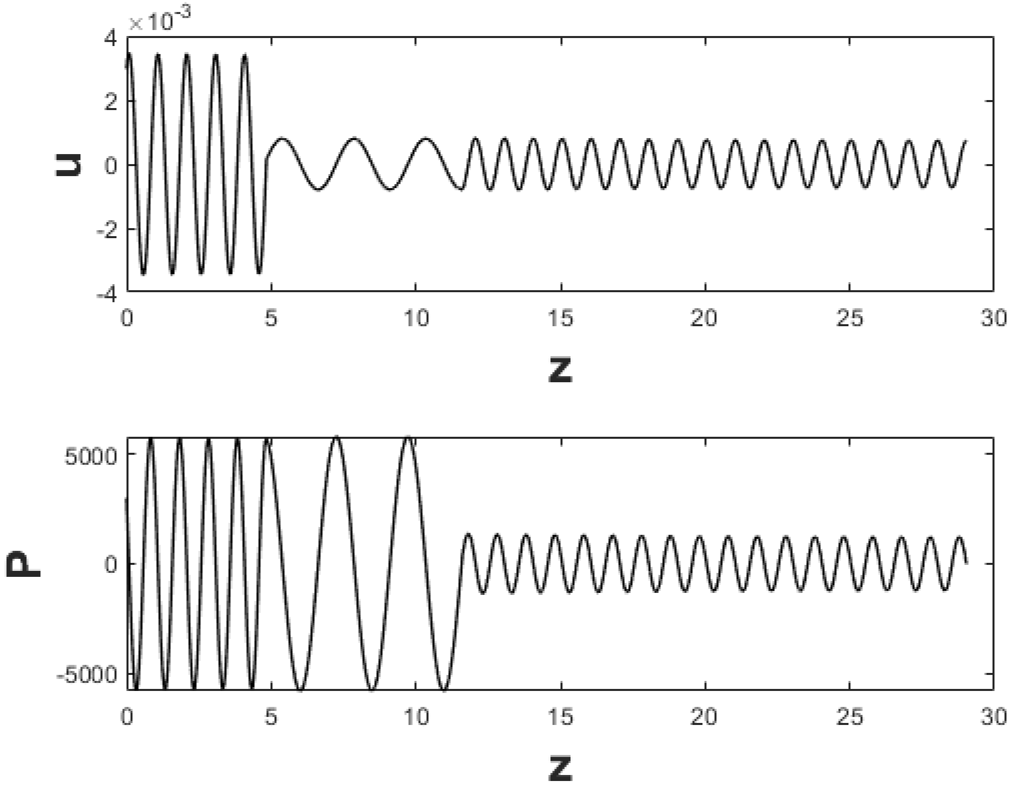

Figure 18: Velocity and pressure in the tissue-bone-tissue domain at f = 1.5MHz.

The dampening is much lower than for the previous case. The drops in particle velocity occurs at the tissue/bone, while we see a decreased velocity and pressure in the second tissue domain. When the damping coefficients in the tissue is increased tenfold, for $\gamma_1 = 10\gamma_2 = 0.028$, the pressure and velocity are strongly damped in the first region, despite the fact that the frequency is *f =1.5MHz*. The results are shown in Figure 19.

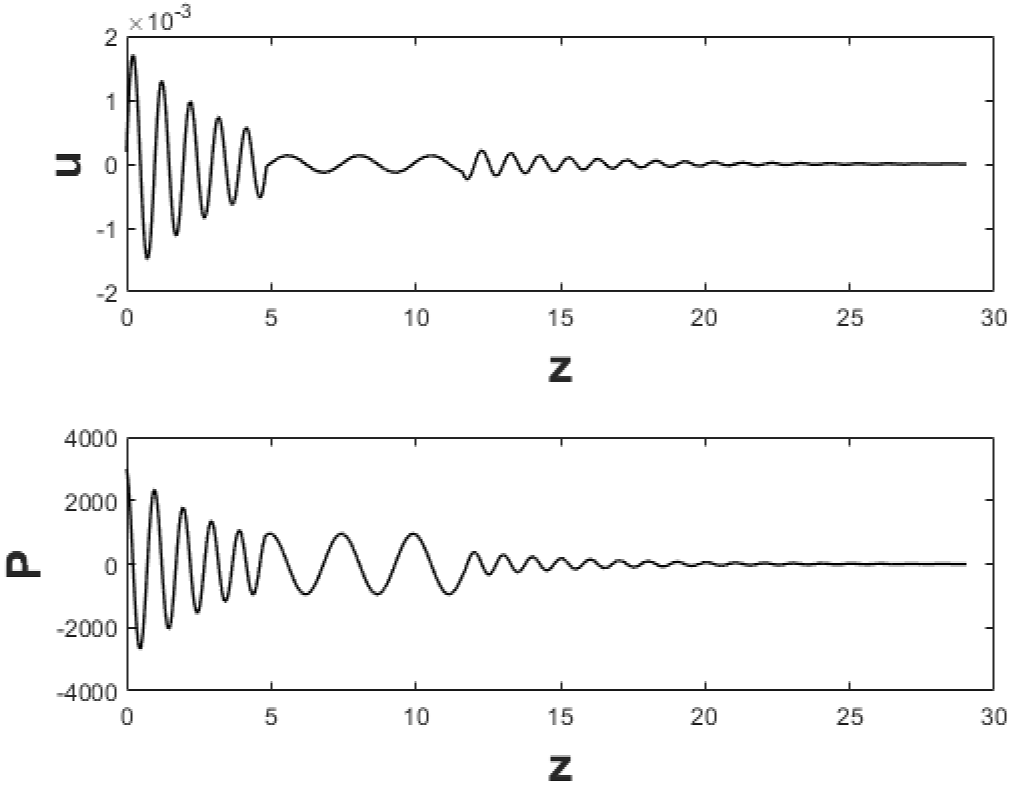

Figure 19: Velocity and pressure in the tissue-bone-tissue domain at f = 1.5MHz for increased γ_1.

Next the damping coefficient in the bone is increased tenfold, $10\gamma_1 = \gamma_2 = 0.028$. The results are shown in Figure 20. The damping is much weaker in the first tissue region, and the pressure in the second bone region is also much stronger, although the damping coefficient in the bone region is tenfold higher.

The overall trends are that the damping coefficient of the tissue is the most important factor that affects the intensity of the US field throughout the domain. Secondly, and consistent with internal damping mechanisms, stronger damping occurs at higher frequencies.

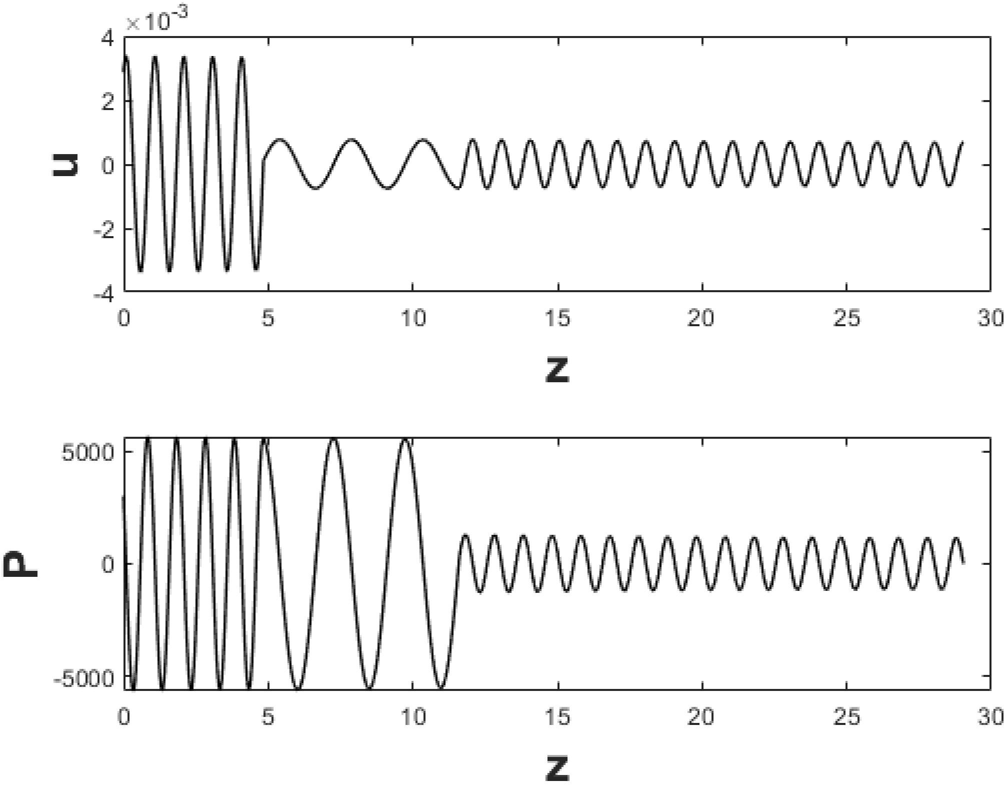

Figure 20: Velocity and pressure in the tissue-bone-tissue domain at f = 1.5MHz for increased γ_2.

If the objective of an US therapy is to deliver US to an injury site at z_1, i.e. the interface of the first tissue region and the bone, then the damping in the first tissue region plays the key role in determining the US intensity at the treatment site. As shown in Figure 19, the US is almost completely annihilated in the bone and second tissue region, but there is still a good field strength at z_1. Note in this case the frequency is *f = 3.8MHz* .

The analysis clearly demonstrates that it is very misleading to assess the US intensity at z_1, based on measurements at z_3. Oftentimes researchers will place a receiver at z_3 to compare the input with the signal at the other end of the domain. This underscores the importance of the model.

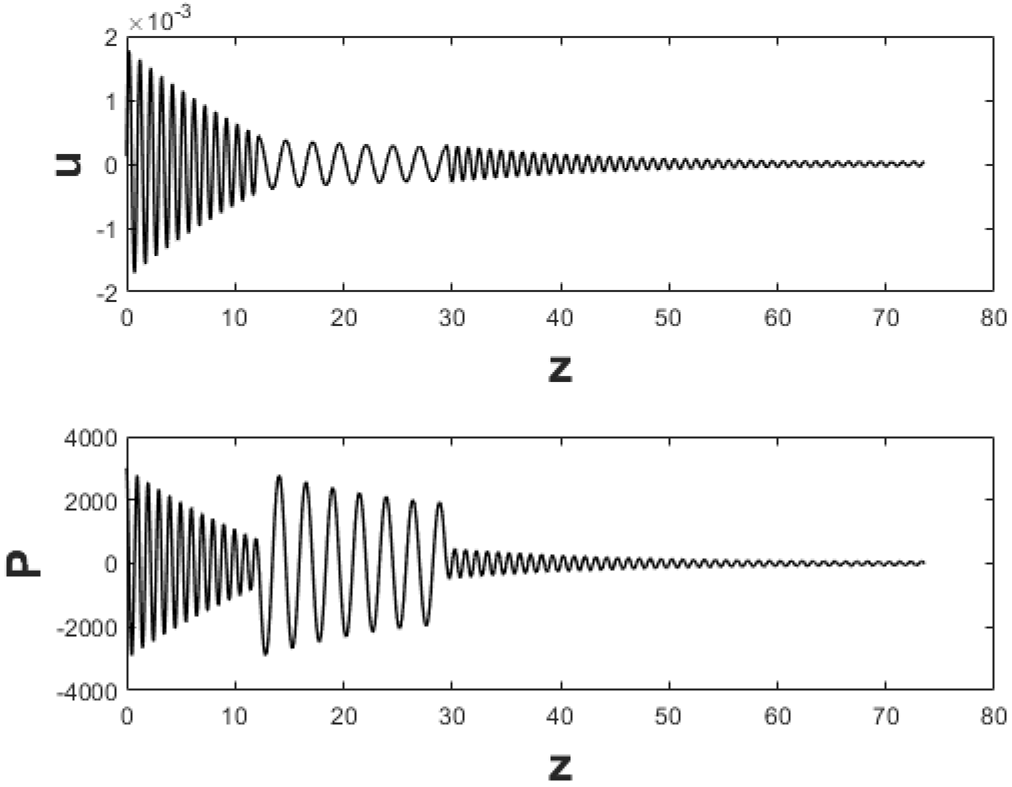

Figure 21: Velocity and pressure in the tissue-bone-tissue domain at f=f_r for increased γ_2.

2.7.3 ENERGY DISSIPATION

Damping is an irreversible energy transfer from the US field to the internal energy of the material (bone or tissue). The rate of dissipation is

$$W_1 = \gamma_1 f_r \rho_1 \bar{u}^2 \qquad 2.7.17$$

and

$$W_2 = \gamma_2 f_r \rho_2 \bar{v}^2 \qquad 2.7.18$$

And $\bar{u}^2$, $\bar{v}^2$ denote the forward and reverse components of the velocity in each region, multiplied with their complex conjugates. In Figure 22 the dissipation and pressure are shown for $\gamma_1 = 0.0014, \gamma_2 = 0.0028$ and $f = f_r$.

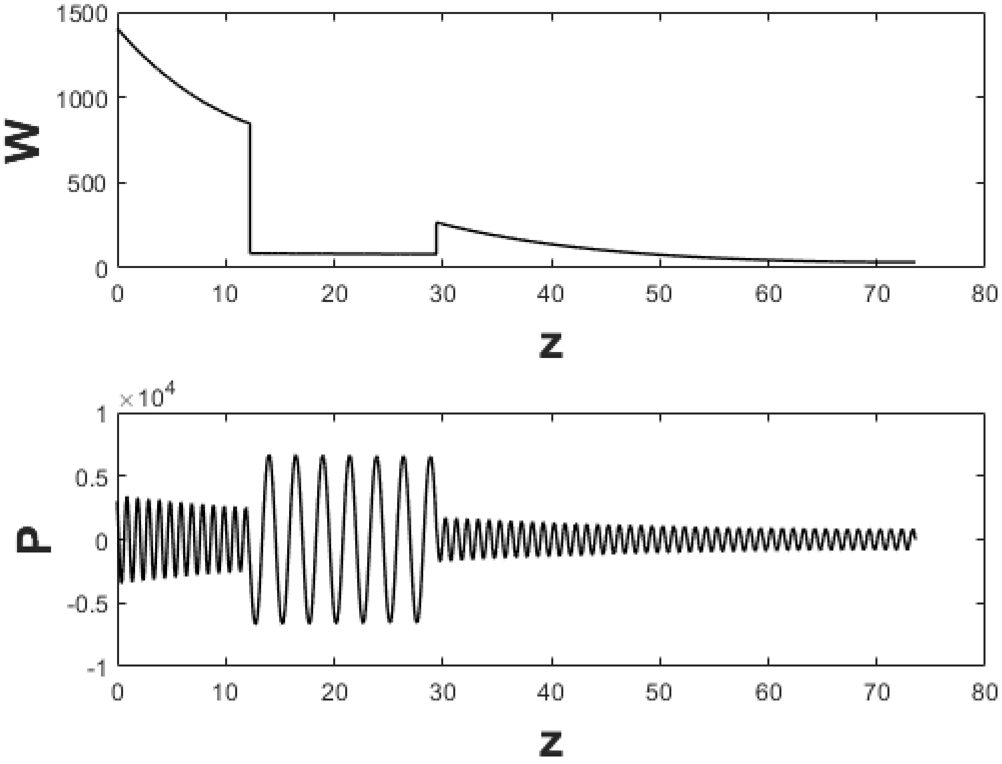

Figure 22: Dissipation rate and pressure in the tissue-bone-tissue domain at f= f_r with damping coefficients $\gamma_1 = 0.0014$ *and* $\gamma_2 = 0.0028$*.*

The dissipation rate is largest next to the transducer, from where it decays exponentially, the rates are low in the bone and second tissue regions.

The temperature is scaled with the ambient temperature, $\theta = \frac{T - T_{am}}{T_{am}}$ the first tissue region is described by the following equation. The radial variable has also been scaled with f_r/c_1.

$$\frac{\partial\theta_1}{\partial\tau} = \frac{\kappa_1 f_r}{c_1^2}\left[\frac{\partial^2\theta_1}{\partial z^2} + \frac{1}{r}\frac{\partial}{\partial r}\left(r\frac{\partial\theta_1}{\partial r}\right)\right] + \frac{W_1}{\rho_1 C_{p1} T_{am} f_r} \qquad 2.7.19$$

$$= A_1\,\Delta\theta_1 + B_1 A_1 W_1$$

The domain that is considered for the temperature distribution consists of a cylinder with radius R_c (the scaled radius of the transducer), and a cylindrical annulus surrounding it where into thermal energy conducts. The US dissipation rate is zero for $r > R_c$. From Figure 22 one infers that $W_i = W_{i0}e^{-a_i z}, i = 1,2,3$. In Table 4 we list some of the dimensionless parameters including the dissipation rates from Figure 22.

Region	κ_i	A_i	B_i	$W_{i0,}$	a_i
Tissue, *i=1*	2.2 E-07	3.0 E-07	9.9 E-10	13,574	0.0178
Bone, *i=2*	2.4 E-07	3.3 E-07	1.2 E-09	3,436	0.0303
Tissue, *i=3*	2.2 E-07	3.0 E-07	9.9 E-10	960	0.0361

Table 4: Dimensionless parameter values.

2.7.4 THERMAL GENERATION

The maximum temperature is at the center, which lies along $z \geq 0$, and $r = 0$. Consider the steady state problem, and as a first approximation we have lumped the radial conduction as follows;

$$\frac{d^2\theta_{1s}}{dz^2} - C_1\theta_{1s} + B_1 W_1 = 0, \qquad 0 \leq z \leq z_1$$

$$\frac{d^2\theta_{2s}}{dz^2} - C_2\theta_{2s} + B_2 W_2 = 0, \qquad z_1 \leq z \leq z_2$$

$$\frac{d^2\theta_{3s}}{dz^2} - C_3\theta_{3s} + B_3 W_3 = 0, \qquad z_2 \leq z \leq z_3$$

At $z = 0, \theta_{1s} = 0$,and at $z = z_3$, $\theta_{3s} = 0$. At $z = z_{1,2}$ we impose continuity of temperature and thermal flux,

$$\theta_{1s} = \theta_{2s}, z = z_1$$

$$\frac{d\theta_{1s}}{dz} = \frac{k_2}{k_1}\frac{d\theta_{2s}}{dz}, z = z_1$$

$$\theta_{2s} = \theta_{3s}, z = z_2$$

$$\frac{d\theta_{3s}}{dz} = \frac{k_2}{k_1}\frac{d\theta_{2s}}{dz}, z = z_2.$$

The solutions are

$$\theta_{1s} = h_{11} sinh\left(\sqrt{C_1}z\right) + \frac{B_1W_{10}}{a_1^2 - C_1} cosh\left(\sqrt{C_1}z\right) - \frac{B_1W_{10}}{a_1^2 - C_1} e^{-a_1z}$$

$$\theta_{2s} = h_{21} sinh\left(\sqrt{C_2}z\right) + h_{22} cosh\left(\sqrt{C_2}z\right) - \frac{B_2W_{20}}{a_2^2 - C_2} e^{-a_2z}$$

$$\theta_{3s} = h_{31} sinh\left(\sqrt{C_3}z\right) + h_{32} cosh\left(\sqrt{C_3}z\right) - \frac{B_1W_{30}}{a_3^2 - C_3} e^{-a_3z}$$

The coefficients h_{ij} are determined by applying the boundary conditions. In Figure 23 the temperature rise along the centerline is shown for $C_1 = C_2 = 0.01$ (top) and $C_1 = C_2 = 0$ (adiabatic case).

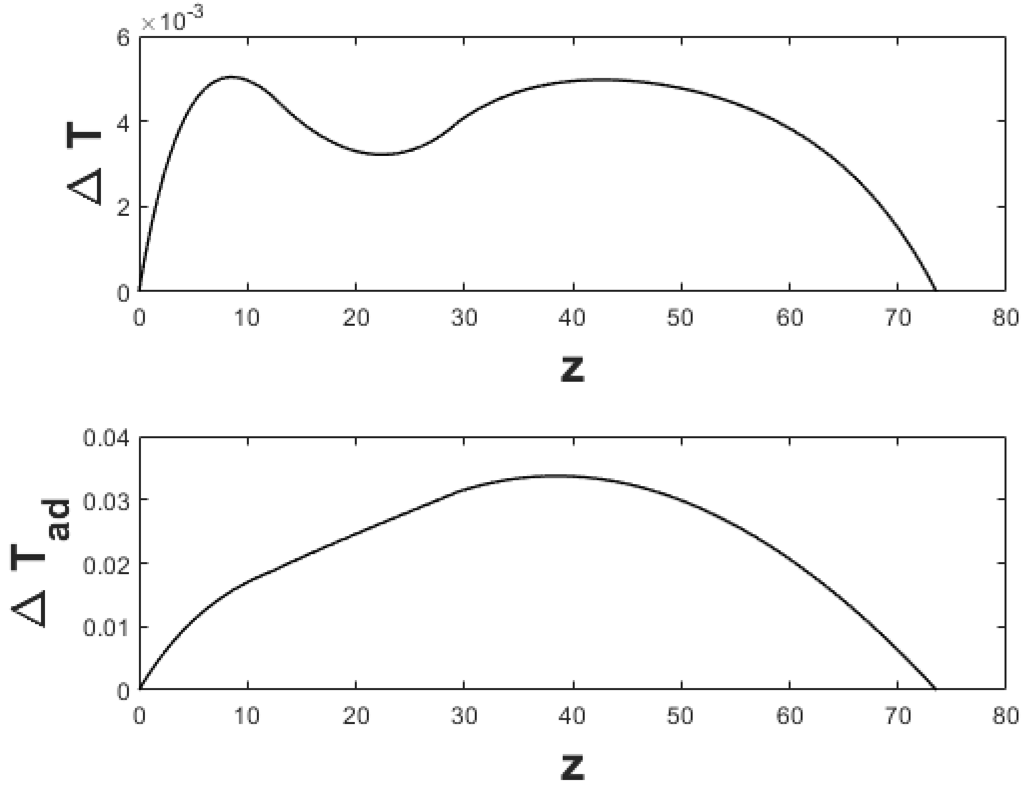

Figure 23: Temperature rise in the tissue-bone-tissue domain at f = f_r. The damping coefficients are $\gamma_1 = 0.0014$ and $\gamma_2 = 0.0028$. The top panel corresponds to $C_1 = C_2 = 0.01$ and the bottom panel to the adiabatic case ($C_{1,2}=0$).

The adiabatic temperature is an upper bound of the system. The adiabatic temperature rise is $0.035°\mathrm{C}$ and the maximum lies in the second tissue region. The non-adiabatic temperature rise $(C_{1,2} = 0.01)$ is approximately $0.005°\mathrm{C}$ and the maximum lies near the center of the first tissue region.

To summarize, a 1-D model has been developed that describes the US field in a system comprising of regions of tissue and bone. The model includes dissipation of the US field. The dissipation is a source term in the thermal energy balance and estimates of the temperature rise can be derived for adiabatic and non-adiabatic conditions. One utility of the model is to vary the input pressure until a target pressure is observed at the interface of the first tissue region and the bone (presumably the site of injury). The concomitant adiabatic temperature rise can be compared to temperature rises which are considered physiologically safe.

2.8 ANIMAL MODEL

The work done here was a collaborative effort with many different parties. Animal surgeries and procedures were designed by Dr. Anu Subramanian, and performed by Dr. Craig Kreikemeier-Bower. Histological analyses were done by University of Alabama-Birmingham Dr. Oraine Snaith, and Dr. Gene Siegal. Animal care and US application was done at University of Nebraska-Lincoln in Veterinary Sciences by Katelin Oborny and Jesse Baumann-Berg. The following results are a cumulative effort from all acknowledge parties and under publication preparation.

2.8.1 RABBIT CARTILAGE DEFECT MODEL

Bilateral defects were created on the knees of the rabbits using an IACUC approved protocol (1297) at the University of Nebraska-Lincoln (Lincoln, NE). To exclude gender-based differences in animal response to injury and repair, female New Zealand Rabbits (white), less than 8-months of age with a body weight of 4kg or less were purchased and acclimatized for about a week prior to surgery. Rabbits were anesthetized by the administration of Ketamine IM (35mg/kg) and xylazine (5mg/kg). Gas anesthesia was maintained using a nose-cone supplying 2-3% isoflurane. Rabbits were laid in supine position on the operating table and the knee was shaved and sterilized using betadine and 2% chlorhexidine. A medial parapatellar approach was used to enter the knee joint placed in flexion of 70 degrees and the patella was dislocated laterally to expose the articular surface of the distal femur. The defect was created on the medial femoral condyle as follows: A 5-mm diameter, full thickness cartilage defect was created using a biopsy punch (Miltex, York, PA) and a curette was used to remove the cartilage and the calcified layer thoroughly. Microfracture to a 3mm depth was performed using a surgical drill mounted with 0.9mm K-wires to create three 1.5mm diameter holes in each defect site, with each hole being 2 to 2.5mm apart on the subchondral bone (Figure 24A). Our rationale for going 3mm deep is based on a previous study that demonstrated that a 3mm deep hole significantly enhanced the volume of blood that could ooze from the bone marrow without penetrating the epiphyseal scar (Figure 24B) (Truong *et al*., 2014). Saline was continuously flushed to minimize the heat caused by drilling. The joint was then irrigated using saline and inner dermis was sutured using biodegradable suture while the outer dermis was closed using nylon sutures and/or metal staples which were removed after a week. Animals were monitored for complications by research and veterinary staff.

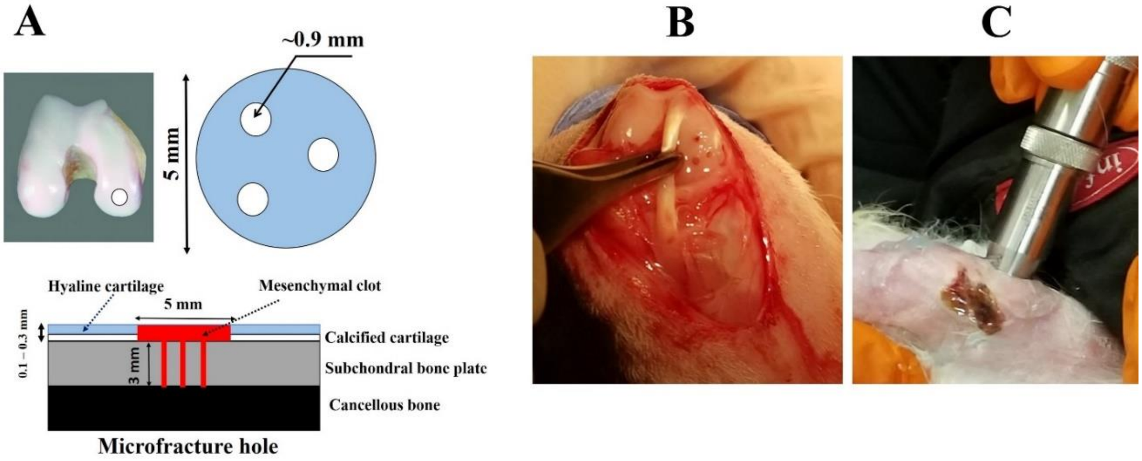

Figure 24: (A) A biopsy punch was used to circumscribe the defect area on the femoral medial condyle and a curette was used to debride the cartilage to create a full thickness cartilage defect. A surgical drill outfitted with 0.9mm K-wire was used to create 2.5 to 3 mm deep holes into the subchondral bone to induce bleeding into the defect. (B) Representative image of the defect created. (C) cLIUS was applied via a handheld transducer.

2.8.2 ANIMAL HOUSING AND CARE

Following the surgery, all animals received pain medication (Buprenorphine SR) during the surgical procedure and meloxicam every 24 hours for at least two days. After two days, if the animals showed any of the signs of pain or distress, Buprenorphine SR or meloxicam was administered on an as needed basis. As an antibiotic, enrofloxacin was given prophylactically once daily, starting intra-operatively and then 3 days post-operative. Rabbits were all housed together on the floor and were allowed unrestricted activity post-operatively. All rabbits were analyzed in a long-term study for 8 weeks. A total of 12 animals were included in these studies.

2.8.3 US APPLICATION PROCEDURE

US was applied using a custom-made non-focused transducer (Olympus NDT Inc., MA) with a radiating area of 1.27cm^2, a center frequency that matches the in-vivo resonant frequency identified (~3.8MHz), and a duty cycle of 100% (Figure 24C). All transducers were characterized by the manufacturer prior to usage. A waveform generator (HP, 33120A) was used to generate LIUS at the frequency of 3.8 MHz. The transducer was positioned on the skin such that the transducer face was approximately in line with the defect area. Coupling gel was applied to the skin. In the absence of exhaustive clinical literature from which to make absolute estimations of treatment time, current literature justifies one minute of US energy per treatment head area covered (Watson, 2008). US was applied for eight minutes/day for five days/week beginning on postoperative day 3. The sites were periodically shaved to ensure contact between the transducer, coupling gel, and skin, and the rabbits were held in a baby carrier.

At 8-weeks following defect creation, rabbits were anesthetized and euthanized as per the approved IACUC protocol. Following euthanasia, both stifle joints were harvested to allow visual inspection, X-ray analyses, and histopathologic testing of the repair tissue including the surrounding cartilage, the tibial cartilage in contact with the repair tissue and similar tissues from the contralateral limb.

2.8.4 *IN VIVO* EVALUATION OF CLIUS IN A FULL THICKNESS ARTICULAR CARTILAGE DEFECT RABBIT MODEL TREATED WITH MICROFRACTURE

Bi-lateral defects were created on the femoral medial condyle and left knee joint was subjected to the cLIUS treatment where the contralateral right joint served as the control (Figure 25). During defect preparation, immediate bleeding from the underlying subchondral bone plate was always observed after microfracture (Figure 24B). When the animals were euthanized at 4 or 8 weeks postoperatively, no joint effusion, macroscopic inflammation, peri-articular osteophytes, and adhesions were noticed in all treated joints. Three rabbits developed swollen joints post-surgically which were managed by draining the synovial fluid and administration of approved analgesics. Upon the completion of an 8-week study, all the rabbits appeared to have full range of motion in both knees and none of the rabbits developed apparent joint degradation or synovial inflammation.

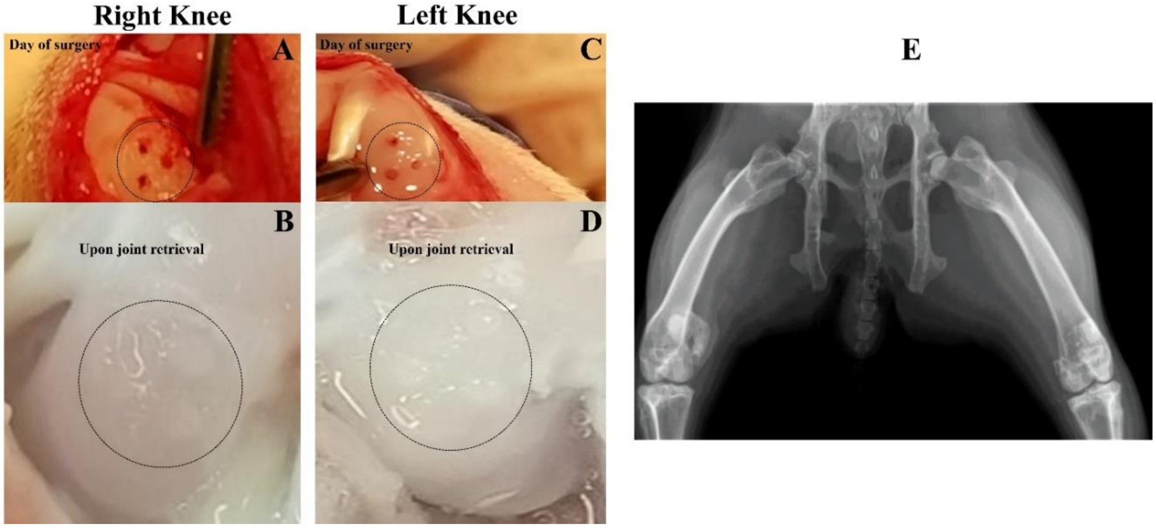

Figure 25: Rabbit-matched images of the defect areas are shown. Defect area is shown by a dotted circle. Panel-A shows the defect area created on the right femoral medial condyle on the day of surgery prior to closing of the joint fascia. Panel-B shows the defect area upon joint retrieval. Panel-C shows the defect area created on the left femoral medial condyle on the day of surgery prior to closing of the joint fascia. Panel-D shows the defect area upon joint retrieval. Panel-E shows the digital X-rays taken post euthanasia using a portable machine from Diagnostic Imaging Systems Inc (Model EPX-F2800).

Post euthanasia, joint capsule was opened, photographed, and evaluated macroscopically (Figure 25). In the non-stimulated control joints, defects were still obvious, with defect boundaries still visible exhibiting noticeable color and texture differences within the surrounding cartilage (Figure 25B). In contrast, the left knee joint that received cLIUS treatment showed uniform tissue fill in most defects with similar color and texture within the surrounding cartilage (Figure 25D). Macroscopic evaluation indicated integration of the engineered tissue with the native cartilage. Previous research showed that therapeutic doses of US (<500 mW/cm2) did not have an adverse effect on bone growth or led to degeneration of the cartilaginous cells in the growth plate (Lyon *et al.*, 2003). Anteroposterior (AP) and lateral radiographs (LP) of each knee joint were obtained after euthanasia and analyzed. Therapeutic doses of US (<500 mW/cm2) did not have an adverse effect on bone growth or cause degeneration of the cartilaginous cells in the growth plate. As anticipated, no adverse impact on the bone or changes within the joint space were noted under cLIUS (< 20 mW/cm2) employed in this study (Figure 26Figure 25).

Representative rabbit matched staining for hematoxylin and Eosin (H&E), Safranin-O, and IHC for collagen II (COL-II) are shown in Figure 26.

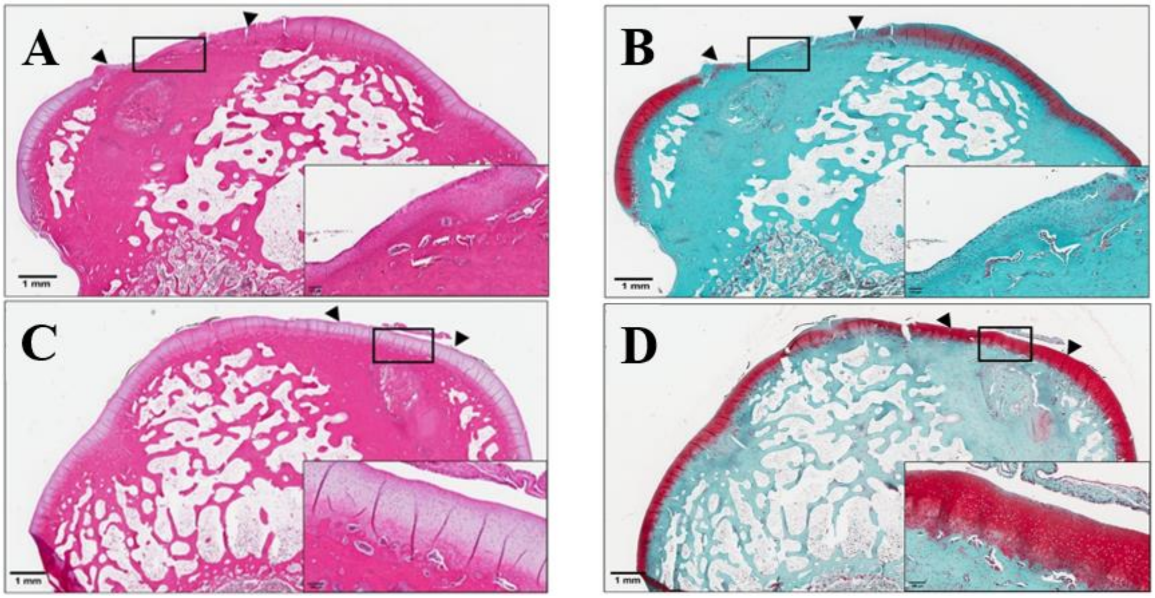

Figure 26: ***Histological evaluation of rabbit knee joint sections at 8 weeks****. Upon joint retrieval, rabbit joints were fixed in 10% formalin and processed for histological analyses using standard procedures. Left knee joints (C-D) were treated with cLIUS and the right knee joints (A-B) served as the contralateral non-stimulated control. 4 to 6 µm sections were stained and presented. Images at 2x and 20x magnifications are included and scale bars are shown in the images. Panel-A and C shows the HE stained section of a representative right and left rabbit joint, respectively. Panel-B and D shows the Safranin-O stained section of a representative right and left rabbit joint, respectively.*

Qualitative assessment of the H&E-stained histological sections of the non-stimulated right knee joints revealed incomplete filling of defects, loss of cellularity, and increase in subchondral bone density as a result of the reparative process and, in some cases, an irregular cartilage surface was noted (Figure 26A). Little to no staining for glycosaminoglycans (GAGs, Safranin-O) was observed in the defect area of the right knee joints (Figure 26B). In some sections, a loss of Safranin-O staining in the superficial layer of the surrounding native cartilage was noted indicating a loss of the extra cellular matrix components. Defects in the left knee joints treated with cLIUS showed a complete fill level to the surrounding native cartilage and a positive staining for GAGs matched the surrounding undamaged cartilage (Figure 26C and Figure 26D). Additionally, a rounded chondrocyte-like morphology, columnar organization and some cell clustering was observed.

2.9 CONCLUSION

All the information provided on the importance of transducer selection highlights theoretical modeling significance in cartilage regeneration. From the placement of the transducer to the input voltage, optimal selections can result in tissue repair or minimal effects due to a variety of variables. In some cases a patient could even see disadvantageous effects such as tissue damage due to unstable intensity. Avoiding this could be easily done through theoretical modeling on a patient-by-patient case. A summary of the main findings from this chapter are:

- There exists a linear relationship between input voltage and output pressure of a transducer.
- Comparing pLIUS and cLIUS shows that pLIUS always results in lower pressures, and thermal generation of cLIUS is not significant enough to rise concern for tissue health.
- Transducer placement is key in optimal pressure seen at the surface of the bone. When the transducer is in line with the joint space US penetrates deeply,

whereas when the transducer is in line with the defect site US minimally penetrates but a larger pressure is seen due to reflection of the US signal.

- A 1D model shows similar results to that of the 3D model and is significantly less computationally expensive. This would be the optimal model for patient-specific treatments in clinical settings.
- Performing a rabbit study using 3.8MHz cLIUS as a cartilage defect reparative therapy resulted in effective cartilage repair without exogenous addition of growth factors.

CHAPTER 3 – PERICELLULAR MATRIX MODEL

3.1 INTRODUCTION

Tissue regeneration can occur after damage due to the natural occurrence of stem cells throughout the human body (Facchin *et al*., 2018). An exception to this remarkable feature is articular cartilage, due to its avascular nature (Fox *et al*., 2009). The building blocks of cartilage, chondrocytes, are embedded in a mesh prohibiting the cells to move to the injured site (Newman, 1998). This essential connective tissue has a low friction coefficient and thus is an essential tissue which is located between joints that supports and distributes forces during everyday motion (Wilusz *et al*., 2014, Han *et al*., 2012).

Everyday activities over time as well as injury and obesity can damage this essential tissue causing a negative response in the chondrocyte and surrounding area (Guilak *et al*., 2004). Damaged articular cartilage leads to degradation and subchondral bone remodeling which translates to pain and dysfunction in the joint (Chen *et al*., 2013). These defects lead to the disease known as osteoarthritis, affecting millions of people per year (Arden, Nevitt, 2006; London *et al*., 2011). The necessity of cartilage tissue for health of joints merits research on methods to replace or renew it. Current methods of regeneration are vast and include: microfracturing (Mithoefer *et al*., 2009), grafting (Rubak *et al*., 1982), synthetic scaffold resurfacing (Sams, Nixon, 1995), autologous chondrocyte implantation (Richardson *et al*., 1999), and stem cell implantation (Mardones, Larrain, 2016; Freitag *et al*., 2016). These methods are expensive, invasive, and have conflicting efficacy (Huey *et al*., 2012; Kon *et al*., 2012) often requiring a combination of therapies to be used (Pestka *et al*., 2011). Result from these methods are unsatisfactory requiring an alternative solution. A worthy candidate for non-invasive technique for cartilage regeneration comes from a method that has already been proven to work for bone fracture treatment: low-intensity ultrasound.

A chondron consists of the pericellular matrix (PCM) surrounding the chondrocyte(s) (Benninghoff, 1925). The PCM surrounding the chondrocyte consists of an organized structure of types II, VI, and IX collagen as well as proteoglycans such as aggrecan, decorin, fibronectin, and hyaluronan (Poole *et al*., 1988). These molecules play a role in regulating biological functions protecting the chondrocyte from apoptosis (Wilusz *et al*., 2014; Mow *et al*., 1999; Haider *et al*., 2006). The structure of the PCM acts as a buffer between the chondrocyte and the extracellular matrix (ECM) to filter out mechanical forces as well as molecules entering or exiting the chondrocyte (Zhang, 2015; Zelenski *et al*. 2015), thus regulating cell activity (Wilusz *et al*., 2014; Guilak *et al*., 2006). Within the PCM it has been shown that chondrocytes occupy a low volume of cartilage tissue (Poole *et al*., 1997), layered with varying cell morphology and different nutrient requirements. Deformation experiments have shown the chondrocyte to change morphology under pressure, but to return to normal when unapplied (Wang *et al*., 2010). The PCM acts in a protective role thereby reducing stress on the chondrocyte. Parameters from Haider *et al* based on chondron osmotic loading experiments were used here (Haider *et al.*, 2006). In past research individual chondrocytes have been modeled in an acoustic field exhibiting multiplicity (Miller *et al.*, 2017). This study expands the nonlinear model from the chondrocyte to the chondron by including the surrounding PCM as a dampening factor. In this study we present a model of the interactions of a force on the PCM in the classical wave equation with a viscoelastic model of two phases.

3.2 INTRODUCING THE MATHEMATICAL MODEL FOR THE PCM

Inclusion of the PCM adds another layer that must be penetrated by ultra-sound (US) waves before they impact on the chondrocytes themselves. A chondron, of radius R_C, is surrounded by a PCM layer of radius R_P.

In the following section we first analyze the PCM. The PCM is a biphasic material, consisting of a solid phase and a liquid phase. The momentum balances for the solid and liquid phases are:

$$(\lambda+2\mu)\frac{\partial}{\partial r}\left(\frac{1}{r^2}\frac{\partial}{\partial r}(r^2u)\right)-\phi\frac{\partial P}{\partial r}+K\left(v-\frac{\partial u}{\partial t}\right)=\rho_s\frac{\partial^2 u}{\partial t^2} \qquad 3.2.1$$

and

$$-(1-\phi)\frac{\partial P}{\partial r}-K\left(v-\frac{\partial u}{\partial t}\right)=\rho_f\frac{\partial v}{\partial t} \qquad 3.2.2$$

where r is radius, ϕ is the solid volume fraction, P is pressure, u is the solid displacement, v is the fluid velocity, K is a diffusive drag coefficient, and ρ_s and ρ_f are the solid and fluid densities. The term $(\lambda+2\mu)$ is called the aggregate modulus where both λ and μ are dependent on the Young's modulus E and Poisson ratio υ such that $\mu=\frac{E}{2(1+\upsilon)}$ and $\lambda=\frac{E\upsilon}{(1+\upsilon)(1-2\upsilon)}$. Note that we neglect the nonlinear convection term in eq. 3.2.2 (i.e. $\rho v\frac{\partial v}{\partial r}$) as is the practice in the derivation of linear acoustic wave propagation. First, we assume the densities of the solid and fluid phases to be close. The continuity equation for the PCM is;

$$\frac{1}{r^2}\frac{\partial}{\partial r}(r^2[(1-\phi)v+\phi\dot{u}])=-A\frac{\partial P}{\partial t} \qquad 3.2.3$$

3.2.1 DIMENSIONLESS MODEL FOR THE PCM

The liquid velocity and solid displacement are scaled with the sound velocity of the liquid phase and the chondrocyte radius as follows:

$$W = v/c$$

$$s = u/R_C$$

The scaled pressure is given by

$$\pi = P/\left(\rho_f c^2\right)$$

The radial variable $\boldsymbol{r}$ is scaled with R_C and time t is scaled with R_C/c.

The balancing equations in dimensionless form are;

$$\frac{\partial^2 s}{\partial \rho^2} + \frac{2}{\rho}\frac{\partial s}{\partial \rho} - \frac{2s}{\rho^2} - \phi\alpha_1 \frac{\partial \pi}{\partial \rho} + \alpha_2 \left[W - \frac{\partial s}{\partial \tau}\right] = \alpha_3 \frac{\partial^2 s}{\partial \tau^2} \qquad 3.2.4$$

$$-(1-\phi)\frac{\partial \pi}{\partial \rho} - \beta_1 \left[W - \frac{\partial s}{\partial \tau}\right] = \frac{\partial W}{\partial \tau} \qquad 3.2.5$$

$$\frac{1}{\rho^2}\frac{\partial}{\partial \rho}\left(\rho^2 \left[(1-\phi)W + \phi \frac{\partial s}{\partial \tau}\right]\right) = -A\frac{\partial \pi}{\partial \tau} \qquad 3.2.6$$

The dimensionless parameters are:

$$\alpha_1 = \frac{\rho_f c^2}{(\lambda + 2\mu)};\ \alpha_2 = \frac{KcR_C}{(\lambda + 2\mu)};\ \alpha_3 = \frac{\rho_s c^2}{(\lambda + 2\mu)};\ \beta_1 = \frac{KR_C}{\rho_f c}$$

Note: The parameter A in eq. 3.2.6 is a dimensionless constant.

3.2.2 CASE 1: INCOMPRESSIBLE FLOW

Let us assume incompressibility (i.e. $\frac{\partial \pi}{\partial \tau} = 0$ in eq. 3.2.6). After integrating the continuity equation, we find the relation between $\frac{\partial s}{\partial \tau}$ and W depends on the function $B(\tau)$:

$$W = \frac{-\phi}{(1-\phi)}\frac{\partial s}{\partial \tau} + \frac{1}{(1-\phi)}\frac{B(\tau)}{\rho^2} \qquad 3.2.7$$

Next we substitute for $\frac{\partial \pi}{\partial \rho}$ from eq. 3.2.5 into eq. 3.2.4 and replace W using eq. 3.2.7. Since the system is externally forced the forcing will determine the temporal behavior.

$$\frac{\partial^2 s}{\partial \rho^2} + \frac{2}{\rho}\frac{\partial s}{\partial \rho} - \frac{2s}{\rho^2} + \kappa_1 s = \kappa_2 \frac{B(\tau)}{\rho^2} \qquad 3.2.8$$

The new constants are

$$\kappa_1 = \left[\left(\frac{\phi}{1-\phi}\right)^2 \alpha_1 + \alpha_3\right]\omega^2 - \left(\frac{\phi\alpha_1\beta_1}{1-\phi} + \alpha_2\right)\left(\frac{i\omega}{1-\phi}\right)$$

$$\kappa_2 = -\left(\frac{\phi\alpha_1\beta_1}{1-\phi} + \alpha_2\right)\left(\frac{1}{1-\phi}\right) - i\frac{\phi\alpha_1\beta_1\omega}{(1-\phi)^2}$$

The homogeneous solutions are

$$s_h = A\left(\frac{sin(a\rho)}{\rho^2} - a\frac{cos(a\rho)}{\rho}\right) + B\left(\frac{cos(a\rho)}{\rho^2} + a\frac{sin(a\rho)}{\rho}\right) \qquad 3.2.9$$

The Wronskian is $w = -\frac{a^3}{\rho^2}$, and it is not zero on the interval $\rho \in \left[1, R_p/R_C\right]$. The particular solution is

$$s_p = -\frac{\kappa_2 B_0}{a^3}\frac{sin(a\rho)}{\rho}\left(\frac{sin(a\rho)}{\rho^2} - a\frac{cos(a\rho)}{\rho}\right) + \frac{\kappa_2 B_0}{a^3}\frac{cos(a\rho)}{\rho}\left(\frac{cos(a\rho)}{\rho^2} + a\frac{sin(a\rho)}{\rho}\right) \tag{3.2.10}$$

The general solution is the sum of the homogeneous and the particular solutions. The boundary conditions are applied to the general solution. Before we include the PCM layer in the nonlinear cell model, let us analyze it by itself. Therefore, we impose the following boundary conditions at the inner and outer PCM surfaces;

$$s = s_0 e^{i\omega\tau}, \rho = R_P/R_C$$

$$s = 0, \rho = 1.$$

We consider external forcing at the outer surface. By setting the displacement equal to zero at the inner surface, we calculate the maximum normal stress, proportional to $\frac{\partial s}{\partial \rho}$, that the PCM will exert on the chondrocyte. In Figures Figure 27 - Figure 29 we compare the normal stress at the outer PCM surface (blue) with the stress at the inner surface (red) for three different values of the damping coefficient K. The plots in Figure 27 represent a case of moderate damping, $K = 10^{10} Pa.m^2/s$, and the plots in Figure 28 and Figure 29 are calculated for $K = 10^{11} Pa.m^2/s$ and $K = 10^{12} Pa.m^2/s$ respectively.

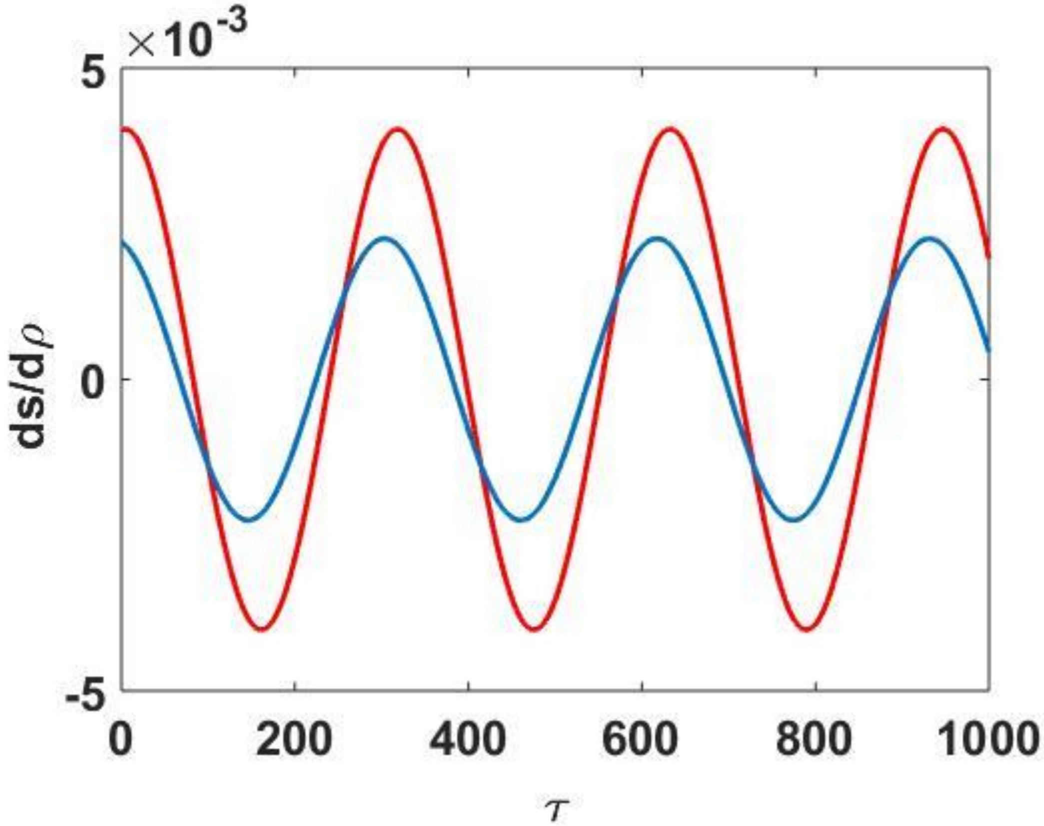

Figure 27: Plots of the time dependence of ∂s/∂ρ at the outer PCM surface (blue) and inner PCM surface (red). K is 10^{10} Pa m^2/s.

The first interesting observation is that the stress is higher at the inner surface than at the outer surface – this is not that surprising since we are dealing with a spherical coordinate system. Also note that a small phase shift exists between the two waves.

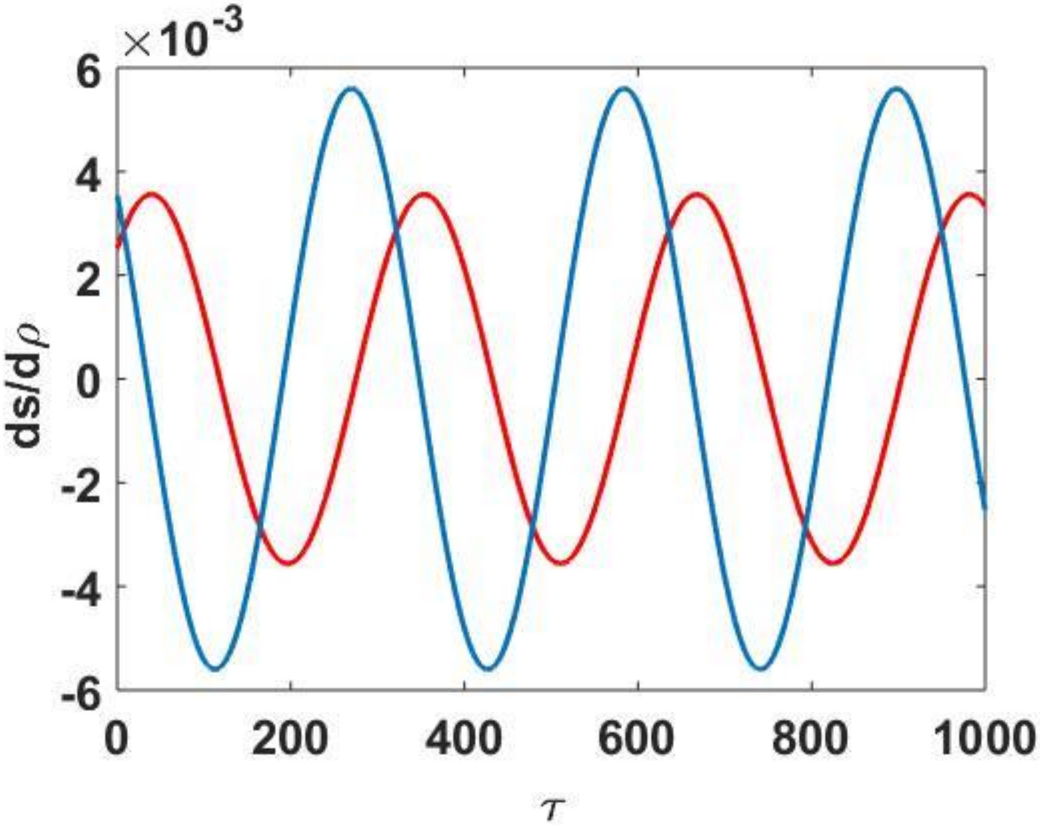

Figure 28: Plots of the time dependence of $\frac{\partial s}{\partial \rho}$ *at the outer PCM surface (blue) and inner PCM surface (red) for a damping coefficient of* 10^{11} *Pa* m^2*/s.*

The phase shift has increased from the plots in Figure 27 and the damping effect more than cancels the focusing effect of the spherical coordinate system. The ratio of the input normal stress to output normal stress (blue: red amplitudes) is less than one. The damping mechanism converts the input mechanical energy into thermal energy and less mechanical energy is available at the inner PCM surface.

In Figure 29 we plot the results for $K = 10^{12} Pa.m^2/s$. The system becomes overdamped, as a matter of fact the system is dominated by the parabolic terms and the mechanical forcing decays monotonically. This represent a case where all the input mechanical energy is converted into thermal energy. Depending on the energy input, this situation could lead to significant temperature rises. The results in Figure 29 are representative of all damping coefficients higher than $10^{12} Pa.m^2/s$.

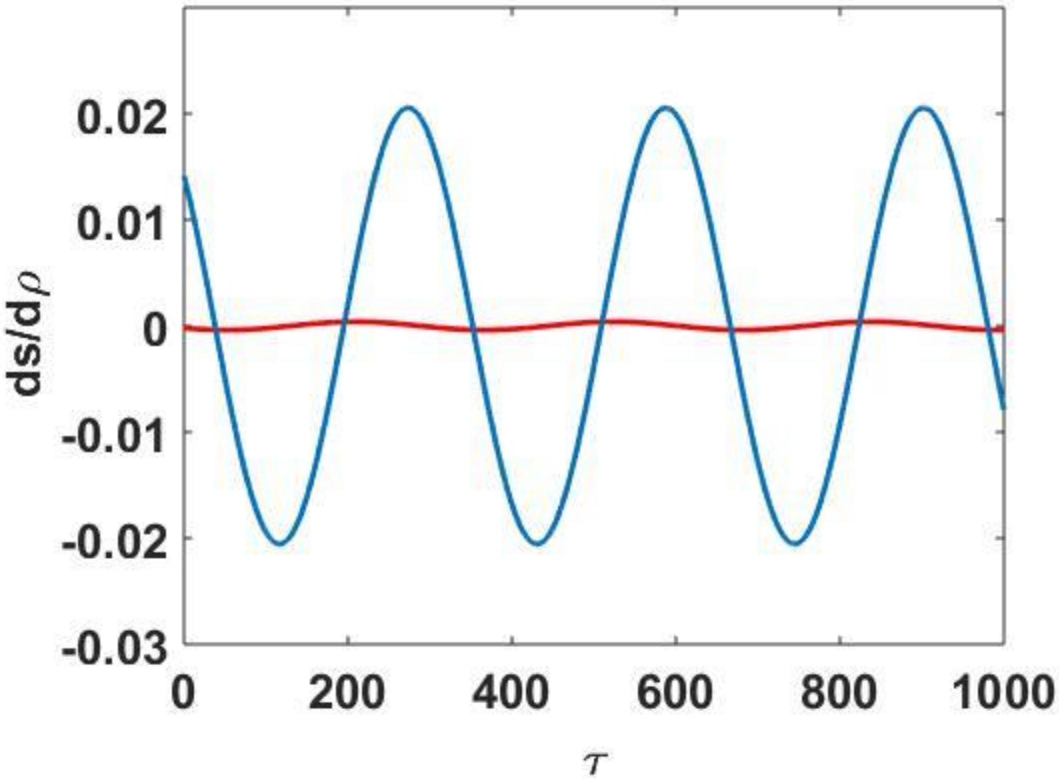

Figure 29: Plots of the time dependence of $\frac{\partial s}{\partial \rho}$ *at the outer PCM surface (blue) and inner PCM surface (red) for a damping coefficient of* 10^{12} *Pa* m^2*/s.*

3.2.3 CASE 2: A > 0

The collagen fibers which constitute the solid phase of the PCM are submicron particles which will exhibit very little inertia, particularly at the US frequencies we use in our studies. Therefore, we do not expect much slip to occur at the interface of the two phases. To put it in more quantitative terms, let $W - \frac{\partial s}{\partial \tau} = gW$, where $g \ll 1, g > 0$.

Thus, we substitute for $\frac{\partial s}{\partial \tau}$ in eq. 3.2.6. The scaling we have used leads to $A = 1.$ Next we eliminate the pressure between equations 3.2.5 and 3.2.6 and obtain the classical wave equation with a damping term.

$$(1-\phi g)\left[\frac{\partial^2 W}{\partial \rho^2}+\frac{2}{\rho}\frac{\partial W}{\partial \rho}-\frac{2W}{\rho^2}\right]-\beta_1 g\frac{\partial W}{\partial \tau}=\frac{\partial^2 W}{\partial \tau^2} \qquad 3.2.11$$

The solution consists of spherical Bessel functions of the first and second kind

$$W=\left[B_1\left(\frac{sin(a\rho)}{\rho^2}-a\frac{cos(a\rho)}{\rho}\right)+B_2\left(\frac{cos(a\rho)}{\rho^2}+a\frac{sin(a\rho)}{\rho}\right)\right]e^{i\omega\tau} \qquad 3.2.12$$

The wavenumber is complex;

$$a^2=(\omega^2-i\beta_1 g\omega)/(1-\phi g).$$

The constants $B_{1,2}$ are defined by the external forcing. Suppose the pressure on the outer surface of the PCM layer is $\pi_0 e^{i\omega\tau}$, then we can examine the solution with varying damping coefficients shown by Figures Figure 30 and Figure 31.

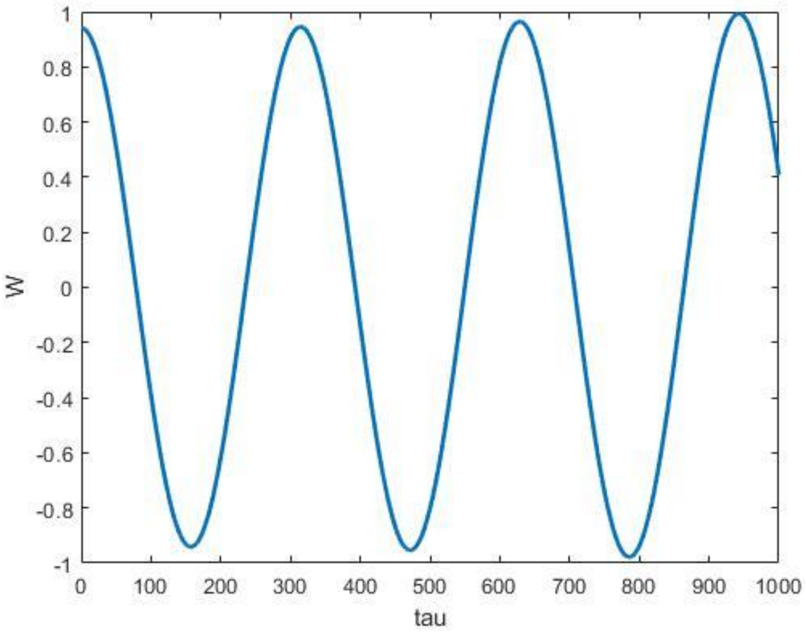

Figure 30: Plot of the solution to the wave equation with varying damping coefficient 10^{10} *Pa* m^2/s.

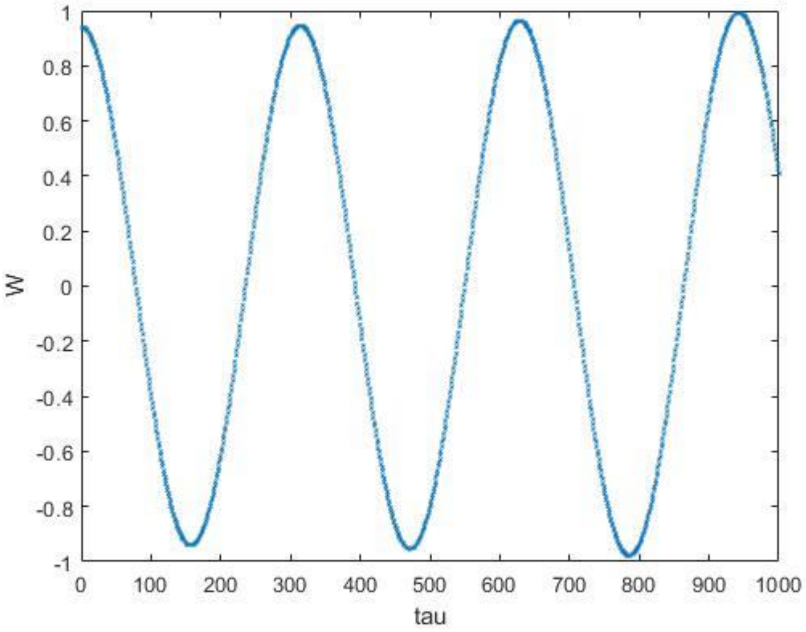

Figure 31: Plot of the solution to the wave equation with varying damping coefficient 10^{11} *Pa* m^2/s.

3.3 DISCUSSION

Presented here is a model showing the effects of outside pressure application to the PCM and the signal translated to the chondrocyte. The results clearly show the importance of the magnitude of damping coefficient used in the wave equation. This model was prompted from the radial biphasic model from Haider where the damping coefficients were much higher in magnitude causing an overdamped system and little transmission of signal to the chondrocyte (Haider, 2004). The mechanical signal seen through actin and collagen fibers in the PCM surrounding the cell activates autoregulation in cartilage, and when stem cells are present stimulate chondrogenic differentiation (Zhao *et al*., 2020). A high damping coefficient correlates with an overdamped system which in turn transforms the mechanical energy into thermal energy. Too much heat in the system causes apoptosis.

CHAPTER 4 – PATHWAYS IN CHONDROGENESIS

4.1 INTRODUCTION

Frictionless movement in joints is due to the cushion articular cartilage provides on the end of long bones. Cartilage tissue is essential to everyday movement ranges in thickness and mechanical properties (Guilak *et al*., 2005). Breakdown and degradation of this tissue can be attributed to age and joint stress via trauma and/or obesity, resulting in osteoarthritis, a chronic joint condition (Setton *et al*., 1999). This degenerative disease affects millions of people per year and is becoming more commonplace with the rise of aging and obese populations. The lack of this protective tissue causes pain and irritation in surrounding tissues and inevitably leads to bone loss (Han *et al*., 2019). Chondrocytes are the cells that maintain and makeup cartilage tissue which rely on the dense extracellular matrix for signals and nutrients since the tissue is avascular (Hunziker *et al*., 2002).

The nature of cartilage tissue lacks the capability for self-renewal or regeneration, requiring outside interventions (Grande *et al*., 1989). Various clinical approaches for tissue repair have been explored, though typically a full joint replacement is the answer. With the ever-increasing population requiring intervention for cartilage tissue loss, research has heightened to find more effective reparative techniques (Boushell *et al*., 2017). One such method is a minimally invasive option utilizing a microfracture procedure with continuous low intensity ultrasound (Qi *et al*., 2011). Ultrasound treatment has proven to heal bone fractures, promote pain relief, and reduction of muscle spasms (Pilla *et al*., 1990, Morishita *et al*., 2014). Microfracture allows a blood source needed for the avascular tissue to heal. The small channels, or stents, created during microfracture allow for bone MSCs to migrate to the injured bone surface where cartilage tissue is needed. Synovial fluid surrounds the joint and provides nutrients for cartilage and thus MSCs for chondrocyte formation (O'Hara *et al*., 1990).

The process of MSC differentiation to a chondrocyte (chondrogenesis) which occurs in stages: recruitment and migration, proliferation, and condensation (Goldring *et al.*, 2006). Chondrogenesis is a complex and multistep process that begins by migrating and condensing MSCs (Goldring *et al*., 2005). Different markers in varying concentration correspond to the stages of chondrogenesis which is taken into consideration in the following modeling sections. This study focuses on the condensation of MSCs – an important indicator of differentiation to chondrocytes. The condensation stage peaks at day 3 (Bang *et al.*, 2000) which could be expedited by utilizing ultrasound. In vitro experiments show cellular condensation leading to chondrogenesis in monolayer cultures (Shukunami et al., 2009). Three dimensional alginate cultures have also demonstrated condensation of rabbit bone marrow MSCs and subsequent induction of cartilage matrix synthesis under cLIUS at 1MHz (Lee et al., 2007). Furthermore, cell condensation was demonstrated in vitro providing significant evidence toward chondrogenic development (Kim et al., 2016; Sing, Schwarzbauer 2014). More evidence of condensation during chondrogenesis through pLIUS has been shown in vitro and in vivo experiments (Uenaka *et al*., 2009).

Many studies have suggested that LIPUS treatment is conducive for regenerating articular cartilage, despite the fact that the underlying mechanisms tying intracellular pathways to improved, healthier outcomes remain poorly understood (Chen *et al*., 2017).

There exists ample evidence (Louw *et al.*, 2013; Sahu *et al.*, 2020) that US promotes the expression of SOX9 in chondrocytes, which lead to higher levels of ECM secretion. Putative intracellular pathways responsible for the upregulation of SOX9, initiated by US stimulation have been proposed by Louw *et al.* and Miller *et al.* (Louw *et al.*, 2013; Miller *et al*., 2017). They also conjectured on the mechano-chemical mechanisms. Briefly, two mechanisms have been proposed which work in parallel. First, US causes oscillating widening/contracting of the calcium ports in the cell membrane, and the increase in calcium in the cell triggers the mitogen-activated protein kinase (MAPK) pathway (Raizman *et al*., 2010). The second mechanism, admittedly speculative, is that US also causes a dilatational expansion/contraction of the cell nucleus and this action could lead to faster nuclear translocation. Important evidence that supports this mechanism was reported by Whitney *et al*. (Whitney *et al*., 2012). This work linked the nuclear transport and chromatin binding to mechanical energy density of the nucleus using a combination of modeling and *in vitro* experiments.

Although chondrocytes are responsible for the formation of new cartilage and the maintenance of ECM, the broader physiological picture must include the recruitment of mesenchymal stem cells (MSCs) from the bone marrow to the injured site where they differentiate into chondrocytes to supplement the existing cells and aid in the healing process. Chondrogenesis is therefore an important part of the repair process. A very interesting finding, reported by Lee *et al.*, is that US also promotes chondrogenesis (Lee *et al.*, 2006). To put this finding in perspective, *in vitro* studies on chondrogenesis always require that MSCs be treated with exogeneous transforming growth factor beta (TGF-β), a growth factor that is a necessary precursor to differentiate to chondrocytes. In the *in* *vivo* case, the exogeneous prompting is obviously absent, which means the MSCs produce them endogenously. Coming back to the result of Sahu *et al*., who compared *in vitro* chondrogenesis of MSCs exposed to US with non-US controls (Sahu *et al*., 2020). The MSCs which were exposed to US readily differentiated into chondrocytes but the controls did not. It is conjectured that the signaling pathway starts via mechanical stress that is mediated by integrins (Whitney *et al.*, 2012), from pressure signals in the surrounding matrix. The mathematical model here attempts to describe the condensation stage of chondrogenesis in MSCs by tying together the essential pathways and the subsequent changes in protein expression levels.

4.2 PATHWAYS INVOLVED IN CHONDROGENESIS

Extensive research of molecular regulation on MSC differentiation has shown that MAPKs, TGF-β, and Wnt signaling are essential for chondrogenesis (Guo, Wang, 2008) with the most widely studied pathway being the MAPK/ERK cascade due to the integrin receptors being thought of as primary regulators. The ability of integrin receptors to communicate with surrounding matrix elements is seen in mechanotransduction studies and confirms the necessity to describe the cascade as a whole (Zhao *et al.*, 2020). Of the many proposed pathways that exist in chondrogenesis (Li, Dong, 2016), three are highlighted to here to be essential in the condensation process: the focal adhesion kinase (FAK) pathway, TGF-β pathway, and the wingless-type protein (Wnt) pathway (Szychlinska *et al.*, 2017). The TGF-β pathway expresses the transcription factor SOX9, a master marker for mesenchymal cell commitment to chondrogenic lineage (Coricor, Serra, 2016). Chondrogenesis is a multifaceted process which also includes pathway crosstalk. This can be seen with the proposed interactions shown in Figure 32.

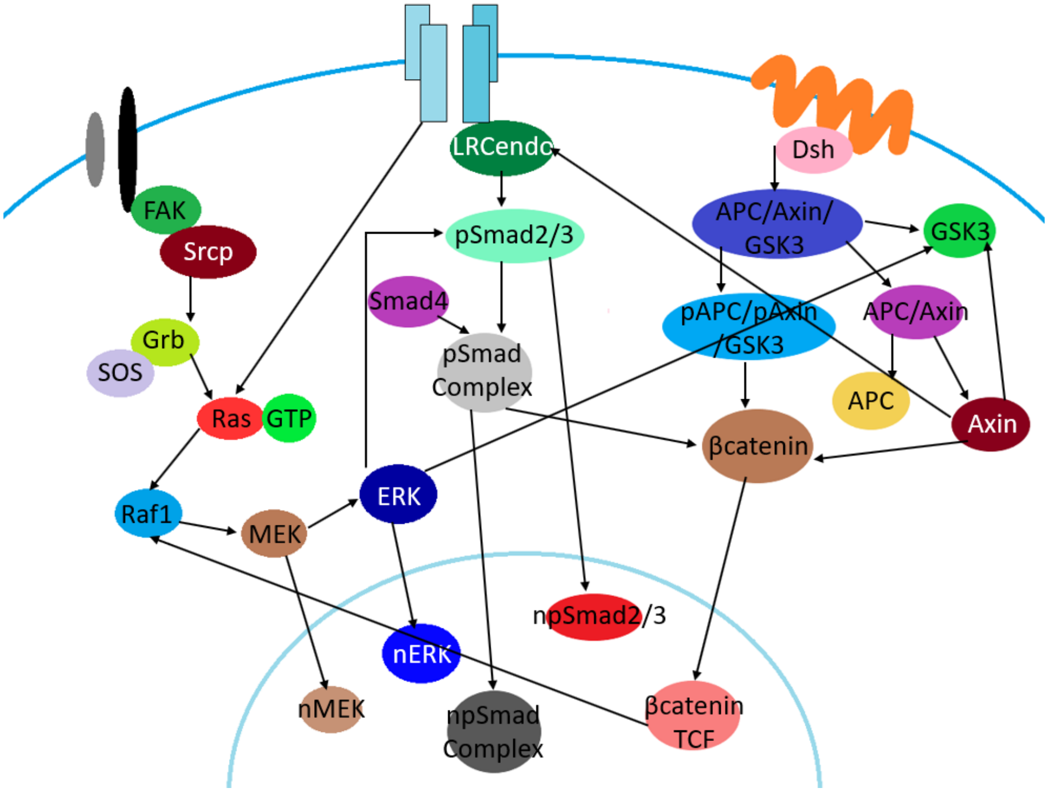

Figure 32: Simplified view of proposed mechanisms within the FAK, TGF-β, and Wnt pathways.

4.3 ON MODELING EFFECTS FROM ULTRASOUND

In an effort to understand the effects of ultrasound treatment researchers have relied on *in vitro* experiments (Korstjens *et al.*, 2008; Whitney *et al.*, 2012). This provides some understanding of just how ultrasound effects these chondrocytes such as inhibition of inflammatory responses (Sahu *et al.*, 2019). Chondrocytes are surrounded by a pericellular matrix (PCM) as well as an extracellular matrix (ECM) which dampen the mechanical signals to the chondrocyte. The deformation in the surrounding matrices gives rise to a response in the chondrocyte by stimulating pathway initiation and releasing factors from receptors (Zhao *et al.*, 2020). Integrin receptors are transmembrane proteins that mediate chemical and mechanical signals from outside and inside the cell via attachments to actin filaments (Ingber, 1991). This makes integrins a high interest study area due to the interest in their interactions with the ECM. The focus here is their ability to translate the mechanical signals from ultrasound to stimulate activation of the FAK pathway.

Though it is known that US effects the FAK pathway, reports of altering other pathways have been found (Huang *et al.*, 2018). For the TGF-β pathway it was found to initiate the expression of TGF-β without any exogenous additions (Lee *et al.*, 2006). More specifically the induction of condensation has been widely achieved by chemical and physical stimuli for chondrogenic differentiation with the TGF-β pathway (Pelaez *et al.*, 2012). These are taken into account in the following sections, which describe the mathematical interpretation of US effects on each pathway and include the responses from pathway crosstalk.

4.3.1 THE FAK PATHWAY

The most widely studied pathway in chondrogenesis is the focal adhesion kinase (FAK) pathway, which is the upstream regulator of the MAPK pathway. Multiple inhibition experiments show that integrin mediated interaction is key in condensation and chondrogenesis (Bang *et al.*, 2000; Zhang *et al.*, 2015). FAK and the cytoskeleton protein paxillin are essential for precartilage condensation of MSCs. Phosphorylation of FAK showed to be increased during condensation, and subsequently reduced as chondrogenesis progressed. Inhibiting treatments showed markedly suppressed condensation and cartilage nodule formation indicated phosphorylated FAK is required.

Condensation of MSCs with ultrasound begins with the focal adhesion kinase (FAK) pathway through mechanosensitive integrin receptors. FAK is an essential tyrosine protein for integrin signaling shown to be a key factor in a variety of pathways (Parkin *et al*., 2019). This model focuses on the activation of a complex bound to integrins in the cytoplasm which begins the cascade where phosphorylation of Ras, Raf, MEK1/2, and ERK1/2 leads to cell growth and proliferation (Zhou *et al.*, 2015). This pathway overall has been shown to be an important intracellular mediator of chondrocyte differentiation through the extracellular signal-related kinase (ERK) (Bobick, Kulyk, 2004).

A 2015 model by Zhou *et al.* examined pulsed low-intensity ultrasound (pLIUS) effects on fibroblast cells using Michaelis Menten kinetics (Zhou *et al*., 2015). This study showed integrin receptor activation with the Rho/ERK signaling pathway. This model was combined with nuclear shuttling modeling done by Fujioka *et al.* to create a complete picture of the pathway (Fujioka *et al*., 2006). Ultrasound starts the cascade on the FAK pathway by forcing the integrins on the cell wall apart using an equation relating work done on the environment, an initial reaction rate k_0, and the mean Gibbs free energy to create an opening between integrins (Dudko *et al*., 2006):

$$k = k_0 \left(1 - \frac{\nu w}{\Delta G}\right)^{\frac{1}{\nu} - 1} e^{\Delta G\left[1 - \left(\frac{\nu w}{\Delta G}\right)^{1/\nu}\right]}$$

Work on the system can be defined as a quasi-static process of cellular contraction (Dill *et al.* 2010):

$$w = -\int_{V_A}^{V_B} P dV$$

From previous modeling on the PCM we assume a symmetrical pressure of 10kPa. The change in volume under an external pressure is set to 2e-15μm^3 (Guo *et al*., 2017). Pathway kinetics are modeled using Michaelis-Menten as well as first or second order reactions. The FAK model by Zhou *et al.* used experiments to verify that ERK activation with ultrasound promotes cell proliferation (Zhou *et al.*, 2004). To fully describe this pathway, a model elucidating Ras-Raf signaling from Fujioka *et al.* has been incorporated (Fujioka *et al.*, 2005). They used fluorescent probes to determine rate constants for use in their mathematical model primarily using first and second order reactions. This showed a peak activation of RasGTP at five minutes and thereafter a steady decline.

4.3.2 THE TGF-β PATHWAY

Wide agreement has been reached on the requirement of TGF-β for all stages of chondrogenesis (Chen *et al.*, 2009). TGF-β acts as a multifunctional remodeling growth factor and modulator of gene expression (Huang, Chen, 2012). This pathway creates the master chondrogenic marker SOX9. The TGF-β pathway promotes cartilage matrix synthesis in various stages of chondrogenesis through the creation of TGF-β and the master chondrogenic marker SOX9. Although the gene expression from this pathway is essential, it alone is not enough to explain chondrogenesis due to the reduced TGF-β and type II receptor in older patients (Qureshi *et al.*, 2008). Exogenous TGF-β experiments with pLIUS shows chondrogenic differentiation of MSCs in alginate culture (Lee *et al.*, 2006), stimulated TGF-β production (Mukai *et al.*, 2005), and SOX9 level dependency on pathway crosstalk activation via dynamic compressive forces (Haudenschild *et al.*, 2010). The results lead to a hypothesis that pLIUS utilizes multiple pathways. Those findings translate to cLIUS as similar mechanical signals are sent to the chondrocyte through the surrounding matrices

Nuclear phosphorylated Smad2/3 increases levels of SOX9 which leads to the chondrogenic markers collagen 2 and aggrecan (Cleary *et al.*, 2013). These components have repeatedly been proven essential in chondrogenesis which are described here with TGF-β and receptor levels as they correlate directly to pathway activity (Liu *et al.*, 2018). Sustained TGF-β stimulation with medium-dosing has been well described by Zi *et al.* (Zi *et al.*, 2011). This pathway has been incorporated to the overall model, with initiating kinetics changed to be based on US stimulation in a fashion similar to that of the FAK pathway, and modified TGF-β kinetics using knowledge that phosphorylated Smad2/3 mediates transcription of intracellular TGF-β which secrets to the extracellular environment (Morshed *et al*., 2018). A report using bone cells with continuous low-intensity ultrasound (cLIUS) application at 3MHz showed an increase of more than 2-fold at minimum from initial concentration (Harle *et al.*, 2005). Since osteoblasts are closely related to chondrocytes, utilizing this information serves as a basis for the effect of US on chondrocytes (Findlay, Atkins, 2014).

4.3.3 THE WNT PATHWAY

The final pathway integrated here is the Wnt canonical pathway, otherwise called the β-catenin pathway. Conflicting evidence of the role of Wnt signaling in chondrogenesis has been reported (Ham *et al.*, 2015), but in recent years has been identified as playing a central role in cellular mechanotransductive responses (Bullock *et al.*, 2018). This could be due to the wide variety of ligands, receptors, and co-receptors that exist in the Wnt family and the complex nature of the pathway (Abuammah *et al.*, 2018). Through experimentation Wnts 3a, 4, 5a, 5b, 7a, 11, and 14 have been all been found to play a role in MSC condensation (Hens *et al.*, 2009) as well as all other stages of chondrogenesis (Gadjanski *et al*., 2012).

A quantitative model of the Wnt pathway was published by Lee *et al.* (Lee *et al.*, 2003) where the dishevelled receptor was activated which in turn releases GSK3B from the APC/Axin/GSK3B complex continuing on to a cyclical destruction of β-catenin/APC/Axin/GSK3B and the phosphorylated complex. This cycle includes β-catenin and its phosphorylated state interacting with Axin and APC. The pathway ends in nuclear β-catenin/TCF which serves as a transcription activator. The intracellular downstream signaling molecule in this pathway, β-catenin, plays a mediating role in the canonical pathway and is shown to be a transcriptional co-activator in the proliferation and differentiation of MSCs (Day *et al.*, 2005). Variation of β-catenin levels show changes in gene expression therefore requiring modeling to show optimal levels for chondrogenesis. In osteoblast cells mechanical loading and shear stress have been shown to activate canonical Wnt signaling (Olkku *et al.*, 2010). With the unique structure of the dishevelled receptor, the US activation of this pathway has to be adjusted. This was done by increasing the rate of activation of the dishevelled receptor (Betancourt *et al.*, 2012).

4.4 PATHWAY CROSSTALK

Findings have usually focused on the primary pathway, and no consideration has been given to the interaction with other signaling cascades. With our better understanding~~s~~ of how the primary pathway works, research on crosstalk between pathways has shown more complex interactions (Oshimori, Fuchs, 2012). Studies on pathway interactions also vary with reports of inhibition or enhancement. The majority of variability can be attributed to the cell type used in experiments. Expression of SOX9 and aggrecan were significantly down-regulated with ERK inhibiting experiments during dynamic compression confirming that ERK activation is key for chondrogenesis to occur (Pelaez *et al.*, 2012). Instead, cells are driven towards osteogenic lineage. ERK is a multifaceted protein and involved in various signaling pathways and it was also taken into account in this model.

4.4.1 FAK AND WNT

The original Wnt pathway developed by Lee was expanded to include ERK activation through crosstalk (Kim *et al.*, 2007). Their model uses a positive feedback loop with an unknown molecule X, and influenced by Raf kinase inhibitor protein (RKIP). The results show stimulation from an inactive to active state without any external receptor signaling from growth factors. Here the model has been adjusted to be activated through the ERK activation from the FAK pathway. Further confirmation of synergistic interaction between these pathways has been proven to exist in osteoblasts (Sun *et al.,* 2016). Experiments showed a direct correlation of FAK deficiency translating to downregulation of the canonical Wnt signaling.

4.4.2 FAK AND TGF-β

The precise role of ERK activation in research has been described in both positive (Xu *et al*., 2020) and negative (Li *et al*., 2010) roles regarding chondrogenesis. This system describes ERK activation as a positive regulator in chondrogenesis as activation of ERK results in increased TGF-β levels (Pelaez *et al*., 2012). Research done on cells of mesenchymal origin show synergistic ERK-Smad interactions (Hayashida *et al.*, 2003). Furthermore, experiments with chondrogenic specificity also show synergistic effects of TGF-β and integrin mediated signaling that enhance downstream signaling during condensation with cartilage nodule formation (Bang *et al.*, 2000). The tight coupling of these two pathways is has been well established experimentally (Furumatsu *et al.*, 2005). Hough *et al.* suggested a positive scheme in MSCs coupling these two pathways where instead of inhibitory effects, the interacting proteins enhance kinetics (Hough *et al.*, 2012). Here, the TGF-β receptor I interacts with RasGDP to shift to the GTP state. Another possible interaction between the pathways is phosphorylated ERK assisting in nuclear translocation of phosphorylated Smad2/3 (Javelaud, Mauviel, 2005).

4.4.3 WNT AND TGF-β

The TGF-β pathway promotes Wnt activity through decreasing Axin expression which increases Wnt ligand expression (Wu *et al*, 2016). A positive feedback loop has been identified by Seo *et al.*, showing that TGF-β induces Wnt production (specifically Wnt3a) (Seo *et al*., 2019), which increases TGF-β production, and so on in cardiac fibroblasts which has been confirmed in chondrocytes (Zhou *et al.*, 2009). Here, the proposed mechanism of TGF-β activation of the Wnt pathway is through the phosphorylated Smad2/3 Smad4 complex with cytoplasmic β-catenin increasing the nuclear translocation to β-catenin/TCF (Wu *et al.*, 2016). General activation of the Wnt pathway through exogenous additions of TGF-β has been shown in fibroblasts through accumulation of nuclear β-catenin, leading to the transcription coactivator β-catenin/TCF

(Akhmetshina *et al.*, 2012). The other part of the positive feedback loop involves Axin from the Wnt pathway activating Smad2/3 through the TGF-β receptor I (Furuhashi *et al.*, 2001). Overall, high levels of β-catenin are shown in mesenchymal condensation with increased SOX9 expression (Kirton *et al.*, 2007).

4.5 RESULTS AND DISCUSSION

The modeling done here focuses on three primary pathways to show protein levels directly associated with chondrogenic specific markers during condensation. The mathematical model was built utilizing powerful ODE solvers in Matlab. The three models from Zhou *et al.*, Zi *et al.*, and Kim *et al.* are combined here with crosstalk in pathways to build the full model. One of the key takeaways from inhibition experiments is the intricacy of underlying events during MSC differentiation. The plots here are in nanomolar concentrations, with time in seconds. Pulsed ultrasound (pLIUS) experiments showed a threefold increase of FAK phosphorylation at 3.5MHz (Jang *et al.*, 2014). Here, we see a similar response at 3.8MHz in Figure 33.

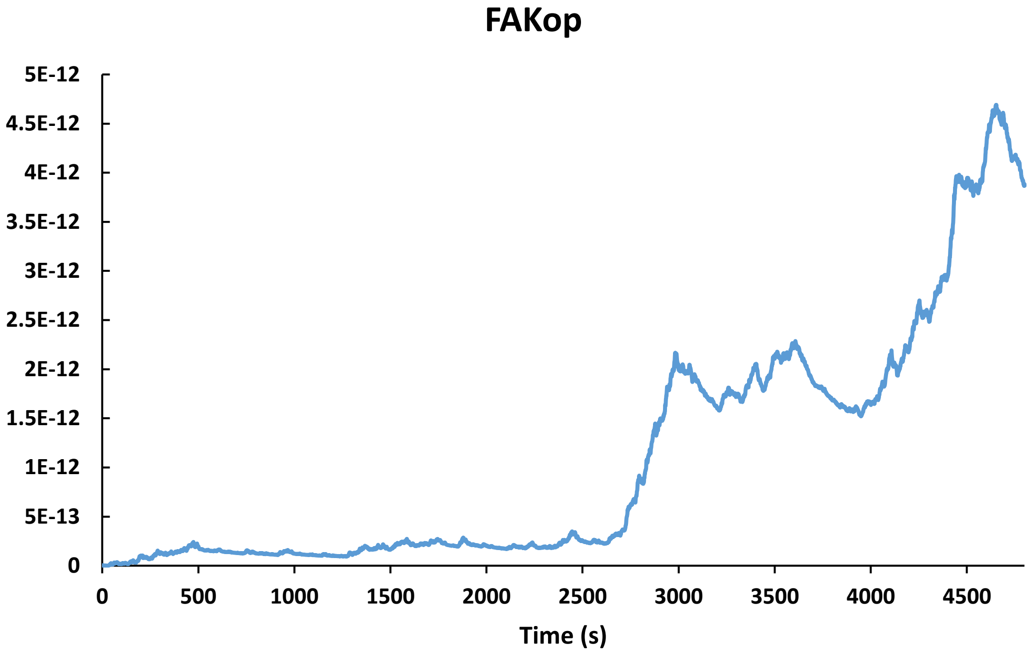

Figure 33: Phosphorylated FAK levels as a direct result of implementing force functions on the integrin receptor via FAK kinetics. Concentration is measured in nanomolar on the y-axis while time is measured in seconds on the x-axis.

The beginning of the Ras/Raf cascade is induced by the GDP to GTP exchange of Ras, which can be observed by the change seen in Figure 34. The GTP state of Ras is a mediator in crosstalk with the Wnt pathway which should therefore be examined.

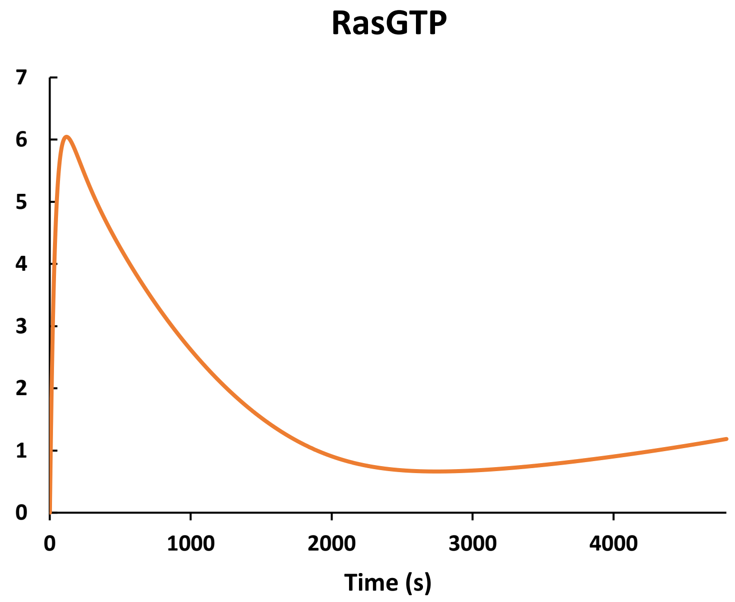

Figure 34: Activated Ras (RasGTP) levels during US stimulation. Concentration is measured in nanomolar on the y-axis while time is measured in seconds on the x-axis.

Phosphorylation of ERK was shown to slightly increase at the end of pLIUS application and eventually peaked at a 2.26-fold increase 10-20 min after stimulation (Zhou *et al.* 2004). The model here was run for the entire eight minutes of cLIUS stimulation where a 1.26-fold increase was observed, seen in Figure 35 (a) along with all overall ERK configurations (b).

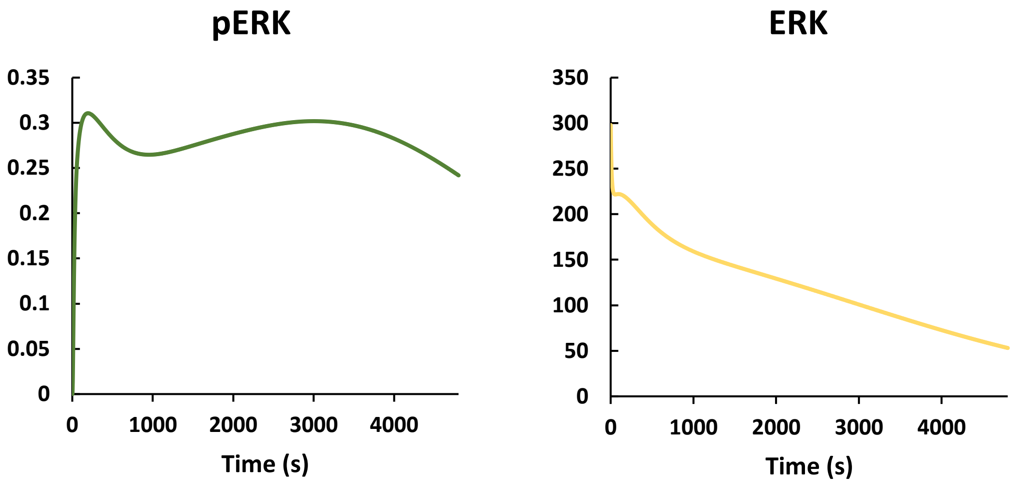

Figure 35: Phosphorylated ERK (pERK) and ERK changes. Concentration is measured in nanomolar on the y-axis while time is measured in seconds on the x-axis.

The changes in the TGF-β pathway can be seen by the changes in Smad2/3 levels. This is monitored throughout the US stimulation by Figure 36. Time is shortened here to better show how rapidly Smad levels are depleted.

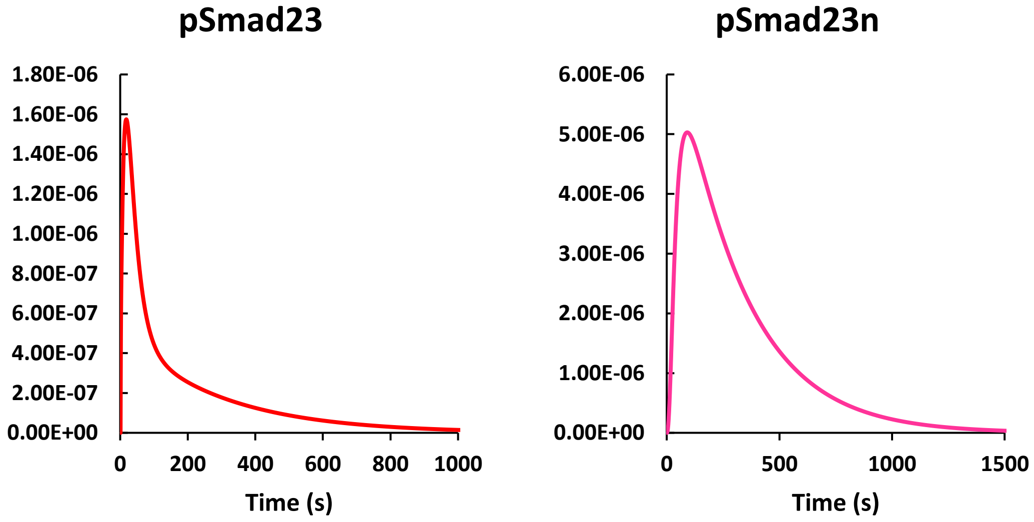

Figure 36: Phosphorylated Smad2/3 and phosphorylated nuclear Smad2/3 levels during US stimulation. Concentration is measured in nanomolar on the y-axis while time is measured in seconds on the x-axis.

Finally, we can see the changes in the Wnt pathway. Accumulation of β-catenin is shown by Figure 37(a), while the transcriptional coactivator can be seen in (b). These levels are similar to those seen in modeling done by Kim et al., though the time to reach these levels are reduced due to US stimulation increasing reaction kinetics within the pathway (Kim *et al.*, 2007).

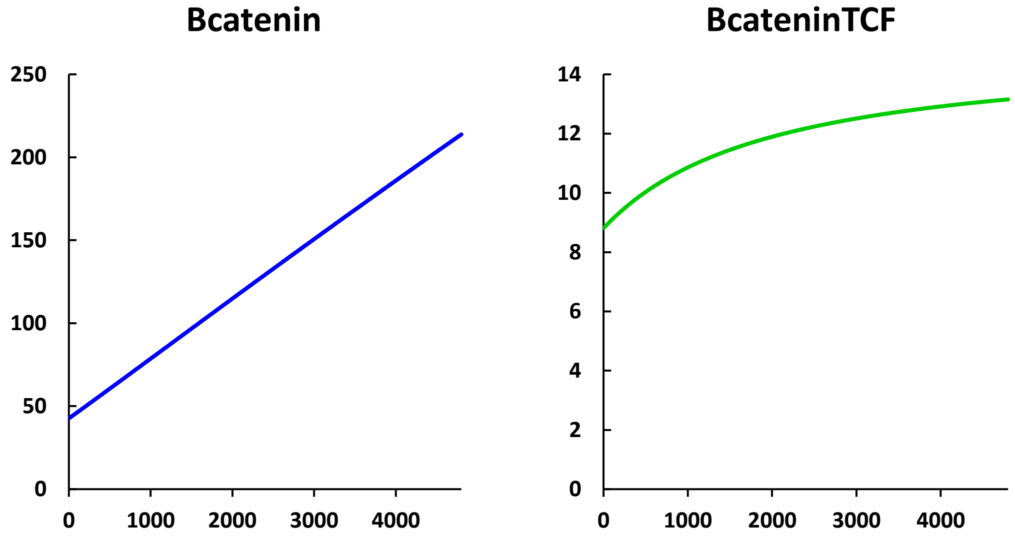

Figure 37: Levels of β-catenin. Concentration is measured in nanomolar on the y-axis while time is measured in seconds on the x-axis.

Overall, these model results show that ultrasound stimulation results in faster kinetics in intracellular pathways.

4.6 CONCLUSION

The three models utilized here have provided a basis for the beginning stage of chondrogenesis, condensation. Individually these models are well established from *in vitro* experiments to show their necessity during condensation. Through research applying mechanical stress to cells, it has been well shown that cells utilize force sensors in a variety of ways through adhesion-associated proteins that activate downstream signal pathways (Cheng *et al.*, 2017). Here we show the effects of cLIUS on key pathways during MSC condensation resulting in multi-fold increases in protein levels. These levels have been confirmed through individual pathway models, and tied together here through proposed crosstalk rate kinetics in similar magnitudes. These findings are consistent with the mechano-sensing function of FAK holding a critical role in membrane mechanotransduction (Zhou *et al*., 2015).

Further experimentation could lead to a more accurate model as well as a better understanding of the interactions of the pathways. Higher accuracy could also be attained in the sole use of MSCs during *in vitro* experiments to further show US effects on these pathways. This model describes the TGF-β receptors in a similar fashion to the FAK receptors. This conclusion was reached as integrins are key mechanisms in extracellular TGF-β activation (Angelini *et al*., 2020).

CHAPTER 5 – FUTURE DIRECTIONS

The work presented here was based on rabbit experiments done to show the effects of continuous pulsed ultrasound on cartilage tissue. It expands on previous experimental findings and two-dimensional modeling. Further expansion in modeling should be done to better describe the viscoelastic behavior of muscle tissue in the *in vivo* model. Clinical protocols utilizing US for therapy has shown variable results; this could be due to lack of application optimization which should be examined.

The 3D modeling environment here is described with linear elastics and attenuation coefficients found from literature. This analysis shows a good basis for future models to be built upon. Muscle is described as a viscoelastic material, and can be accounted for in other packages in COMSOL. Attenuation coefficients could also easily be confirmed or found in simple laboratory experiments. The overall goal is to determine efficient energy coupling to the cell which enhances bioeffects in the cell. A large scale model in the 3D environment incorporating cells in the cartilage tissue layer should be further studied. The biopsy punch model here was a good start to that, though in the 3D environment could become more computationally expensive than models already run.

5.1 HUMAN APPLICATION OF cLIUS

Limited human applications of ultrasound for cartilage regeneration have been done thus far. Human biology is larger in scale to rabbit including larger muscle and fat mass. The effect of this on ultrasound applications has not been investigated theoretically. A complete model including all tissues would give better insight to exactly how the macroscopic system responds to US stimulation.

Clinical protocol development is the desired result from research. The results here indicate that MSCs after microfracture procedures should utilize a frequency of 2.1MHz applied for only the first two days. After that time period, interchanging with 3.8MHz should be done to decrease inflammation markers. From the third day on the treatment should be switched completely to 3.8MHz. Our animal models were done for 8min/day, for 5days/week. The time applied should be confirmed or optimized in additional studies.

5.2 ALL-INCLUSIVE PATHWAY MODEL

The comprehensive pathway model included here only describes the first stage of chondrogenesis marked by specific protein expressions. Ideally future work would focus on confirming US effects to each pathway and obtaining more accurate kinetic data. Kinetic data here was obtained by a variety of cell types. Future experiments should utilize one type – preferably human bone marrow-derived MSCs.

Expanding the model would have to include piecewise functions to signal the start of other pathways important in later stages of chondrogenesis. Those pathways and ion channels would have to be included in what is already a large model, and shortening each pathway would be necessary for computational restraints. Each pathway should be examined in the in vitro environment with cLIUS application to observe its effects on protein expression levels.

There is some speculation on the mechanisms which US effects nuclear shuttling of cytoplasmic proteins. This should further be studied to examine just how that occurs. Whether it be increased kinetics from upstream US modulation, or a function of US akin to the mechanosensing description of FAK.

REFERENCES

1. Abuammah, A., Maimari, N., Towhidi, L., Frueh, J., Chooi, K. Y., Warboys, C., & Krams, R. (2018). New developments in mechanotransduction: Cross talk of the Wnt, TGF-β and Notch signalling pathways in reaction to shear stress. *Current Opinion in Biomedical Engineering*, *5*, 96-104.
2. Akhmetshina, A., Palumbo, K., Dees, C., Bergmann, C., Venalis, P., Zerr, P., ... & Distler, J. H. (2012). Activation of canonical Wnt signalling is required for TGF-β-mediated fibrosis. *Nature communications*, *3*(1), 1-12.
3. Alexopoulos, L. G., Williams, G. M., Upton, M. L., Setton, L. A., & Guilak, F. BIPHASIC PROPERTIES OF NORMAL AND OSTEOARTHRITIC HUMAN CHONDRONS.
4. Aliabouzar, M., Zhang, L. G., & Sarkar, K. (2016). Lipid coated microbubbles and low intensity pulsed ultrasound enhance chondrogenesis of human mesenchymal stem cells in 3D printed scaffolds. *Scientific reports*, *6*(1), 1-11.
5. Allard, J. F. (1993). Biot theory of sound propagation in porous materials having an elastic frame. In *Propagation of Sound in Porous Media* (pp. 118-144). Springer, Dordrecht.
6. Allard, J., & Atalla, N. (2009). *Propagation of sound in porous media: modelling sound absorbing materials 2e*. John Wiley & Sons.
7. Angelini, A., Trial, J., Ortiz-Urbina, J., & Cieslik, K. A. (2020). Mechanosensing dysregulation in the fibroblast: a hallmark of the aging heart. Ageing Research Reviews, 101150.
8. Arden, N., & Nevitt, M. C. (2006). Osteoarthritis: epidemiology. *Best practice & research Clinical rheumatology*, *20*(1), 3-25.
9. Atalla, N., Panneton, R., & Debergue, P. (1998). A mixed displacement-pressure formulation for poroelastic materials. *The Journal of the Acoustical Society of America*, *104*(3), 1444-1452.
10. Azhari, H. (2010). Basics of biomedical ultrasound for engineers. John Wiley & Sons.
11. Bang, O. S., Kim, E. J., Chung, J. G., Lee, S. R., Park, T. K., & Kang, S. S. (2000). Association of focal adhesion kinase with fibronectin and paxillin is required for precartilage condensation of chick mesenchymal cells. *Biochemical and biophysical research communications*, *278*(3), 522-529.
12. Basser PJ, Schneiderman R, Bank RA, Wachtel E, Maroudas A. Mechanical properties of the collagen network in human articular cartilage as measured by osmotic stress technique. Arch Biochem Biophys. 1998;351(2):207-219.
13. Benninghoff, A. (1925). Form und Bau der Gelenkknorpel in ihren Beziehungen zur Funktion. *Zeitschrift für Zellforschung und mikroskopische Anatomie, 2*(5), 783-862.

14. Best, T. M., Wilk, K. E., Moorman, C. T., & Draper, D. O. (2016). Low intensity ultrasound for promoting soft tissue healing: a systematic review of the literature and medical technology. *Internal medicine review (Washington, DC: Online)*, *2*(11).

15. Betancourt, M. C. C., Cailotto, F., Kerkhof, H. J., Cornelis, F. M., Doherty, S. A., Hart, D. J., ... & van Meurs, J. B. (2012). Genome-wide association and functional studies identify the DOT1L gene to be involved in cartilage thickness and hip osteoarthritis. *Proceedings of the National Academy of Sciences*, *109*(21), 8218-8223.

16. Bhosale, A. M., & Richardson, J. B. (2008). Articular cartilage: structure, injuries and review of management. *British medical bulletin*, *87*(1), 77-95.

17. Bigelow, T. A. (2001). Experimental evaluation of nonlinear indices for ultrasound transducer characterizations (Doctoral dissertation, University of Illinois at Urbana-Champaign).

18. Biot, M. A. (1941). General theory of three-dimensional consolidation. *Journal of applied physics*, *12*(2), 155-164.

19. Biot, M. A. (1956). Theory of propagation of elastic waves in a fluid-saturated porous solid. II. Higher frequency range. *The Journal of the acoustical Society of america*, *28*(2), 179-191.

20. Biot, M. A. (1962). Mechanics of deformation and acoustic propagation in porous media. *Journal of applied physics*, *33*(4), 1482-1498.

21. Bobick, B. E., & Kulyk, W. M. (2004). The MEK-ERK signaling pathway is a negative regulator of cartilage-specific gene expression in embryonic limb mesenchyme. *Journal of Biological Chemistry*, *279*(6), 4588-4595.

22. Boushell, M. K., Hung, C. T., Hunziker, E. B., Strauss, E. J., & Lu, H. H. (2017). Current strategies for integrative cartilage repair. *Connective tissue research*, *58*(5), 393-406.

23. Budhiraja, G., Sahu, N., & Subramanian, A. (2018). Low-intensity ultrasound upregulates the expression of cyclin-D1 and promotes cellular proliferation in human mesenchymal stem cells. *Biotechnology journal*, *13*(4), 1700382.

24. Bullock, W. A., Plotkin, L. I., Robling, A. G., & Pavalko, F. M. (2018). Mechanotransduction in bone formation and maintenance. *Primer on the Metabolic Bone Diseases and Disorders of Mineral Metabolism*, 75-83.

25. Cameron, John R.; James G. Skofronick & Roderick M. Grant. Physics of the Body. Second Edition. Madison, WI: Medical Physics Publishing, 1999: 96.

26. Cardoso, L., Fritton, S. P., Gailani, G., Benalla, M., & Cowin, S. C. (2013). Advances in assessment of bone porosity, permeability and interstitial fluid flow. Journal of biomechanics, 46(2), 253-265.

27. Castillo, M., Acevedo, P., & Moreno, E. (2003). KLM model for lossy piezoelectric transducers. *Ultrasonics*, *41*(8), 671-679.

28. Chen, D., Shen, J., Zhao, W., Wang, T., Han, L., Hamilton, J. L., & Im, H. J. (2017). Osteoarthritis: toward a comprehensive understanding of pathological mechanism. Bone research, 5(1), 1-13.

29. Chen, W. H., Lai, M. T., Wu, A. T., Wu, C. C., Gelovani, J. G., Lin, C. T., ... & Deng, W. P. (2009). *In vitro* stage-specific chondrogenesis of mesenchymal stem cells committed to chondrocytes. *Arthritis & Rheumatism: Official Journal of the American College of Rheumatology*, *60*(2), 450-459.

30. Cheng, B., Lin, M., Huang, G., Li, Y., Ji, B., Genin, G. M., ... & Xu, F. (2017). Cellular mechanosensing of the biophysical microenvironment: a review of mathematical models of biophysical regulation of cell responses. *Physics of life reviews*, *22*, 88-119.

31. COMSOL. (2018). COMSOL Acoustics Module User's Guide.

32. Cook, S. D., Salkeld, S. L., Popich-Patron, L. S., Ryaby, J. P., Jones, D. G., & Barrack, R. L. (2001). Improved cartilage repair after treatment with low-intensity pulsed ultrasound. *Clinical Orthopaedics and Related Research (1976-2007)*, *391*, S231-S243.

33. Coricor, G., & Serra, R. (2016). TGF-β regulates phosphorylation and stabilization of Sox9 protein in chondrocytes through p38 and Smad dependent mechanisms. *Scientific reports*, *6*(1), 1-11.

34. Cui, J. H., Park, K., Park, S. R., & Min, B. H. (2006). Effects of low-intensity ultrasound on chondrogenic differentiation of mesenchymal stem cells embedded in polyglycolic acid: an in vivo study. *Tissue engineering*, *12*(1), 75-82.

35. Day, T. F., Guo, X., Garrett-Beal, L., & Yang, Y. (2005). Wnt/β-catenin signaling in mesenchymal progenitors controls osteoblast and chondrocyte differentiation during vertebrate skeletogenesis. *Developmental cell*, *8*(5), 739-750.

36. Dill, K. A., Bromberg, S., & Stigter, D. (2010). *Molecular driving forces: statistical thermodynamics in biology, chemistry, physics, and nanoscience*. Garland Science.

37. Duda, G. N., Kliche, A., Kleemann, R., Hoffmann, J. E., Sittinger, M., & Haisch, A. (2004). Does low-intensity pulsed ultrasound stimulate maturation of tissue-engineered cartilage?. Journal of Biomedical Materials Research Part B: Applied Biomaterials: An Official Journal of The Society for Biomaterials, The Japanese Society for Biomaterials, and The Australian Society for Biomaterials and the Korean Society for Biomaterials, 68(1), 21-28.

38. Dudko, O. K., Hummer, G., & Szabo, A. (2006). Intrinsic rates and activation free energies from single-molecule pulling experiments. *Physical review letters*, *96*(10), 108101.

39. Dyson, M., Moodley, S., Verjee, L., Verling, W., Weinman, J., & Wilson, P. (2003). Wound healing assessment using 20 MHz ultrasound and photography. *Skin Research and Technology*, *9*(2), 116-121.

40. Elsaid, K. A., Jay, G. D., Warman, M. L., Rhee, D. K., & Chichester, C. O. (2005). Association of articular cartilage degradation and loss of boundary-lubricating ability of synovial fluid following injury and inflammatory arthritis. *Arthritis & Rheumatism*, *52*(6), 1746-1755.

41. Facchin, F., Bianconi, E., Canaider, S., Basoli, V., Biava, P. M., & Ventura, C. (2018). Tissue Regeneration without Stem Cell Transplantation: Self-Healing Potential from Ancestral Chemistry and Physical Energies. *Stem cells international*, *2018*.

42. Feigin, M., Zwecker, M., Freedman, D., & Anthony, B. W. (2020, July). Detecting muscle activation using ultrasound speed of sound inversion with deep learning. In 2020 42nd Annual International Conference of the IEEE Engineering in Medicine & Biology Society (EMBC) (pp. 2092-2095). IEEE.

43. Fellah, Z. E. A., Chapelon, J. Y., Berger, S., Lauriks, W., & Depollier, C. (2004). Ultrasonic wave propagation in human cancellous bone: Application of Biot theory. *The Journal of the acoustical Society of america*, *116*(1), 61-73.

44. Findlay, D. M., & Atkins, G. J. (2014). Osteoblast-chondrocyte interactions in osteoarthritis. *Current osteoporosis reports*, *12*(1), 127-134.

45. Sophia Fox, A. J., Bedi, A., & Rodeo, S. A. (2009). The basic science of articular cartilage: structure, composition, and function. *Sports health*, *1*(6), 461-468.

46. Franciosa, P., & Gerbino, S. (2010). From CT scan to plantar pressure map distribution of a 3D anatomic human foot. In *COMSOL conference*.

47. Freitag, J., Bates, D., Boyd, R., Shah, K., Barnard, A., Huguenin, L., & Tenen, A. (2016). Mesenchymal stem cell therapy in the treatment of osteoarthritis: reparative pathways, safety and efficacy–a review. *BMC musculoskeletal disorders*, *17*(1), 230.

48. Fujioka, A., Terai, K., Itoh, R. E., Aoki, K., Nakamura, T., Kuroda, S., ... & Matsuda, M. (2006). Dynamics of the Ras/ERK MAPK cascade as monitored by fluorescent probes. Journal of Biological Chemistry, 281(13), 8917-8926.

49. Furuhashi, M., Yagi, K., Yamamoto, H., Furukawa, Y., Shimada, S., Nakamura, Y., ... & Kato, M. (2001). Axin facilitates Smad3 activation in the transforming growth factor β signaling pathway. *Molecular and cellular biology*, *21*(15), 5132-5141.

50. Furumatsu, T., Tsuda, M., Taniguchi, N., Tajima, Y., & Asahara, H. (2005). Smad3 Induces Chondrogenesis through the Activation of SOX9 via CREB-binding Protein/p300 Recruitment*[boxs]. *Journal of Biological Chemistry*, *280*(9), 8343-8350.

51. Gadjanski, I., Spiller, K., & Vunjak-Novakovic, G. (2012). Time-dependent processes in stem cell-based tissue engineering of articular cartilage. *Stem Cell Reviews and Reports*, *8*(3), 863-881.

52. Goldring, M. B. (2000). Osteoarthritis and cartilage: the role of cytokines. *Current rheumatology reports*, *2*(6), 459-465.

53. Goldring, M. B., Tsuchimochi, K., & Ijiri, K. (2006). The control of chondrogenesis. Journal of cellular biochemistry, 97(1), 33-44.

54. Grande, D. A., Pitman, M. I., Peterson, L., Menche, D., & Klein, M. (1989). The repair of experimentally produced defects in rabbit articular cartilage by autologous chondrocyte transplantation. *Journal of Orthopaedic Research*, *7*(2), 208-218.

55. Greene, M. A., & Loeser, R. F. (2015). Aging-related inflammation in osteoarthritis. *Osteoarthritis and cartilage*, *23*(11), 1966-1971.

56. Guilak, F., Alexopoulos, L. G., Upton, M. L., Youn, I., Choi, J. B., Cao, L., ... & Haider, M. A. (2006). The pericellular matrix as a transducer of biomechanical and

biochemical signals in articular cartilage. *Annals of the New York Academy of Sciences, 1068*(1), 498-512.

57. Guilak, F., Fermor, B., Keefe, F. J., Kraus, V. B., Olson, S. A., Pisetsky, D. S., ... & Weinberg, J. B. (2004). The role of biomechanics and inflammation in cartilage injury and repair. *Clinical Orthopaedics and Related Research®, 423*, 17-26.

58. Guo, M., Pegoraro, A. F., Mao, A., Zhou, E. H., Arany, P. R., Han, Y., ... & Weitz, D. A. (2017). Cell volume change through water efflux impacts cell stiffness and stem cell fate. *Proceedings of the National Academy of Sciences*, *114*(41), E8618-E8627.

59. Guo, X., & Wang, X. F. (2009). Signaling cross-talk between TGF-β/BMP and other pathways. *Cell research*, *19*(1), 71-88.

60. Guo, H., Maher, S. A., & Spilker, R. L. (2013). Biphasic finite element contact analysis of the knee joint using an augmented Lagrangian method. *Medical engineering & physics*, *35*(9), 1313-1320.

61. Hadjiargyrou, M., McLeod, K., Ryaby, J. P., & Rubin, C. (1998). Enhancement of fracture healing by low intensity ultrasound. *Clinical Orthopaedics and Related Research®, 355,* S216-S229.

62. Haider, M. A. (2004). A radial biphasic model for local cell-matrix mechanics in articular cartilage. *SIAM Journal on Applied Mathematics*, *64*(5), 1588-1608.

63. Haider, M. A., Schugart, R. C., Setton, L. A., & Guilak, F. (2006). A mechano-chemical model for the passive swelling response of an isolated chondron under osmotic loading. *Biomechanics and modeling in mechanobiology*, *5*(2-3), 160.

64. Ham, O., Lee, C. Y., Kim, R., Lee, J., Oh, S., Lee, M. Y., ... & Chang, W. (2015). Therapeutic potential of differentiated mesenchymal stem cells for treatment of osteoarthritis. *International journal of molecular sciences*, *16*(7), 14961-14978.

65. Han, S. K., Madden, R., Abusara, Z., & Herzog, W. (2012). In situ chondrocyte viscoelasticity. *Journal of biomechanics*, *45*(14), 2450-2456.

66. Han, B., Li, Q., Wang, C., Patel, P., Adams, S. M., Doyran, B., ... & Han, L. (2019). Decorin regulates the aggrecan network integrity and biomechanical functions of cartilage extracellular matrix. *ACS nano*, *13*(10), 11320-11333.

67. Harle, J., Mayia, F., Olsen, I., & Salih, V. (2005). Effects of ultrasound on transforming growth factor-beta genes in bone cells. *European Cells and Materials, 10,* 70-77.

68. Haudenschild, D. R., Chen, J., Pang, N., Lotz, M. K., & D'Lima, D. D. (2010). Rho kinase–dependent activation of SOX9 in chondrocytes. *Arthritis & Rheumatism: Official Journal of the American College of Rheumatology*, *62*(1), 191-200.

69. Hayashida, T., de Caestecker, M., & Schnaper, H. W. (2003). Cross-talk between ERK MAP kinase and Smad-signaling pathways enhances TGF-β dependent responses in human mesangial cells. *The FASEB journal*, *17*(11), 1-21.

70. Hens, J. R., Wilson, K. M., Dann, P., Chen, X., Horowitz, M. C., & Wysolmerski, J. J. (2005). TOPGAL mice show that the canonical Wnt signaling pathway is active

during bone development and growth and is activated by mechanical loading *in vitro*. *Journal of bone and mineral research*, *20*(7), 1103-1113.

71. Horas, U., Pelinkovic, D., Herr, G., Aigner, T., & Schnettler, R. (2003). Autologous chondrocyte implantation and osteochondral cylinder transplantation in cartilage repair of the knee joint: a prospective, comparative trial. *JBJS*, *85*(2), 185-192.

72. Hosoda, N., Sakai, N., Sawae, Y., & Murakami, T. (2009). Finite element analysis of articular cartilage model considering the configuration and biphasic property of the tissue. In 13th International Conference on Biomedical Engineering (pp. 1883-1887). Springer, Berlin, Heidelberg.

73. Houard, X., Goldring, M. B., & Berenbaum, F. (2013). Homeostatic mechanisms in articular cartilage and role of inflammation in osteoarthritis. *Current rheumatology reports*, *15*(11), 375.

74. Huang, F., & Chen, Y. G. (2012). Regulation of TGF-β receptor activity. *Cell & bioscience*, *2*(1), 1-10.

75. Huang, X., Das, R., Patel, A., & Nguyen, T. D. (2018). Physical stimulations for bone and cartilage regeneration. *Regenerative engineering and translational medicine*, *4*(4), 216-237.

76. Huey, D. J., Hu, J. C., & Athanasiou, K. A. (2012). Unlike bone, cartilage regeneration remains elusive. *Science*, *338*(6109), 917-921.

77. Hunziker, E. B., Quinn, T. M., & Häuselmann, H. J. (2002). Quantitative structural organization of normal adult human articular cartilage. *Osteoarthritis and Cartilage*, *10*(7), 564-572.

78. Hughes, E. R., Leighton, T. G., White, P. R., & Petley, G. W. (2007). Investigation of an anisotropic tortuosity in a Biot model of ultrasonic propagation in cancellous bone. *The Journal of the Acoustical Society of America*, *121*(1), 568-574.

79. Ingber, D. (1991). Integrins as mechanochemical transducers. *Current opinion in cell biology*, *3*(5), 841-848.

80. Ioan-Facsinay, A., & Kloppenburg, M. (2013). An emerging player in knee osteoarthritis: the infrapatellar fat pad. *Arthritis research & therapy*, *15*(6), 1-9.

81. Jang, K. W., Ding, L., Seol, D., Lim, T. H., Buckwalter, J. A., & Martin, J. A. (2014). Low-intensity pulsed ultrasound promotes chondrogenic progenitor cell migration via focal adhesion kinase pathway. *Ultrasound in medicine & biology*, *40*(6), 1177-1186.

82. Javelaud, D., & Mauviel, A. (2005). Crosstalk mechanisms between the mitogen-activated protein kinase pathways and Smad signaling downstream of TGF-β: implications for carcinogenesis. *Oncogene*, *24*(37), 5742-5750.

83. Jebens, E. H., & Monk-Jones, M. E. (1959). On the viscosity and pH of synovial fluid and the pH of blood. *The Journal of bone and joint surgery. British volume*, *41*(2), 388-400.

84. Kar, B., & Wallrabe, U. (2020). Performance enhancement of an ultrasonic power transfer system through a tightly coupled solid media using a KLM model. *Micromachines*, *11*(4), 355.

85. Kawasaki, S., Ueda, R., Hasegawa, A., Fujita, A., Mihata, T., Matsukawa, M., & Neo, M. (2015). Ultrasonic wave properties of human bone marrow in the femur and tibia. *The Journal of the Acoustical Society of America*, *138*(1), EL83-EL87.

86. Kim, E., Guilak, F., & Haider, M. A. (2008). The dynamic mechanical environment of the chondrocyte: a biphasic finite element model of cell-matrix interactions under cyclic compressive loading. *Journal of biomechanical engineering*, *130*(6).

87. Kim, D., Rath, O., Kolch, W., & Cho, K. H. (2007). A hidden oncogenic positive feedback loop caused by crosstalk between Wnt and ERK pathways. *Oncogene*, *26*(31), 4571-4579.

88. Kim, I. G., Ko, J., Lee, H. R., Do, S. H., & Park, K. (2016). Mesenchymal cells condensation-inducible mesh scaffolds for cartilage tissue engineering. *Biomaterials*, *85*, 18-29.

89. Kim, G., Seo, M. K., Choi, N., Baek, K. S., & Kim, K. B. (2019). Application of KLM model for an ultrasonic through-transmission method. *International Journal of Precision Engineering and Manufacturing*, *20*(3), 383-393.

90. Kinsler, L. E., Frey, A. R., Coppens, A. B., & Sanders, J. V. (2000). *Fundamentals of acoustics*. John wiley & sons.

91. Kirton, J. P., Crofts, N. J., George, S. J., Brennan, K., & Canfield, A. E. (2007). Wnt/β-catenin signaling stimulates chondrogenic and inhibits adipogenic differentiation of pericytes: Potential relevance to vascular disease?. *Circulation research*, *101*(6), 581-589.

92. Kon, E., Filardo, G., Roffi, A., Andriolo, L., & Marcacci, M. (2012). New trends for knee cartilage regeneration: from cell-free scaffolds to mesenchymal stem cells. *Current reviews in musculoskeletal medicine*, *5*(3), 236-243.

93. Korhonen, R. K., Laasanen, M. S., Töyräs, J., Lappalainen, R., Helminen, H. J., & Jurvelin, J. S. (2003). Fibril reinforced poroelastic model predicts specifically mechanical behavior of normal, proteoglycan depleted and collagen degraded articular cartilage. Journal of biomechanics, 36(9), 1373-1379.

94. Korstjens, C. M., Van der Rijt, R. H. H., Albers, G. H. R., Semeins, C. M., & Klein-Nulend, J. (2008). Low-intensity pulsed ultrasound affects human articular chondrocytes *in vitro*. *Medical & biological engineering & computing*, *46*(12), 1263-1270.

95. Krimholtz, R., Leedom, D. A., & Matthaei, G. L. (1970). New equivalent circuits for elementary piezoelectric transducers. *Electronics Letters*, *6*(13), 398-399.

96. Krueger, T. E., Thorek, D. L., Denmeade, S. R., Isaacs, J. T., & Brennen, W. N. (2018). Concise review: Mesenchymal stem cell-based drug delivery: The good, the bad, the ugly, and the promise. *Stem cells translational medicine*, *7*(9), 651-663.

97. Kulkarni, V. (2011). Flexible Two-dimensional Ultrasonic Transducer Array: Design, Fabrication and Characterization.

98. Kuo, A. C., Rodrigo, J. J., Reddi, A. H., Curtiss, S., Grotkopp, E., & Chiu, M. (2006). Microfracture and bone morphogenetic protein 7 (BMP-7) synergistically stimulate articular cartilage repair. *Osteoarthritis and cartilage*, *14*(11), 1126-1135.

99. Kuthe, C. D., & Uddanwadiker, R. V. (2016). Investigation of effect of fiber orientation on mechanical behavior of skeletal muscle. Journal of Applied Biomaterials & Functional Materials, 14(2), 154-162.

100. Lai, W. C., Iglesias, B. C., Mark, B. J., & Wang, D. (2021). Low-intensity pulsed ultrasound augments tendon, ligament, and bone-soft tissue healing in preclinical animal models: A systematic review. *Arthroscopy: The Journal of Arthroscopic & Related Surgery*.

101. Lee, H. J., Choi, B. H., Min, B. H., Son, Y. S., & Park, S. R. (2006). Low-intensity ultrasound stimulation enhances chondrogenic differentiation in alginate culture of mesenchymal stem cells. *Artificial organs*, *30*(9), 707-715.

102. Lee, H. J., Choi, B. H., Min, B. H., & Park, S. R. (2007). Low-intensity ultrasound inhibits apoptosis and enhances viability of human mesenchymal stem cells in three-dimensional alginate culture during chondrogenic differentiation. *Tissue Engineering*, *13*(5), 1049-1057.

103. Li, J., & Dong, S. (2016). The signaling pathways involved in chondrocyte differentiation and hypertrophic differentiation. Stem cells international, 2016.

104. Li, J., Zhao, Z., Liu, J., Huang, N., Long, D., Wang, J., ... & Liu, Y. (2010). MEK/ERK and p38 MAPK regulate chondrogenesis of rat bone marrow mesenchymal stem cells through delicate interaction with TGF-β1/Smads pathway. *Cell proliferation*, *43*(4), 333-343.

105. Liang, X., & Boppart, S. A. (2009). Biomechanical properties of in vivo human skin from dynamic optical coherence elastography. *IEEE Transactions on Biomedical Engineering*, *57*(4), 953-959.

106. Lieberthal, J., Sambamurthy, N., & Scanzello, C. R. (2015). Inflammation in joint injury and post-traumatic osteoarthritis. *Osteoarthritis and cartilage*, *23*(11), 1825-1834.

107. Liu, S., Iaria, J., Simpson, R. J., & Zhu, H. J. (2018). Ras enhances TGF-β signaling by decreasing cellular protein levels of its type II receptor negative regulator SPSB1. *Cell Communication and Signaling*, *16*(1), 1-15.

108. London, N. J., Miller, L. E., & Block, J. E. (2011). Clinical and economic consequences of the treatment gap in knee osteoarthritis management. *Medical hypotheses*, *76*(6), 887-892.

109. Loyola-Sánchez, A., Richardson, J., Beattie, K. A., Otero-Fuentes, C., Adachi, J. D., & MacIntyre, N. J. (2012). Effect of low-intensity pulsed ultrasound on the cartilage repair in people with mild to moderate knee osteoarthritis: a double-blinded, randomized, placebo-controlled pilot study. *Archives of physical medicine and rehabilitation*, *93*(1), 35-42.

110. Louw, T. M., Budhiraja, G., Viljoen, H. J., & Subramanian, A. (2013). Mechanotransduction of ultrasound is frequency dependent below the cavitation threshold. *Ultrasound in medicine & biology*, *39*(7), 1303-1319.

111. Louw, T. M., Subramanian, A., & Viljoen, H. J. (2015). Theoretical evaluation of the acoustic field in an ultrasonic bioreactor. *Ultrasound in medicine & biology, 41*(6), 1766-1778.

112. Madsen, E. L., Zagzebski, J. A., Banjavie, R. A., & Jutila, R. E. (1978). Tissue mimicking materials for ultrasound phantoms. *Medical physics, 5*(5), 391-394.

113. Mardones, R., & Larrain, C. (2015). Cartilage restoration technique of the hip. *Journal of hip preservation surgery*, *3*(1), 30-36.

114. Martin, A. D., Daniel, M. Z., Drinkwater, D. T., & Clarys, J. P. (1994). Adipose tissue density, estimated adipose lipid fraction and whole body adiposity in male cadavers. *International journal of obesity and related metabolic disorders: journal of the International Association for the Study of Obesity*, *18*(2), 79-83.

115. Mfoumou, E., Tripette, J., Blostein, M., & Cloutier, G. (2014). Time-dependent hardening of blood clots quantitatively measured in vivo with shear-wave ultrasound imaging in a rabbit model of venous thrombosis. *Thrombosis research*, *133*(2), 265-271.

116. Miller, A. D. (2017). *Mathematical Modeling of Ultrasound in Regenerative Medicine: From the Cellular Scale to the Macroscale*. The University of Nebraska-Lincoln.

117. Miller, A. D., Subramanian, A., & Viljoen, H. J. (2017). A nonlinear model of cell interaction with an acoustic field. *Journal of biomechanics*, *56*, 83-88.

118. Miller, A. D., Subramanian, A., & Viljoen, H. J. (2017). Theoretically proposed optimal frequency for ultrasound induced cartilage restoration. *Theoretical Biology and Medical Modelling*, *14*(1), 1-14.

119. Min, B. H., Choi, B. H., & Park, S. R. (2007). Low intensity ultrasound as a supporter of cartilage regeneration and its engineering. *Biotechnology and Bioprocess Engineering*, *12*(1), 22-31.

120. Misra, S., Ramesh, K. T., & Okamura, A. M. (2008). Modeling of tool-tissue interactions for computer-based surgical simulation: A literature review. Presence: Teleoperators and Virtual Environments, 17(5), 463-491.

121. Mithoefer, K., McAdams, T., Williams, R. J., Kreuz, P. C., & Mandelbaum, B. R. (2009). Clinical efficacy of the microfracture technique for articular cartilage repair in the knee: an evidence-based systematic analysis. *The American journal of sports medicine*, *37*(10), 2053-2063.

122. Moran, C. M., Bush, N. L., & Bamber, J. C. (1995). Ultrasonic propagation properties of excised human skin. Ultrasound in Medicine and Biology, 21(9), 1177-1190.

123. Morishita, K., Karasuno, H., Yokoi, Y., Morozumi, K., Ogihara, H., Ito, T., ... & Abe, K. (2014). Effects of therapeutic ultrasound on range of motion and stretch pain. *Journal of physical therapy science*, *26*(5), 711-715.

124. Morrisette-Thomas, V., Cohen, A. A., Fülöp, T., Riesco, É., Legault, V., Li, Q., ... & Ferrucci, L. (2014). Inflamm-aging does not simply reflect increases in pro-inflammatory markers. *Mechanisms of ageing and development*, *139*, 49-57.

125. Morse, P. M., & Ingard, K. U. (1986). *Theoretical acoustics*. Princeton university press.

126. Morshed, A., Dutta, P., & Dillon, R. H. (2018). Mathematical modeling and numerical simulation of the tgf-β/smad signaling pathway in tumor microenvironments. *Applied Numerical Mathematics*, *133*, 41-51.

127. Moskowitz, R. W., Kelly, M. A., & Lewallen, D. G. (2004). Understanding osteoarthritis of the knee--causes and effects. American Journal of Orthopedics (Belle Mead, NJ), 33(2 Suppl), 5-9.

128. Mow, V. C., Wang, C. C., & Hung, C. T. (1999). The extracellular matrix, interstitial fluid and ions as a mechanical signal transducer in articular cartilage. *Osteoarthritis and Cartilage*, *7*(1), 41-58.

129. Mukai, S., Ito, H., Nakagawa, Y., Akiyama, H., Miyamoto, M., & Nakamura, T. (2005). Transforming growth factor-β1 mediates the effects of low-intensity pulsed ultrasound in chondrocytes. *Ultrasound in medicine & biology*, *31*(12), 1713-1721.

130. Murrell, G. A., Maddali, S., Horovitz, L., Oakley, S. P., & Warren, R. F. (2001). The effects of time course after anterior cruciate ligament injury in correlation with meniscal and cartilage loss. *The American Journal of Sports Medicine*, *29*(1), 9-14.

131. Myers, S. L., Dines, K. R. I. S., Brandt, D. A., Brandt, K. D., & Albrecht, M. E. (1995). Experimental assessment by high frequency ultrasound of articular cartilage thickness and osteoarthritic changes. *J Rheumatol*, *22*(1), 109-16.

132. Nahirnyak, V. M., Yoon, S. W., & Holland, C. K. (2006). Acousto-mechanical and thermal properties of clotted blood. *The Journal of the Acoustical Society of America*, *119*(6), 3766-3772.

133. Naito, K., Watari, T., Muta, T., Furuhata, A., Iwase, H., Igarashi, M., ... & Kaneko, K. (2010). Low-intensity pulsed ultrasound (LIPUS) increases the articular cartilage type II collagen in a rat osteoarthritis model. *Journal of Orthopaedic Research*, *28*(3), 361-369.

134. Newman, A. P. (1998). Articular cartilage repair. *The American journal of sports medicine*, *26*(2), 309-324.

135. Nguyen, B. V., Wang, Q. G., Kuiper, N. J., El Haj, A. J., Thomas, C. R., & Zhang, Z. (2010). Biomechanical properties of single chondrocytes and chondrons determined by micromanipulation and finite-element modelling. *Journal of The Royal Society Interface*, *7*(53), 1723-1733.

136. O'Hara, B. P., Urban, J. P., & Maroudas, A. (1990). Influence of cyclic loading on the nutrition of articular cartilage. *Annals of the rheumatic diseases*, *49*(7), 536-539.

137. Ohkawa, S., Odamaki, M., Ikegaya, N., Hibi, I., Miyaji, K., & Kumagai, H. (2005). Association of age with muscle mass, fat mass and fat distribution in non-diabetic haemodialysis patients. *Nephrology Dialysis Transplantation*, *20*(5), 945-951.

138. Oldershaw, R. A. (2012). Cell sources for the regeneration of articular cartilage: the past, the horizon and the future. *International journal of experimental pathology*, *93*(6), 389-400.

139. Olkku, A., Leskinen, J. J., Lammi, M. J., Hynynen, K., & Mahonen, A. (2010). Ultrasound-induced activation of Wnt signaling in human MG-63 osteoblastic cells. *Bone*, *47*(2), 320-330.

140. Oshimori, N., & Fuchs, E. (2012). The harmonies played by TGF-β in stem cell biology. *Cell stem cell*, *11*(6), 751-764.

141. Parkin, A., Man, J., Timpson, P., & Pajic, M. (2019). Targeting the complexity of Src signalling in the tumour microenvironment of pancreatic cancer: from mechanism to therapy. *The FEBS journal*, *286*(18), 3510-3539.

142. Pelaez, D., Arita, N., & Cheung, H. S. (2012). Extracellular signal-regulated kinase (ERK) dictates osteogenic and/or chondrogenic lineage commitment of mesenchymal stem cells under dynamic compression. *Biochemical and biophysical research communications*, *417*(4), 1286-1291.

143. Pestka, J. M., Bode, G., Salzmann, G., Südkamp, N. P., & Niemeyer, P. (2012). Clinical outcome of autologous chondrocyte implantation for failed microfracture treatment of full-thickness cartilage defects of the knee joint. *The American journal of sports medicine*, *40*(2), 325-331.

144. Peterson, L., Vasiliadis, H. S., Brittberg, M., & Lindahl, A. (2010). Autologous chondrocyte implantation: a long-term follow-up. *The American journal of sports medicine*, *38*(6), 1117-1124.

145. Pilla, A. A., Mont, M. A., Nasser, P. R., Khan, S. A., Figueiredo, M., Kaufman, J. J., & Siffert, R. S. (1990). Non-invasive low-intensity pulsed ultrasound accelerates bone healing in the rabbit. *Journal of orthopaedic trauma*, *4*(3), 246-253.

146. Poole, C. A., Ayad, S. H. I. R. L. E. Y., & Schofield, J. R. (1988). Chondrons from articular cartilage: I. Immunolocalization of type VI collagen in the pericellular capsule of isolated canine tibial chondrons. *Journal of Cell Science*, *90*(4), 635-643.

147. Pounder, N. M., & Harrison, A. J. (2008). Low intensity pulsed ultrasound for fracture healing: a review of the clinical evidence and the associated biological mechanism of action. Ultrasonics, 48(4), 330-338.

148. Puso, M. A., & Weiss, J. A. (1998). Finite element implementation of anisotropic quasi-linear viscoelasticity using a discrete spectrum approximation.

149. Qi, W. A. N. G., Zhong-li, L. I., Yang-mu, F. U., Zhi-gang, W. A. N. G., Min, W. E. I., Bin, Z. H. A. O., ... & Juan-li, Z. H. U. (2011). Effect of low-energy shock waves in microfracture holes in the repair of articular cartilage defects in a rabbit model. *Chinese medical journal*, *124*(9), 1386-1394.

150. Qureshi, H. Y., Ricci, G., & Zafarullah, M. (2008). Smad signaling pathway is a pivotal component of tissue inhibitor of metalloproteinases-3 regulation by transforming growth factor beta in human chondrocytes. *Biochimica et Biophysica Acta (BBA)-Molecular Cell Research*, *1783*(9), 1605-1612.

151. Raizman, I., De Croos, J. A., Pilliar, R., & Kandel, R. A. (2010). Calcium regulates cyclic compression-induced early changes in chondrocytes during in vitro cartilage tissue formation. *Cell calcium*, *48*(4), 232-242.

152. Rathod, V. T. (2019). A review of electric impedance matching techniques for piezoelectric sensors, actuators and transducers. *Electronics*, *8*(2), 169.

153. Richardson, J. B., Caterson, B., Evans, E. H., Ashton, B. A., & Roberts, S. (1999). Repair of human articular cartilage after implantation of autologous chondrocytes. *The Journal of bone and joint surgery. British volume*, *81*(6), 1064-1068.

154. Robert, H. (2011). Chondral repair of the knee joint using mosaicplasty. *Orthopaedics & Traumatology: Surgery & Research*, *97*(4), 418-429.

155. Rothenberg, J. B., Jayaram, P., Naqvi, U., Gober, J., & Malanga, G. A. (2017). The role of low-intensity pulsed ultrasound on cartilage healing in knee osteoarthritis: a review. PM&R, 9(12), 1268-1277.

156. Rubak, J. M., Poussa, M., & Ritsilá, V. (1982). Chondrogenesis in repair of articular cartilage defects by free periosteal grafts in rabbits. *Acta Orthopaedica Scandinavica*, *53*(2), 181-186.

157. Ruiz, J. P., Pelaez, D., Dias, J., Ziebarth, N. M., & Cheung, H. S. (2012). The effect of nicotine on the mechanical properties of mesenchymal stem cells. *Cell health and cytoskeleton*, *4*, 29.

158. Sahu, N., Viljoen, H. J., & Subramanian, A. (2019). Continuous low-intensity ultrasound attenuates IL-6 and TNFα-induced catabolic effects and repairs chondral fissures in bovine osteochondral explants. *BMC musculoskeletal disorders*, *20*(1), 1-13.

159. Sahu, N., Budhiraja, G., & Subramanian, A. (2020). Preconditioning of mesenchymal stromal cells with low-intensity ultrasound: influence on chondrogenesis and directed SOX9 signaling pathways. *Stem cell research & therapy*, *11*(1), 1-15.

160. Sams, A. E., & Nixon, A. J. (1995). Chondrocyte-laden collagen scaffolds for resurfacing extensive articular cartilage defects. *Osteoarthritis and Cartilage*, *3*(1), 47-59.

161. Schaefer, K. N., & Peifer, M. (2019). Wnt/Beta-catenin signaling regulation and a role for biomolecular condensates. Developmental cell, 48(4), 429-444.

162. Seo, H. H., Lee, S., Lee, C. Y., Lee, J., Shin, S., Song, B. W., ... & Hwang, K. C. (2019). Multipoint targeting of TGF-β/Wnt transactivation circuit with microRNA 384-5p for cardiac fibrosis. *Cell Death & Differentiation*, *26*(6), 1107-1123.

163. Setton, L. A., Elliott, D. M., & Mow, V. C. (1999). Altered mechanics of cartilage with osteoarthritis: human osteoarthritis and an experimental model of joint degeneration. *Osteoarthritis and cartilage*, *7*(1), 2-14.

164. Shchetinin, V. G. (1991). Calculation of the state parameters of condensed substances at high pressures and temperatures. *Combustion, Explosion and Shock Waves*, *27*(4), 426-432.

165. Sherrit, S., Leary, S. P., Dolgin, B. P., & Bar-Cohen, Y. (1999, October). Comparison of the Mason and KLM equivalent circuits for piezoelectric resonators in the thickness mode. In *1999 IEEE Ultrasonics Symposium. Proceedings. International Symposium (Cat. No. 99CH37027)* (Vol. 2, pp. 921-926). IEEE.

166. Sherrit, S., & Mukherjee, B. K. (2007). Characterization of piezoelectric materials for transducers. *arXiv preprint arXiv:0711.2657*.

167. Shukunami, C., Ishizeki, K., Atsumi, T., Ohta, Y., Suzuki, F., & Hiraki, Y. (1997). Cellular hypertrophy and calcification of embryonal carcinoma-derived chondrogenic cell line ATDC5 in vitro. *Journal of Bone and Mineral Research*, *12*(8), 1174-1188.

168. Singh, P., & Schwarzbauer, J. E. (2014). Fibronectin matrix assembly is essential for cell condensation during chondrogenesis. *Journal of cell science*, *127*(20), 4420-4428.

169. Smit, T. H., Huyghe, J. M., & Cowin, S. C. (2002). Estimation of the poroelastic parameters of cortical bone. *Journal of biomechanics*, *35*(6), 829-835.

170. Solheim, E., Hegna, J., & Inderhaug, E. (2020). Long-term survival after microfracture and mosaicplasty for knee articular cartilage repair: a comparative study between two treatments cohorts. *Cartilage*, *11*(1), 71-76.

171. Stachecka, J., Walczak, A., Kociucka, B., Ruszczycki, B., Wilczyński, G., & Szczerbal, I. (2018). Nuclear organization during in vitro differentiation of porcine mesenchymal stem cells (MSCs) into adipocytes. Histochemistry and cell biology, 149(2), 113-126.

172. Steinwachs, M. R., Guggi, T. H., & Kreuz, P. C. (2008). Marrow stimulation techniques. *Injury*, *39*(1), 26-31.

173. Stevens, A. L., Wishnok, J. S., White, F. M., Grodzinsky, A. J., & Tannenbaum, S. R. (2009). Mechanical injury and cytokines cause loss of cartilage integrity and upregulate proteins associated with catabolism, immunity, inflammation, and repair. *Molecular & Cellular Proteomics*, *8*(7), 1475-1489.

174. Suh, J. K., & DiSilvestro, M. R. (1999). Biphasic poroviscoelastic behavior of hydrated biological soft tissue. *Journal of Applied Mechanics*, *66*(2), 528-535.

175. Sun, C., Yuan, H., Wang, L., Wei, X., Williams, L., Krebsbach, P. H., ... & Liu, F. (2016). FAK promotes osteoblast progenitor cell proliferation and differentiation by enhancing Wnt signaling. *Journal of Bone and Mineral Research*, *31*(12), 2227-2238.

176. Szychlinska, M. A., Stoddart, M. J., D'Amora, U., Ambrosio, L., Alini, M., & Musumeci, G. (2017). Mesenchymal stem cell-based cartilage regeneration approach and cell senescence: can we manipulate cell aging and function?. *Tissue Engineering Part B: Reviews*, *23*(6), 529-539.

177. Takeuchi, R., Ryo, A., Komitsu, N., Mikuni-Takagaki, Y., Fukui, A., Takagi, Y., ... & Saito, T. (2008). Low-intensity pulsed ultrasound activates the phosphatidylinositol

3 kinase/Akt pathway and stimulates the growth of chondrocytes in three-dimensional cultures: a basic science study. *Arthritis research & therapy*, *10*(4), 1-11.

178. ter Haar, G., Sinnett, D., & Rivens, I. (1989). High intensity focused ultrasound-a surgical technique for the treatment of discrete liver tumours. *Physics in Medicine & Biology*, *34*(11), 1743.

179. Töyräs, J., Laasanen, M. S., Saarakkala, S., Lammi, M. J., Rieppo, J., Kurkijärvi, J., ... & Jurvelin, J. S. (2003). Speed of sound in normal and degenerated bovine articular cartilage. *Ultrasound in medicine & biology*, *29*(3), 447-454.

180. Truong, M. D., Chung, J. Y., Kim, Y. J., Jin, L. H., Kim, B. J., Choi, B. H., & Min, B. H. (2014). Histomorphochemical comparison of microfracture as a first-line and a salvage procedure: Is microfracture still a viable option for knee cartilage repair in a salvage situation?. *Journal of Orthopaedic Research*, *32*(6), 802-810.

181. Uenaka, K., Imai, S., Shioji, S., Kumagai, K., Okumura, N., & Matsusue, Y. (2009). 174 THE EFFECT OF LOW-INTENSITY PULSED ULTRASOUND FOR SACFFOLD-FREE CHONDROCYTE PLATE IN VITRO AND IN VIVO. *Osteoarthritis and Cartilage*, *17*, S102-S103.

182. Vahedi, P., Hosainzadegan, H., Brazvan, B., Roshangar, L., Shafaei, H., & Salimnejad, R. (2021). Treatment of cartilage defects by Low-intensity pulsed ultrasound in a sheep model. *Cell and Tissue Banking*, *22*(3), 369-378.

183. Van den Berg, W. B. (2011). Osteoarthritis year 2010 in review: pathomechanisms. *Osteoarthritis and Cartilage*, *19*(4), 338-341.

184. Vincent, H. K., Heywood, K., Connelly, J., & Hurley, R. W. (2012). Obesity and weight loss in the treatment and prevention of osteoarthritis. *PM&R*, *4*(5), S59-S67.

185. Waldrop, K., & Serfass, A. (2008). Clinical effectiveness of noncontact, low-frequency, nonthermal ultrasound in burn care. *Ostomy Wound Manage*, *54*(6), 66-69.

186. Wang, S. H., Lee, L. P., & Lee, J. S. (2001). A linear relation between the compressibility and density of blood. *The Journal of the Acoustical Society of America*, *109*(1), 390-396.

187. Weiss, M., Ben-Shlomo, A. B., Hagag, P., & Rapoport, M. (2000). Reference database for bone speed of sound measurement by a novel quantitative multi-site ultrasound device. *Osteoporosis International*, *11*(8), 688-696.

188. Whitney, N. P., Lamb, A. C., Louw, T. M., & Subramanian, A. (2012). Integrin-mediated mechanotransduction pathway of low-intensity continuous ultrasound in human chondrocytes. *Ultrasound in medicine & biology*, *38*(10), 1734-1743.

189. Wilusz, R. E., Sanchez-Adams, J., & Guilak, F. (2014). The structure and function of the pericellular matrix of articular cartilage. *Matrix biology*, *39*, 25-32.

190. Wu, M., Chen, G., & Li, Y. P. (2016). TGF-β and BMP signaling in osteoblast, skeletal development, and bone formation, homeostasis and disease. *Bone research*, *4*(1), 1-21.

191. Xu, Y., Wang, Y. Q., Wang, A. T., Yu, C. Y., Luo, Y., Liu, R. M., ... & Xiao, J. H. (2020). Effect of CD44 on differentiation of human amniotic mesenchymal stem cells

into chondrocytes via Smad and ERK signaling pathways. *Molecular medicine reports*, *21*(6), 2357-2366.

192. Yang, S. W., Kuo, C. L., Chang, S. J., Chen, P. C., Lin, Y. T., Manousakas, I., & Kuo, S. M. (2014). Does low-intensity pulsed ultrasound treatment repair articular cartilage injury? A rabbit model study. *BMC musculoskeletal disorders*, *15*(1), 1-7.

193. Zelenski, N. A., Leddy, H. A., Sanchez-Adams, J., Zhang, J., Bonaldo, P., Liedtke, W., & Guilak, F. (2015). Type VI collagen regulates pericellular matrix properties, chondrocyte swelling, and mechanotransduction in mouse articular cartilage. *Arthritis & Rheumatology*, *67*(5), 1286-1294.

194. Zhang, Z. (2014). Chondrons and the pericellular matrix of chondrocytes. *Tissue Engineering Part B: Reviews*, *21*(3), 267-277.

195. Zhang, N., Chow, S. K. H., Leung, K. S., & Cheung, W. H. (2017). Ultrasound as a stimulus for musculoskeletal disorders. *Journal of orthopaedic translation*, *9*, 52-59.

196. Zhang, T., Wen, F., Wu, Y., Goh, G. S. H., Ge, Z., Tan, L. P., ... & Yang, Z. (2015). Cross-talk between TGF-beta/SMAD and integrin signaling pathways in regulating hypertrophy of mesenchymal stem cell chondrogenesis under deferral dynamic compression. *Biomaterials*, *38*, 72-85.

197. Zhang, Z. (2015). Chondrons and the pericellular matrix of chondrocytes. *Tissue Engineering Part B: Reviews*, *21*(3), 267-277.

198. Zhao, Z., Li, Y., Wang, M., Zhao, S., Zhao, Z., & Fang, J. (2020). Mechanotransduction pathways in the regulation of cartilage chondrocyte homoeostasis. *Journal of cellular and molecular medicine*, *24*(10), 5408-5419.

199. Zhou, S., Eid, K., & Glowacki, J. (2004). Cooperation between TGF-β and Wnt pathways during chondrocyte and adipocyte differentiation of human marrow stromal cells. *Journal of Bone and Mineral Research*, *19*(3), 463-470.

200. Zhou, S., Schmelz, A., Seufferlein, T., Li, Y., Zhao, J., & Bachem, M. G. (2004). Molecular mechanisms of low intensity pulsed ultrasound in human skin fibroblasts. *Journal of Biological Chemistry*, *279*(52), 54463-54469.

201. Zhou, J., Aponte-Santamaría, C., Sturm, S., Bullerjahn, J. T., Bronowska, A., & Gräter, F. (2015). Mechanism of focal adhesion kinase mechanosensing. PLoS Comput Biol, 11(11), e1004593.

202. Zwikker, C., & Kosten, C. W. (1949). *Sound absorbing materials*. Elsevier publishing company.

APPENDIX A: NOMENCLATURE AND ABBREVIATIONS

a	Pore Size
ACI	Autologous Chondrocyte Implantation
ACL	Anterior Cruciate Ligament
ALK1	Activin Receptor-Like Kinase 1
APC	Adenomatous Polyposis Coli
c	Speed of Sound
c_c	Complex Speed of Sound
cLIUS	Continuous Low-Intensity Ultrasound
COL2A1	Type II Collagen
C_P	Heat Capacity
d	Diameter
DICOM	Digital Imaging and Communications in Medicine
DZ	Deep Zone
DZP	Different Zonal Properties
ECM	Extracellular Matrix
E_d	Young’s Modulus
ERK	Extracellular Signal-Related Kinase
F	Viscous Drag
$\boldsymbol{F}$	Body Load Source Term
f	Frequency
FAK	Focal Adhesion Kinase
FE	Finite Element
f_r	Reference Frequency
GSK3B	Glycogen Synthase Kinase 3 Beta
$\boldsymbol{I}$	Identity Tensor
IFNγ	Type II Interferon
IL-1	Interleukin-1
IL-1β	Interleukin-1 Beta
IL-6	Interleukin-6
k	Wave Number
$\mathbf{k}$	Wave Vector
K_d	Drained Bulk Modulus
K	Diffusive Drag Coefficient
KLM	Krimholtz Leedom Matthaei
kPa	Kilopascal
M	Biot Module
MHz	Megahertz

mm	Millimeter
MMP13	Matrix Metallopeptidase 13
MRI	Magnetic Resonance Image
MSC	Mesenchymal Stem Cell
MZ	Middle Zone
N	Number of Elements
$\mathbf{n_k}$	Normal Unit Vector
OA	Osteoarthritis
P	Period
P	Pressure
PCM	Pericellular Matrix
p_f	Pore Pressure
pLIUS	Pulsed Low-Intensity Ultrasound
p_0	Pressure Amplitude
p_t	Total Pressure
r	Radius
R_C	Chondrocyte Radius
R_p	Pericellular Matrix Radius
SOX9	SRY-Box Transcription Factor 9
SZ	Superficial Zone
SZP	Same Zonal Properties
TGF-β	Transforming Growth Factor Beta
TNFα	Tumor Necrosis Factor Alpha
$\boldsymbol{u}$	Porous Material Displacement
$\boldsymbol{q}_d$	Source Vector
Q_m	Monopole Source Term
US	Ultrasound
Vpp	Peak to Peak Voltage
$\boldsymbol{w}$	Fluid Displacement
Wnt	Wingless Type Protein
α_B	Biot-Willis Coefficient
κ	Permeability
$\widetilde{\mu_f}$	Frequency-Dependent Viscosity
μ_f	Dynamic Fluid Viscosity
µm	Micrometer
µs	Microsecond
ν_d	Poisson's Ratio

ρ	Density
ρ_{av}	Average Density
ρ_c	Complex Density
ρ_d	Porous Matrix Density
ρ_f	Fluid Density
ρ_s	Solid Density
τ	Dimensionless Time
$\tau_{¥}$	Tortuosity
u	Material Sound Velocity
ϕ	Solid Volume Fraction
ω	Angular Frequency
$\boldsymbol{\sigma}$	Cauchy Stress Tensor
$\boldsymbol{\epsilon}$	Strain Tensor
ϵ_p	Porosity

APPENDIX B: KLM EQUIVALENT MATHEMATICS

The basic structure of the KLM model derived by Krimholtz-Leedoem-Matthaei can be seen by Figure 1 in the main text. Equivalent circuit parameters are described by equations B1.2 through B1.4. The components in the model utilize the

$$Z_0 = \rho_{PZT} c_{PZT} A \tag{B1.1}$$

where ρ_{PZT}, c_{PZT}, and A are density, speed of sound, and area of the piezoelectric element,

$$C_0 = \varepsilon A/d \tag{B1.2}$$

where ε is the permittivity of the piezoelectric element, and d is its thickness,

$$X1 = \frac{h_{33}^2}{\omega^2 Z_0} sin(\omega d/c_{PZT}) \tag{B1.3}$$

where h_{33} is the electromechanical constant and ω is the angular frequency, and finally:

$$\phi = \frac{\omega Z_0}{2h_{33}\sin(\omega d/2c_{PZT})} \tag{B1.4}$$

These equations are used to determine the impedance values at the front and back of the transducer, detailed in Figure 1.

APPENDIX C: COMSOL PARAMETERS

For the Suspended Cell Model

Variable	Symbol	MSC		Blood Clot	Chondrocyte		PCM	ECM
		Nucleus	Cytoplasm		Nucleus	Cytoplasm		
Radius (µm)	r	7.1 (Stachecka *et al.*, 2018)	11.25 (Kreuger *et al.*, 2018)	32.5	3.5 (Miller *et al.*, 2017)	6.5 (Miller *et al.*, 2017)	9 (Miller *et al.*, 2017)	32.5 (Miller *et al.*, 2017)
Young's Modulus (kPa)	E	4.7 (Ruiz *et al.*, 2012)	9.07 (Ruiz *et al.*, 2012)	5.3 (Mfoumou *et al.*, 2014)		1 (Haider, 2004)	34.7 (Alexopoulos *et al.*, 2003)	1.3[MPa] (Alexopoulos *et al.*, 2003)
Porosity	ε			0.19 (Wufsus *et al.*, 2013)	0.65 (Miller *et al.*, 2017)	0.75 (Miller *et al.*, 2017)	0.83 (Haider, 2004)	0.83
Poisson's Ratio	σ		0.5 (Ruiz *et al.*, 2012)	0.49 (Mfoumou *et al.*, 2014)	0.38 (Miller *et al.*, 2017)	0.43 (Haider, 2004)	0.04 (Haider, 2004)	0.04
Permeability (m^2)	κ			6.7E-15 (Wufsus *et al.*, 2013)	7e-19 (Miller *et al.*, 2017)	7e-19 (Miller *et al.*, 2017)	0.76e-16 (Alexopoulos *et al.*, 2003)	9e-16 (Alexopoulos *et al.*, 2003)

Density (kg/m^3)	ρ			1.08E3 (5)	400 (Miller *et al*., 2017)	300 (Miller *et al*., 2017)		
Bulk Modulus (Pa)	K			E/3(1-2σ)	2e3 (Miller *et al*., 2017)	500 (Miller *et al*., 2017)	E/3(1-2σ)	E/3(1-2σ)
Shear Modulus (Pa)	G			E/2(1+σ)			E/2(1+σ)	E/2(1+σ)
Biot-Willis Coefficient	α_B				0.9996 (Miller *et al*., 2017)	0.9999 (Miller *et al*., 2017)	0.99749	0.9058
Tortuosity	τ				2	1.2 (Miller *et al*., 2017)		
Dynamic Viscosity (Pa*s)	μ			0.003	0.7e-3 (Miller *et al*., 2017)	0.7e-3 (Miller *et al*., 2017)	3.4e3 (Nguyen *et al*., 2010)	3.4e3
Compressibility of Fluid (1/Pa)	χ_f			4.32E-10 (Wang *et al*., 2001)	4.35e-10 (Miller *et al*., 2017)	4.35e-10 (Miller *et al*., 2017)		

Any values not input for the MSC are made the same as the values for the chondrocyte.

For the 3D Model

Variable	Symbol	Skin	Muscle	Cartilage	Bone
Density (kg/m^3)	ρ	1020 (Liang *et al*., 2009)	1073 (Kuthe, Uddanwadiker, 2016)	1470 (Basser *et al*., 1998)	1900 (Cameron *et al*., 1999)
Speed of Sound (m/s)	c	1645 (Moran *et al*., 1995)	1550 (Feigin *et al*., 2020)	1640 (Toyras *et al*., 2003)	3700 (Cameron *et al*., 1999)
Young's Modulus (Pa)	E			1e6 (Guo *et al*., 2013)	7.3e9 (Franciosa, Gerbino, 2010)
Poisson's Ratio	σ			0.125 (Korhonen *et al*., 2003)	0.3 (Franciosa, Gerbino, 2010)
Biot-Willis Coefficient	α_B			0.875 (COMSOL, 2018)	0.15 (Smit *et al*., 2002)
Porosity	ε			0.75 (Hosoda *et al*., 2009)	0.05 (Cardoso *et al*., 2013)
Permeability (m^2)	κ			2.6e-14 (Hosoda *et al*., 2009)	2.2e-7 (Smit *et al*., 2002)
Tortuosity	τ			1	1.05 (Fellah *et al*., 2004)

Using the Pressure acoustics physics on the skin and muscle only requires density and speed of sound to be specified for the materials it is applied to.

APPENDIX D: KINETIC EQUATIONS IN PATHWAYS

Rate constant values used in pathway model.

	Units	Value		Units	Value
k_1					
k_{2cat}	s^{-1}	9.33	k_{2m}	nM	0.132
k_{3cat}	s^{-1}	9.33	k_{3m}	nM	0.132
k_4	(nMs)$^{-1}$	0.09	k_{4b}	s^{-1}	0.6
k_{5cat}	s^{-1}	9.33			
k_{6cat}	s^{-1}	9.33			
k_7	(nMs)$^{-1}$	0.09	k_{7b}	s^{-1}	0.09
k_8	(nMs)$^{-1}$	6	k_{8b}	s^{-1}	0.06
k_9	s^{-1}	0.3	k_{9b}	(nMs)$^{-1}$	0.0009
k_{10}	(nMs)$^{-1}$	0.003	k_{10b}	s^{-1}	0.05
k_{11}	(nMs)$^{-1}$	0.003	k_{11b}	s^{-1}	0.1
k_{12m}	nM	340	V_{12max}	nM s^{-1}	1.7
k_{13}	(nMs)$^{-1}$	0.003	k_{13b}	s^{-1}	0.1
k_{14}	(nMs)$^{-1}$	0.0015	k_{14b}	s^{-1}	0.0001
k_{15}	(nMs)$^{-1}$	0.03	k_{15b}	s^{-1}	0.064
k_{16}	(nMs)$^{-1}$	0.01	k_{16b}	s^{-1}	0.06
k_{17}	(nMs)$^{-1}$	0.021	k_{17b}	s^{-1}	0.1
k_{18}	(nMs)$^{-1}$	0.0045	k_{18b}	s^{-1}	0.03
k_{19}	(nMs)$^{-1}$	0.01	k_{19b}	s^{-1}	0.0214
k_{20}	(nMs)$^{-1}$	0.009	k_{20b}	s^{-1}	0.0429
k_{21}	(nMs)$^{-1}$	0.12	k_{21b}	s^{-1}	0.000214

k_{22}	s^{-1}	0.222	k_{22m}	nM	0.181
k_{23m}	nM	0.0571	V_{23max}	nM s^{-1}	0.289
k_{24}	μM s^{-1}	0.49	k_{24b}	s^{-1}	0.049
k_{25}	μM s^{-1}	0.65	k_{25b}	s^{-1}	0.065
k_{26}	μM s^{-1}	0.88	k_{26b}	s^{-1}	0.088
k_{27}	μM s^{-1}	0.88	k_{27b}	s^{-1}	0.088
k_{28}	μM s^{-1}	0.88	k_{28b}	s^{-1}	0.088
k_{29}	μM s^{-1}	0.88	k_{29b}	s^{-1}	0.088
k_{30}	μM s^{-1}	0.18			
k_{31}	μM s^{-1}	0.22			
k_{32}	μM s^{-1}	0.22			
k_{33}	μM s^{-1}	0.01			
k_{34}	μM s^{-1}	0.01			
k_{35}	μM s^{-1}	0.014			
k_{36}	μM s^{-1}	0.014			
k_{37}	μM s^{-1}	0.61	k_{37b}	s^{-1}	0.046
k_{38}	μM s^{-1}	0.54	k_{38b}	s^{-1}	0.04
k_{39}	μM s^{-1}	0.018	k_{39b}	s^{-1}	0.012
k_{40}	μM s^{-1}	0.013	k_{40b}	s^{-1}	0.012
k_{41}	μM s^{-1}	0.26	k_{41b}	s^{-1}	0.035
k_{42}	μM s^{-1}	0.26	k_{42b}	s^{-1}	0.035
k_{degT1R}	min^{-1}	0.00256	k_{degT2R}	min^{-1}	0.0132
k_{degLRC}	min^{-1}	0.00256	$k_{degTGFB}$	min^{-1}	0.347
$k_{prodT1R}$	(nMmin)$^{-1}$	0.0137	$k_{prodT2R}$	nM min^{-1}	0.0190076
k_i	min^{-1}	0.333	k_r	min^{-1}	0.0333

$k_{impSmad23}$	min^{-1}	0.156	$k_{expSmad23}$	min^{-1}	0.739
$k_{impSmad4}$	min^{-1}	0.156	$k_{expSmad4}$	min^{-1}	0.355
$k_{impComplex}$	min^{-1}	0.889			
$k_{offSmads}$	min^{-1}	1	$k_{dephoSmads}$	min^{-1}	0.394
k_{aLRC}	nM^{-2} min^{-1}	117.897			
$k_{dissLRC}$	min^{-1}	0.0438111			
k_{lid}	(nMmin)$^{-1}$	0.0233678			
$k_{phoSmad23}$	(nMmin)$^{-1}$	0.0488268			
$k_{onSmads}$	(nMmin)$^{-1}$	0.198472			
k_{onns}	min^{-1}	0.0505413	k_{offns}	min^{-1}	2.073285
k_{43}	min^{-1}	0.182	k_{44}	min^{-1}	0.0182
k_{45}	(nMmin)$^{-1}$	0.05	k_{46}	min^{-1}	0.267
k_{47}	min^{-1}	0.133			
k_{48}	(nMmin)$^{-1}$	0.0909	k_{48b}	min^{-1}	0.909
k_{49}	(nMmin)$^{-1}$	1	k_{49b}	min^{-1}	50
k_{50}	(nMmin)$^{-1}$	1	k_{50b}	min^{-1}	120
k_{51}	min^{-1}	206	k_{52}	min^{-1}	206
k_{53}	min^{-1}	0.417			
v_{12}	(nMmin)$^{-1}$	0.423	k_{54}	min^{-1}	0.000257
k_{55}	(nMmin)$^{-1}$	0.0000822	k_{56}	min^{-1}	0.167
k_{57}	(nMmin)$^{-1}$	1	k_{57b}	min^{-1}	30
k_{58}	(nMmin)$^{-1}$	1	k_{58b}	min^{-1}	1200
V_{max1}	nM min^{-1}	150	K_{m1}	nM	10
K_i	nM	9	V_{max2}	nM min^{-1}	15
K_{m2}	nM	8	k_{cat1}	min^{-1}	1.5

K_{m3}	nM	15	V_{max3}	nM min^{-1}	45
K_{m4}	nM	15	k_{cat2}	min^{-1}	1.5
K_{m5}	nM	15	V_{max4}	nM min^{-1}	45
K_{m6}	nM	15	k_{cat3}	min^{-1}	1.5
K_{m7}	nM	15	V_{max5}	nM min^{-1}	45
K_{m8}	nM	15	k_{cat4}	min^{-1}	1.5
K_{m9}	nM	9	k_{59}	(nMmin)$^{-1}$	0.15
k_{60}	min^{-1}	39	V_{max6}	nM min^{-1}	45
K_{m10}	nM	12	k_{cat5}	min^{-1}	0.6
K_{m11}	nM	15	n		2
k_{61}	min^{-1}	0.015	k_{cat6}	min^{-1}	1.5
K_{m12}	nM	15	k_{cat7}	min^{-1}	1.5
K_{m13}	nM	15	V_{max7}	nM min^{-1}	45
K_{m14}	nM	15	k_{62}	min^{-1}	0.000001

APPENDIX E: RATE EQUATIONS

Species	Initial Conc.	Rate Equation
FAKo	0	k1*(1-v*w/dG)^(1/v-1)*exp(dG*(1-v*w/dG)^(1/v))
FAKop	0	(k2cat*FAKop^2)/(k2m+FAKop)-(k4*FAKop*Srcp-k4b*SrcpFAKop)-(k7*FAKop*Shc-k7b*FAKopSh)+(k9*FAKopShP-k9b*FAKop*ShP)+(k21*FAKopShPGS-k21b*ShPGS*FAKop)
Src	90nM	-((k3cat*Src^2)/(k3m+Src))
Srcp	0	((k3cat*Src^2)/(k3m+Src))
SrcpFAKop	0	k4*FAKop*Srcp-k4b*SrcpFAKop-k5cat*SrcpFAKop
SrcpFAKopp	0	k5cat*SrcpFAKop- k6cat*SrcpFAKopp
SrcpFAKoppp	0	k6cat*SrcpFAKopp-(k10*SrcpFAKop*Grb2-k10b*SrcpFAKopppG)-(k18*SrcpFAKoppp*GS-k18b*SrcpFAKopppGS)
Shc	1000nM	-(k7*FAKop*Shc-k7b*FAKopSh)+V12max*ShP/(k12m+ShP)
FAKopSh	0	k7*FAKop*Shc-k7b*FAKopSh-(k8*FAKopSh-k8b*FAKopShP)
FAKopShP	0	k8* FAKopSh-k8b*FAKopShP-(k9*FAKopShP-k9b*FAKop*ShP)-(k13*FAKopShP*Grb2-k13b*FAKopShPG)-(k20*FAKopShP*GS-k20b*FAKopShPGS)
ShP	0	k9*FAKopShP-k9b*FAKop*ShP-(k11*ShP*Grb2-k11b*ShPG)-(V12max*ShP/(k12m+ShP))-(k17*ShP*GS-k17b*ShPGS)

Grb2	48nM	-(k10*SrcpFAKop*Grb2-k10b*SrcpFAKopppG)-(k11*ShP*Grb2-k11b*ShPG)-(k13*FAKopShP*Grb2-k13b*FAKopShPG)-(k14*Grb2*SOS-k14b*GS)
SrcpFAKopppG	0	k10*SrcpFAKop*Grb2-k10b*SrcpFAKopppG-(k16*SrcpFAKopppG*SOS-k16b*SrcpFAKopppGS)
ShPG	0	k11*ShP*Grb2-k11b*ShPG-(k15*ShPG*SOS-k15b*ShPGS)
FAKopShPG	0	k13*FAKopShP*Grb2-k13b*FAKopShPG-(k19*FAKopShPG*SOS-k19b*FAKopShPGS)
SOS	62nM	-(k14*Grb2*SOS-k14b*GS)-(k15*ShPG*SOS-k15b*ShPGS)-(k16*SrcpFAKopppG*SOS-k16b*SrcpFAKopppGS) -(k19*FAKopShPG*SOS-k19b*FAKopShPGS)
GS	0	k14*Grb2*SOS-k14b*GS-(k17*ShP*GS-k17b*ShPGS)-(k18*SrcpFAKoppp*GS-k18b*SrcpFAKopppGS)-(k20*FAKopShP*GS-k20b*FAKopShPGS)
ShPGS	0	k15*ShPG*SOS-k15b*ShPGS+ k17*ShP*GS-k17b*ShPGS+k21*FAKopShPGS-k21b*ShPGS*FAKop
SrcpFAKopppGS	0	k16*SrcpFAKopppG*SOS-k16b*SrcpFAKopppGS-(k18*SrcpFAKoppp*GS-k18b*SrcpFAKopppGS)
FAKopShPGS	0	k19*FAKopShPG*SOS-k19b*FAKopShPGS+k20*FAKopShP*GS-k20b*FAKopShPGS-(k21*FAKopShPGS-k21b*ShPGS*FAKop)
RasGTP	0	k22*RasGDP*RGS/(k22m+RasGDP)-(V23max*RasGTP/(k23m+RasGTP))-(k24*Raf*RasGTP-k24b*RasRaf)
RasGDP	120nM	V23max*RasGTP/(k23m+RasGTP)-(k22*RasGDP*RGS/(k22m+RasGDP))

Raf	0.013uM	-(k24*RasRaf-k24b*RasGTP*Raf)
RasRaf	0	k24*Raf*RasGTP-k24b*RasRaf-(k25*RasRaf*MEK-k25b*RasRafMEK)+k30*RasRafMEK
RasRafMEK	0	k25*RasRaf*MEK-k25b*RasRafMEK-k30*RasRafMEK
MEKERK	0	k26*MEK*ERK-k26b*MEKERK
pMEKERK	0	k27*pMEK*ERK-k27b*pMEKERK-k31*pMEKERK-(k42*pMEKERKn-42b*pMEKERK)
MEKERKn	0	k28*MEKn*ERKn-k28b*MEKERKn-(k41*MEKERKn-k41b*MEKERK)
pMEKERKn	0	k29*pMEKn*ERKn-k29b*pMEKERKn-32*pMEKn*ERKn-(k42*pMEKERKn-k42b*pMEKERK)
pMEK	0	k30*RasRafMEK+k31*pMEKERK+k38*pMEKn-k38b*pMEK
pERK	0	k31*pMEKERK+k40*pERKn-40b*pERK
pMEKn	0	k32*pMEKERKn-(k38*pMEKn-k38bpMEK)
ERKn	0	k32*pMEKERKn+k36*pERKn-(k39*ERKn-k39b*ERK)-(k28*MEKn*ERKn-k28b*MEKERKn)-(k29*pMEKn*ERKn-k29b*pMEKERKn)
pERKn	0	-(k40*pERK-k40b*pERKn)
MEK	1.39uM	k33*pMEK+k37*MEKn-k37b*MEK-(k25*RasRaf*MEK-k25b*RasRafMEK)
MEKn	0	k34*pMEKn-k28*MEKn*ERKn-k28b*MEKERKn-(k37*MEKn-k37b*MEK)
ERK	0.96uM	k35*pERK-(k26*MEK*ERK-k26b*MEKERK)-(k27*pMEK*ERK-k27b*pMEKERK)+(k39*ERKn-k39b*ERK)
exTGFB	0	-(Vc/Vmed)*kaLRC*exTGFB*T2Rsurf*T1Rsurf-konns*exTGFB+koffns*TGFBns

T1Rsurf	0.702494nM	kprodT1R-ki*T1Rsurf+kr*T1Rendo-kaLRC*exTGFB*T2Rsurf*T1Rsurf
T1Rendo	6.52344nM	ki*T1Rsurf-kr*T1Rendo-kdegT1R*T1Rendo+kdissLRC*LRCendo
T2Rsurf	0.201077nM	kprodT2R-ki*T2Rsurf+kr*T2Rendo-kaLRC*exTGFB*T2Rsurf*T1Rsurf
T2Rendo	1.43997nM	ki*T2Rsurf-kr*T2Rendo-kdegT2R*T2Rendo+kdissLRC*LRCendo
LRCsurf	0	kaLRC*exTGFB*T2Rsurf*T1Rsurf-ki*LRCsurf-klid*LRCsurf*TSmad23pn
LRCendo	0	ki*LRCsurf-kdissLRC*LRCendo-kdegLRC*LRCendo
Smad23c	60.6nM	(Vn/Vc)*kexpSmad23*Smad23n-kphoSmad23*Smad23c*LRCendo-kimpSmad23*Smad23c
Smad23n	28.5nM	(Vc/Vn)*kimpSmad23*Smad23c-kexpSmad23*Smad23n+kdephoSmad23*PSmad23n
Smad4c	50.8nM	(Vn/Vc)*kexpSmad4*Smad4n-konSmads*PSmad23c*Smad4c+koffSmads*PSmad23Smad4c-kimpSmad4*Smad4c
Smad4n	50.8nM	(Vc/Vn)*kimpSmad4*Smad4c-kexpSmad4*Smad4n+koffSmads*PSmad23Smad4c-konSmads*PSmad23c*Smad4n
PSmad23c	0	kphoSmad23*Smad23c*LRCendo-kimpSmad23*PSmad23c+(Vn/Vc)*kexpSmad23*PSmad23n-konSmads*PSmad23c*Smad4c+koffSmads*PSmad23Smad4c-2*konSmads*PSmad23c*PSmad23c+2*koffSmads*PSmad23c*PSmad23c

PSmad23PSmad23c	0	konSmads*PSmad23c*PSmad23c-koffSmads*PSmad23PSmad23c-kimpSmads*PSmad23PSmad23c
PSmad23Smad4c	0	konSmads*PSmad23c*Smad4c-koffSmads*PSmad23PSmad4c-kimpSmads*PSmad23PSmad4c
PSmad23n	0	(Vc/Vn)*kimpSmad23*PSmad23c-kexpSmad23*PSmad23n+koffSmads*PSmad23Smad4n-konSmads*PSmad23n*Smad4n-kdephoSmad23*PSmad23n+2*(koffSmads*PSmad23PSmad23n-konSmads*PSmad23PSmad23n)^2
PSmad23PSmad23n	0	(Vc/Vn)*kimpSmads*PSmad23PSmad23c-koffSmads*PSmad23PSmad23n+konSmads*PSmad23n^2
PSmad23Smad4n	0	(Vc/Vn)*kimpSmads*PSmad23PSmad4c-koffSmads*PSmad23PSmad4n+konSmads*PSmad23n*Smad4n
TGFBendo	0	kdissLRC*LRCendo-kdegTGFB*TGFBendo
TGFBns	0	konns*exTGFB-koffns*TGFBns
Dshi	100nM	-k43*Dshi+ k44*Dsha
Dsha	0	k43*Dshi+-k44*Dsha
APCpAxinpGSK3B	0.0153nM	k46*APCAxinGSK3B- k47*APCpAxinpGSK3B-(k50*APCpAxinpGSK3B*Bcatenin-k50b*BcateninAPCpAxinpGSK3B)+k52*BcateninpAPCpAxinpGSK3B
APCAxinGSK3B	0.0076 nM	-k45*Dsha*APCAxinGSK3B- k46*APCAxinGSK3B+k47*APCpAxinpGSK3B+ k48*GSK3B*APCAxin-k48b*APCAxinGSK3B

GSK3B	49.1372 nM	k45*Dsha*APCAxinGSK3B-(k48*GSK3B*APCAxin-k48b*APCAxinGSK3B)-(kcat7*pERK*GSK3B/(Km13+GSK3B))+Vmax7*GSK3Bp/(Km14+GSK3Bp)
APCAxin	0.0015 nM	k45*Dsha*APCAxinGSK3B-(k48*GSK3B*APCAxin-k48b*APCAxinGSK3B)+k49*APC*Axin-k49b*APCAxin
APC	96.6019 nM	-(k49*APC*Axin-k49b*APCAxin)-(k58*APC*Bcatenin-k58b*BcateninAPC)
BcateninAPCpAxinpGSK3B	0.002 nM	k50*APCpAxinpGSK3B*Bcatenin-k50b*BcateninAPCpAxinpGSK3B-k51*BcateninAPCpAxinpGSK3B
BcateninpAPCpAxinpGSK3B	0.002 nM	k51*BcateninAPCpAxinpGSK3B-k52*BcateninpAPCpAxinpGSK3B
pBcatenin	0.9881 nM	k52*BcateninpAPCpAxinpGSK3B-k53*pBcatenin
Bcatenin	42.7224 nM	-(k50*APCpAxinpGSK3B*Bcatenin-k50b*BcateninAPCpAxinpGSK3B)+v12-k54*Bcatenin-(k57*Bcatenin*TCF-k57b*BcateninTCF)-(k58*APC*Bcatenin-k58b*BcateninAPC)
Axin	0.0008 nM	-(k49*APC*Axin-k49b*APCAxin)+k55+k62*(Bcatenin+BcateninTCF)-k56*Axin
TCF	6.1879 nM	-(k57*Bcatenin*TCF-k57b*BcateninTCF)
BcateninTCF	8.8121 nM	k57*Bcatenin*TCF-k57b*BcateninTCF
BcateninAPC	3.4392 nM	k58*APC*Bcatenin-k58b*BcateninAPC
Raf1	112.5585 nM	-kcat1*RasGTP*Raf1/(Km3+Raf1)+Vmax3*Raf/(Km4+Raf)+kcat4*pERK*Raf1RKIP/(Km9+Raf1RKIP)-(k59*Raf1*RKIP-k60*Raf1RKIP)-kcat6*XX*Raf1/(Km12+Raf1)

Raf1RKIP	180.9595 nM	-kcat4*pERK*Raf1RKIP/(Km9+Raf1RKIP) +k59*Raf1*RKIP-k60*Raf1RKIP
RKIP	418.1788 nM	-(k59*Raf1*RKIP-k60*Raf1RKIP)+Vmax6*RKIPp/(Km10+RKIPp)
RKIPp	0.8619 nM	-Vmax6*RKIPp/(Km10+RKIPp) +kcat4*pERK*Raf1RKIP/(Km9+Raf1RKIP)
XX	10.263 nM	kcat5*BcateninTCF^n/(Km11^n+BcateninTCF^n)-k61*XX-kcat6*XX*RasRaf/(Km12+RasRaf)
GSK3Bp	0.85544 nM	kcat7*pERK*GSK3B/(Km13+GSK3B)-Vmax7*GSK3Bp/(Km14+GSK3Bp)